TERAHERTZ OPTICAL PROPERTIES OF METAMATERIALS AND OPTICAL COMPONENTS FABRICATED USING POLYMER-BASED ADDITIVE MANUFACTURING

by

Serang Park

A dissertation submitted to the faculty of
The University of North Carolina at Charlotte
in partial fulfillment of the requirements
for the degree of Doctor of Philosophy in
Optical Science and Engineering

Charlotte

2021

Approved by:

Dr. Tino Hofmann

Dr. Glenn Boreman

Dr. Thomas Suleski

Dr. Thomas Schmedake

ABSTRACT

SERANG PARK. Terahertz optical properties of metamaterials and optical components fabricated using polymer-based additive manufacturing. (Under the direction of DR. TINO HOFMANN)

Continuous advancement in terahertz technologies have drawn interest in manufacturing and rapid prototyping of optical components suitable for the terahertz spectral range. One of the approaches of realizing such optical components is additive manufacturing, which has been studied in recent years for fabricating terahertz optical elements including lenses, filters, and waveguides. Stereolithography, with its superior resolution compared to other prevalent additive manufacturing techniques, could be an efficient way of fabricating terahertz elements with sub-wavelength scale architectures. However stereolithographically fabricated terahertz optical elements or metamaterials have not been studied extensively. In fact there is lack of information on the terahertz optical properties of materials available for stereolithography, which impedes first-principle calculations and further development of terahertz structures using stereolithography. In this thesis, we sought to fill this knowledge gap by determining the terahertz optical properties of materials commonly available for stereolithography. Utilizing the determined material properties, terahertz optical elements and metamaterials have been designed and experimentally realized. One-dimensional terahertz photonic crystals and defect modes within such crystals have been demonstrated for the first time through a single-step stereolithography from a single dielectric material. Mechanical tunability of the photonic bandgap and defect modes of the one-dimensional photonic crystals was realized experimentally. In addition, stereolithographically fabricated anisotropic metamaterial composed of slanted columnar structures have been explored for the first time. This metamaterial design was successfully demonstrated as a single layer, as well as constituent layers of one-dimensional photonic crystal structures. Fabrication of terahertz optics with desired curvature have also been investigated using two different approaches. Off-axis parabolic reflectors have been demonstrated first by metalizing stereolithographically fabricated polymer base, then by employing one-dimensional photonic crystal structure into design. In conclusion, stereolithography has been introduced as a new paradigm for fabrication of custom terahertz elements and novel metamaterials with tailored optical properties.

ACKNOWLEDGEMENTS

I would like to express my sincerest gratitude to my advisor, Dr. Tino Hofmann for the immeasurable support he has provided over the years. His earnest attitude towards his research, work, and life has inspired me greatly. I would like to thank Dr. Glenn Boreman for his valuable insight and advice on our collaborative work and my future career. I would like to thank Dr. Thomas Suleski and Dr. Thomas Schmedake for helpful discussions and suggestions towards my dissertation. I would also like to thank Dr. Menelaos Poutous for his kind guidance at most needed times.

This work was made possible with the generous help and guidance from my mentors and collaborators within the Center for Metamaterials. I would like to thank Dr. Susanne Lee from L3Harris for helpful discussions and encouragement. I am very grateful for Dr. Stefan Schöche, Dr. Craig Herzinger and Dr. James Hilfiker from J. A. Woollam for valuable discussions and help with THz ellipsometry. I would like to also express my gratitude to J. A. Woollam foundation and Dr. John Woollam.

I would like to thank Scott Williams and Dr. Jeffery Thousand for their help with additive manufacturing processes and discussions towards my research.

I am very grateful for my colleagues from Hofmann research group - Dr. Yanzeng Li for being a great inspiration for the group, Micheal McLamb and Paige Stinson for being hard-working, kind lab mates who are always willing to help me in research and life and are open to have discussions with me. I will not forget our Hawaiian shirt Fridays (and carry on with it).

I would like to also acknowledge my friends and classmates from UNCC. I cannot name everyone here but I would like to mention Mehnaz Tarannum, Sabeeh Irfan Ahmad and Chris Avery for being their diligent selves who have encouraged me to be better throughout my PhD.

Lastly I would like to thank my family. Parents, grandma, uncles, aunts and cousins for being supportive of what I choose to pursue and motivating me from back home.

To my dear little sister: I always wish that your shiny days will be brighter than mines will ever be. Unnie loves you.

TABLE OF CONTENTS

LIST OF TABLES

LIST OF FIGURES

CHAPTER 1: INTRODUCTION

1.1 Overview

Terahertz (THz) radiation is one of the most widely used non-ionizing illumination today in areas such as wireless communication, non-destructive quality inspection, medical, and security imaging applications [1, 2, 3, 4, 5]. Interest in manufacturing and rapid prototyping of optical components suitable for the THz spectral range, therefore, has been also increasing. In recent years, additive manufacturing of THz optical components including lenses, [6] gratings, [7] and waveguides [8] have been actively explored. Additive manufacturing of THz optics is a very attractive concept as it allows rapid fabrication of optics with arbitrary shapes at low-cost, enabling effective optimization of THz optical systems.

Additively manufactured THz optics to date have been primarily demonstrated using fused filament deposition-based techniques, which is one of the most frequently used polymer-based additive manufacturing methods [9, 10]. Despite its advantages in low fabrication costs and variety in material selection, fused filament deposition inherently suffers the limitation in spatial resolutions governed by mechanical factors including the nozzle diameter through which the materials are applied [11]. Stereolithography, on the other hand, has been demonstrated to achieve resolution on the order of 10 µm and substantially better surface roughness compared to other fabrication techniques [12]. In addition, metamaterials operating in the infrared or further wavelength ranges can be realized by stereolithography as its superior resolution allows flexible tailoring of the geometry on sub-wavelength scales. Therefore, stereolithography-based techniques are ideal methods of fabrication for optical components as well as metamaterials designed for the THz spectral ranges [13, 14].

In spite of the rapidly increasing interest in additively manufactured THz and infrared optical components, accurate infrared and THz dielectric function data on polymers compatible with stereolithography-based systems are scarce [15, 16]. This lack of information impedes the simulation-based design and demonstration of components with novel THz optical properties composed of such polymers. Attaining accurate knowledge of the complex dielectric function of the materials used for stereolithography will enable realization of stereolithographically fabricated THz optical components and metamaterials with tailored optical properties.

This work encompasses optical characterization of materials, optical components, and anisotropic metamaterials in the THz spectral range. THz optical properties of several polymethacrylates compatible with commercial stereolithography systems were determined for the first time. Utilizing the determined optical properties, simulation-based design of THz optical components including one-dimensional photonic crystals and off-axis parabolic reflectors were performed. The designed components were then stereolithographically fabricated and experimentally demonstrated in the THz spectral range. In addition, THz anisotropic metamaterials have been stereolithographically fabricated and studied here. The results obtained in the course of this work have been reported in several peer-reviewed publications, which are summarized on page 141. The content of chapter 2 through 6 of this thesis is based on a selection of these publications. The present work is organized as follows:

Stereolithography and spectroscopic ellipsometry, which are crucial techniques for fabricating and studying the materials and optical components demonstrated in this work, will be introduced in the rest of this chapter. Brief review on the fundamentals and working principles of a stereolithography system are provided in chapter 1.2 to help understand the fabrication process of the THz components discussed here. Chapter 1.3 introduces spectroscopic ellipsometry and outlines the Jones and Mueller matrix formalism used to describe optical response of the materials and anisotropic metamaterials investigated throughout this work in terms of stratified optical systems.

Chapter 2 focuses on the complex dielectric functions of several polymethacrylates frequently used with commercial stereolithography systems. Spectroscopic ellipsometry data sets from the THz to the mid-infrared spectral range and the analysis using stratified layer optical model calculations with parameterized model dielectric functions are provided.

In Chapter 3, THz one-dimensional photonic crystals that exhibit THz frequency bands with very high reflectivity are introduced. By employing Bruggeman effective medium approximation, photonic crystals were achieved from a single material using a single-step stereolithographic fabrication. Defect modes as a highly localized transmission within the photonic bandgap of such THz photonic crystals are also discussed in this chapter. Chapter 4 illustrates the mechanical tuning of spectral position of the photonic bandgap achieved by applying mechanical force to the crystals as well as shift of the spectral position of defect modes achieved by mechanical translation.

Chapter 5 includes the first demonstration of stereolithographically fabricated THz anisotropic metamaterials and the THz 1D photonic crystal structures which incorporate such anisotropic metamaterials. The anisotropic photonic crystals exhibit polarization direction dependent photonic bandgaps. In chapter 6, two different approaches for stereolithographically fabricating THz reflective optics with curved surfaces are studied. This work is concluded with a summary of the demonstrations and a brief outlook in Chapter 7.

1.2 Stereolithography

Stereolithography is an additive manufacturing process based on curing or solidification of liquid photosensitive resin that employs electromagnetic radiation as a source of energy required to induce a chemical reaction (curing reaction) [12]. Depending on the photopolymerization principle (single-photon or two-photon polymerization) and the type of light source used for the solidification (ultraviolet or infrared radiation), stereolithography can be further categorized [12]. In this thesis, the term stereolithography is used to describe a system based on single-photon polymerization employing a ultraviolet (UV) laser, which is technically relevant to the demonstrations explored here.

Stereolithography is a single-photon photo-fabrication approach where three-dimensional (3D) shapes are built by selectively polymerizing photosensitive resins using UV radiation. A stereolithography system employing direct laser writing approach commonly consists of a container containing a photosensitive resin, a movable platform on which the part is built, a UV laser to irradiate and cure the polymer, and a dynamic mirror system to direct the laser beam [17].

Typical stereolithographic fabrication processes involve a computer-aided design (CAD) file which describes the geometry and size of the parts to be built. Based on the CAD file, the coordinates of triangles that make up the surface of the designed 3D part are recorded into a STL (Stereolithography) file. The designed structure is then virtually sliced into layers of the specified thickness (typically ranges from 25 - 100 µm) for the layer-by-layer fabrication process. Finally, these data are uploaded to the stereolithography system to be manufactured [17].

The manufacturing of 3D objects by stereolithography is based on the spatially controlled solidification of a liquid resin by photopolymerization. By controlling the dynamic mirrors, UV laser beam is directed over the surface of a photosensitive resin, curing a cross sectional layer of the part that comprise a set of elementary volumes, referred to as voxels [17].

The resin is photopolymerized to a defined depth, adhering to the printing platform. The curing reaction of stereolithographic resins can be described as an exothermic, chemical cross-linking reaction process that results in highly cross-linked 3D network of polymer that is insoluble and infusible [18]. Once the first layer is polymerized onto the building platform, the platform is moved away by the selected layer thickness and

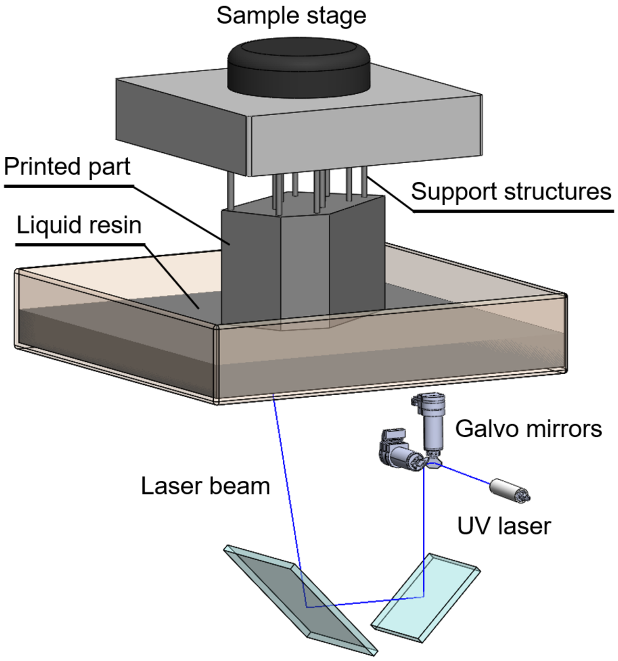

Figure 1.1: Simplified diagram of a typical stereolithography system. A UV laser beam guided by mirrors photopolymerizes the liquid resin on the fabrication platform layer by layer to form a 3D object.

the built layer is re-coated with liquid resin. The next layer is then cured, and these steps are repeated to construct a solid, 3D object. After draining and rinsing the excess resin from the as-fabricated structure, post-curing process is often involved to improve mechanical properties of the parts by ensuring thorough conversion of reactive groups within the polymer [19].

The curing process of photosensitive resin has been well studied and detailed descriptions on this topic can be found in literature [20, 21, 22]. Further details regarding the stereolithography process and its applications can be found in a series of references and references within [23, 24, 25, 26].

1.3 Spectroscopic Ellipsometry

When designing optical components or metamaterials, accurate knowledge on the optical properties of the constituent materials is essential for performing numerical simulations to predict the response prior to fabrication. Spectroscopic ellipsometry is employed here to acquire precise complex dielectric function data for a number of polymethacrylates compatible with commercial stereolithography systems and analyze anisotropic optical response of stereolithographically fabricated THz metamaterials.

Spectroscopic ellipsometry is an optical measurement technique that is widely used to characterize thin films, surfaces and material microstructure [27]. While ellipsometry can be performed in reflection (incident beam reflected from a sample) or transmission (incident beam transmitted through a sample) configuration, all ellipsometric measurements included in this dissertation were performed using reflection configuration. Thus, discussion regarding spectroscopic ellipsometry here will focus on reflection configuration. Ellipsometry measures the change in polarization state of light induced by a sample and determines the complex ratio of polarized wave components [28]. This ratio is typically expressed as two real-valued ellipsometric parameters Ψ and Δ. Ψ and Δ values are related to the sample-induced variations in two orthogonal polarization states relative to each other in terms of magnitude and phase. The electromagnetic plane wave responses from the samples measured with spectroscopic ellipsometry are commonly represented utilizing the Jones or the Mueller matrix formalism, which are described further in section below.

In general, data analysis for the spectroscopic ellipsometry data requires stratified layer model calculation to describe an optical system that modifies the polarization state of the light, in other words the sample [28]. Choosing appropriate oscillator models to employ for the stratified model calculations also plays an important role in drawing meaningful results from the ellipsometric data. An overview of ellipsometric data analysis through stratified layer model calculations are described further in sections below.

1.3.1 Jones and Mueller matrix formalism for ellipsometry

In reflection configuration ellipsometry, the interaction between a probing light beam and the surface of a sample can be written using the Jones vector representation. The 2×2 Jones matrix contains four complex-valued elements known as the polarized Fresnel reflection coefficients [27]:

$$\begin{bmatrix} E_{rp} \\ E_{rs} \end{bmatrix} = \begin{bmatrix} r_{pp} & r_{ps} \\ r_{sp} & r_{ss} \end{bmatrix} \begin{bmatrix} E_{ip} \\ E_{is} \end{bmatrix}, \tag{1.1}$$

where both incident and reflected electric fields (E_i and E_r) are represented by the Jones vectors with components polarized parallel (denoted by p) or perpendicular (denoted by s) to the plane of incidence.

In standard ellipsometry, the ellipsometric parameters Ψ and Δ do not depend on the polarization state of the incident light. The ellipsometric parameters Ψ and Δ can be expressed simply as a ratio of complex Fresnel reflection coefficients [27]:

$$\tan(\Psi)e^{i\Delta} \equiv \frac{r_p}{r_s}, \tag{1.2}$$

where the Fresnel reflection coefficients for orthogonally polarized components of light are denoted by r_p and r_s.

For isotropic samples, the off-diagonal elements of the Jones matrix r_{ps} and r_{sp} vanish and only on-diagonal elements r_{pp} and r_{ss}, the complex reflection coefficients for p- and s-polarization, become relevant.

The Jones matrix provides a complete mathematical presentation for fully polarized response where the sample is non-depolarizing. However partially polarized or unpolarized light can not be represented using Jones matrix. When depolarization is involved due to the factors such as thickness non-uniformity or backside-reflections from a transparent substrate, Mueller matrix and Stokes vector formalism can be used to describe such cases [29].

In situations where depolarization and partially polarized light are explored, Jones matrix fails to fully describe the sample response since it can only describe completely polarized light. Accurate description of unpolarized or partially polarized light requires Stokes vectors and Mueller matrix formalism. In terms of the p- and s-polarized coordinate system of the electromagnetic plane wave, the four real-valued Stokes parameters S_i, $i = 0 \ldots 3$, which have dimensions of intensities, are expressed as [27]:

$$\begin{aligned} S_0 &= I_p + I_s \ , \\ S_1 &= I_p - I_s \ , \\ S_2 &= I_{+45} - I_{-45} \ , \\ S_3 &= I_{\sigma+} - I_{\sigma-} \ , \end{aligned} \tag{1.3}$$

where I_p, I_s,I_{+45},I_{-45}, $I_{\sigma+}$, and $I_{\sigma-}$ denote the intensities for the p, s, $+45°$, $-45°$, right-, and left-handed circularly polarized light components, respectively. The Stokes parameter S_0 is proportional to the intensity of the light beam. Arranging the Stokes parameters into a column Stokes vector $\mathbf{S}$, the Mueller matrix $\mathbf{M}$ is defined by the Stokes vector before ($\mathbf{S}_{in}$) and after the interaction with an optical system ($\mathbf{S}_{out}$) as [27]:

$$\begin{pmatrix} S_0^{out} \\ S_1^{out} \\ S_2^{out} \\ S_3^{out} \end{pmatrix} = \begin{pmatrix} M_{11} & M_{12} & M_{13} & M_{14} \\ M_{21} & M_{22} & M_{23} & M_{24} \\ M_{31} & M_{32} & M_{33} & M_{34} \\ M_{41} & M_{42} & M_{43} & M_{44} \end{pmatrix} \begin{pmatrix} S_0^{in} \\ S_1^{in} \\ S_2^{in} \\ S_3^{in} \end{pmatrix} . \tag{1.4}$$

The Mueller matrix elements $M_{j,k}$ $(j, k = 1,\ 2,\ 3,\ 4)$ are commonly normalized by the M_{11} element such that all elements of the matrix have values ranging from -1 to 1. While Mueller matrix ellipsometry is employed to examine samples that exhibit optical anisotropy and/or depolarization, isotropic samples can be expressed using Mueller matrix as well. It is important to note that for isotropic samples, the off-diagonal elements of the Mueller matrix (M_{13}, M_{14}, M_{23}, M_{24}, M_{31}, M_{32}, M_{41}, and M_{42}) become zero and only on-diagonal elements have non-zero values. The off-diagonal elements of the Mueller matrix will become non-zero when anisotropy is present. Details of this concept, its use in ellipsometry, and its relation to the Jones matrix formalism can be found in refs. [27, 28, 29] and references within.

1.3.2 Analysis of Ellipsometric Data

In order to extract information such as thickness and the complex dielectric function ε of each sample constituents from measured ellipsometric data, stratified optical model calculations are performed [30]. Depending on the parameters of interest and the sample properties including layer sequence and anisotropy, different analysis approaches can be employed. Two common approaches of analyzing ellipsometric data through stratified layer calculations are the so-called wavelength-by wavelength analysis and the model dielectric function based analysis [31].

The wavelength-by-wavelength analysis, also known as point-by-point fit analysis, directly converts the experimental spectroscopic ellipsometry data Ψ and Δ to complex dielectric function independently for each wavelength. Thus for isotropic bulk samples with known thickness values, this method can be used to directly extract the complex dielectric function of the materials. Exact values of physically relevant parameters (such as resonance frequencies, amplitudes, and broadening parameters) can be also determined from the dielectric function drawn from the point-by-point fitting, by comparing the dielectric function data with a line shape model. While this is a useful approach for a bulk sample, it is not a preferable approach for stratified samples since the dielectric function and thickness of all other sample constituent must be known to correctly perform this conversion.

The model dielectric function based analysis is performed by fitting parameterized model dielectric functions to the experimental data for the entire spectrum, retaining Kramers-Kronig consistency throughout the procedure. It is generally considered more robust method, as it secures a direct connection between measured ellipsometric data and the physically relevant parameters. In addition, the number of free parameters are reduced dramatically as the measurement noise is excluded from the parametric models. In this dissertation, both analysis approaches were utilized during characterzation of polymethacrylates used for stereolithography.

During the data analysis, the physically relevant parameters, including resonance frequencies, amplitudes, broadenings, and layer thickness are varied until the best match is obtained between the experimental data and the model calculated data. The Levenberg-Marguardt algorithm is employed here for this fitting process, where the adjustable model parameters are varied until the mean square error (MSE) is minimized. The MSE is defined as the mismatch between the calculated and measured data sets and can be expressed as [32]:

$$MSE = \sqrt{\frac{1}{2N-M}\sum_{i=1}^{N}\left[\left(\frac{\Psi_i - \Psi_i^C}{\sigma_i^{\Psi}}\right)^2 + \left(\frac{\Delta_i - \Delta_i^C}{\sigma_i^{\Delta}}\right)^2\right]}, \tag{1.5}$$

where the total number of real-valued parameters varied during the fitting procedure is denoted as M. The total number of measured data pairs (Ψ_i, Δ_i) is expressed as N while their standard deviations are denoted by σ_i^{Ψ} and σ_i^{Δ}. Ellipsometric parameters calculated at photon energy of $E = \hbar\omega_i$ are represented as Ψ_i^C, Δ_i^C [30]. The details of thin film characterization via spectroscopic ellipsometry can be found in numerous publications [33, 34].

The standard model for analyzing spectroscopic ellipsometry data is based on an assumption that the constituent layers are homogeneous (isotropic or anisotropic) with smooth, plane-parallel interfaces. The assumption of homogeneity at the microscopic scale does not hold for a compound sample that is composed of multiple dielectrics interspersing with each other in a either disordered or ordered manner. In order to correctly analyze optical properties of such composite materials, well-known effective medium approximation (EMA) approaches are utilized. Amongst various EMA theories, Bruggeman EMA provides the best estimation of the "effective" optical properties of the layers with sub-wavelength scale inclusions that comprise optical structures demonstrated in this work [35].

In a two-constituent based Bruggeman topology, one of the constituents is considered "inclusion" while the other is referred to as "host". The inclusion and host materials cannot be differentiated topologically and are intermingled with each other in a symmetric manner in the Bruggeman topology. Effective medium of such composite materials can be calculated by knowing the optical properties of constituent materials and their volume fraction. Bruggeman EMA is one of the most common effective medium approximation models, applicable for a wide range of mixing effects including surface and interfacial roughness and index grading. This approximation method has been studied extensively and further details and examples where this method is applied can be found in numerous literature [35, 36, 37, 38]. The use of Bruggeman EMA to calculate effective medium properties of isotropic and anisotropic layers is also discussed throughout this work in chapters 3, 4, and 5.

REFERENCES

[1] J. Federici and L. Moeller, "Review of terahertz and subterahertz wireless communications," *J. Appl. Phys.* **107**, 6 (2010).

[2] J. P. Guillet, B. Recur, L. Frederique, B. Bousquet, L. Canioni, I. Manek-Hönninger, P. Desbarats, and P. Mounaix, "Review of terahertz tomography techniques," *J. Infrared Millim. Terahertz Waves* **35**, 382 (2014).

[3] A. J. Fitzgerald, E. Berry, N. N. Zinovev, G. C. Walker, M. A. Smith, and J. M. Chamberlain, "An introduction to medical imaging with coherent terahertz frequency radiation," *Phys. Med. Biol.* **47**, R67 (2002).

[4] Z. D. Taylor, R. S. Singh, D. B. Bennett, P. Tewari, C. P. Kealey, N. Bajwa, M. O. Culjat, A. Stojadinovic, H. Lee, J.-P. Hubschman, E. R. Brown, and W. S. Grundfest, "Thz medical imaging: in vivo hydration sensing," *IEEE Trans. Terahertz Sci. Technol.* **1**, 201 (2011).

[5] M. C. Kemp, P. F. Taday, B. E. Cole, J. A. Cluff, A. J. Fitzgerald, and W. R. Tribe, "Security applications of terahertz technology," *Terahertz for Military and Security Applications*, **5070**, 44 (2003).

[6] W. D. Furlan, V. Ferrando, J. A. Monsoriu, P. Zagrajek, E. Czerwińska, and M. Szustakowski, "3d printed diffractive terahertz lenses," *Opt. Lett.* **41**, 1748 (2016).

[7] A. D. Squires, E. Constable, and R. A. Lewis, "3d printed terahertz diffraction gratings and lenses," *J. Infrared Millim. Terahertz Waves* **36**, 72 (2015).

[8] M. Weidenbach, D. Jahn, A. Rehn, S. F. Busch, F. Beltrán-Mejía, J. C. Balzer, and M. Koch, “3d printed dielectric rectangular waveguides, splitters and couplers for 120 ghz,” *Opt. Express* **24**, 28968 (2016).

[9] J. A. Colla, R. E. M. Vickers, M. Nancarrow, and R. A. Lewis, “3d printing metallised plastics as terahertz reflectors,” *J. Infrared Millim. Terahertz Waves* **40**, 752 (2019).

[10] S. Singh, G. Singh, C. Prakash, and S. Ramakrishna, “Current status and future directions of fused filament fabrication,” *J. Manuf. Process.* **55**, 288 (2020).

[11] J. Go, S. N. Schiffres, A. G. Stevens, and A. J. Hart, “Rate limits of additive manufacturing by fused filament fabrication and guidelines for high-throughput system design,” *Addit. Manuf.* **16**, 1 (2017).

[12] C. Schmidleithner and D. M. Kalaskar, “Stereolithography,” (IntechOpen, 2018).

[13] A. Macor, E. De Rijk, S. Alberti, T. Goodman, and J.-P. Ansermet, “Note: Three-dimensional stereolithography for millimeter wave and terahertz applications,” *Rev. Sci. Instrum.* **83**, 046103 (2012).

[14] W. J. Otter and S. Lucyszyn, “Hybrid 3-d-printing technology for tunable thz applications,” *Proc. IEEE* **105**, 756 (2017).

[15] S. Sahin, N. K. Nahar, and K. Sertel, “Dielectric properties of low-loss polymers for mmw and thz applications,” *J. Infrared Millim. Terahertz Waves* **40**, 557 (2019).

[16] N. Duangrit, B. Hong, A. D. Burnett, P. Akkaraekthalin, I. D. Robertson, and N. Somjit, “Terahertz dielectric property characterization of photopolymers for additive manufacturing,” *IEEE Access* **7**, 12339 (2019).

[17] P. J. Bártolo, Stereolithography: materials, processes and applications, (Springer Science & Business Media, 2011).

[18] E. Andrzejewska, "Photopolymerization kinetics of multifunctional monomers," *Prog. Polym. Sci.* **26**, 605 (2001).

[19] T. N. T. Decker, C.and Viet, D. Decker, and E. Weber-Koehl, "Uv-radiation curing of acrylate/epoxide systems," *Polymer* **42**, 5531 (2001).

[20] J.-P. Fouassier and J. F. Rabek, Radiation curing in polymer science and technology: Practical aspects and applications, (Springer Science & Business Media, 1993).

[21] J. G. Kloosterboer, "Network formation by chain crosslinking photopolymerization and its applications in electronics," *Adv. Polym. Sci.* **84**, 1 (1988).

[22] C. Decker, "Photoinitiated crosslinking polymerisation," *Prog. Polym. Sci.* **21**, 593 (1996).

[23] F. Doreau, C. Chaput, and T. Chartier, "Stereolithography for manufacturing ceramic parts," *Adv. Eng. Mater.* **2**, 493 (2000).

[24] J. Z. Manapat, Q. Chen, P. Ye, and R. C. Advincula, "3d printing of polymer nanocomposites via stereolithography," *Macromol. Mater. Eng.* **302**, 1600553 (2017).

[25] F. P. W. Melchels, J. Feijen, and D. W. Grijpma, "A review on stereolithography and its applications in biomedical engineering," *Biomaterials* **31**, 6121 (2010).

[26] A. Bagheri and J. Jin, "Photopolymerization in 3d printing," *ACS Appl. Polym. Mater.* **1**, 593 (2019).

[27] H. Fujiwara, Spectroscopic Ellipsometry: Principles and Applications, (John Wiley & Sons, 2007).

[28] R. M. A. Azzam and N. M. Bashara, Ellipsometry and Polarized Light, (North-Holland, Amsterdam, 1977).

[29] M. Schubert, “Generalized ellipsometry and complex optical systems,” *Thin Solid Films* **313**, 323 (1998).

[30] G. E. Jellison, “Spectroscopic ellipsometry data analysis: measured versus calculatedquantities,” *Thin Solid Films* **313-314**, 33 (1998).

[31] J. N. Hilfiker and T. Tiwald, “Dielectric function modeling,” in Spectroscopic Ellipsometry for Photovoltaics, 115–153, (Springer, 2018).

[32] W. H. Press, W. T. Vetterling, S. A. Teukolsky, and B. P. Flannery, Numerical recipes, (Cambridge university press Cambridge, 1986).

[33] J. B. Theeten and D. E. Aspnes, “Ellipsometry in thin film analysis,” *Annu. Rev. Mater. Sci.* **11**, 97 (1981).

[34] C. M. Herzinger, B. Johs, W. A. McGahan, J. A. Woollam, and W. Paulson, “Ellipsometric determination of optical constants for silicon and thermally grown silicon dioxide via a multi-sample, multi-wavelength, multi-angle investigation,” *J. Appl. Phys.* **83**, 3323 (1998).

[35] D. A. G. Bruggeman, “Dielectric constant and conductivity of mixtures of isotropic materials,” *Ann. Phys.(Leipzig)* **24**, 636 (1935).

[36] D. E. Aspnes, “Optical properties of thin films,” *Thin solid films* **89**, 249 (1982).

[37] D. Stroud, “The effective medium approximations: Some recent developments,” *Superlattices Microstruct.* **23**, 567 (1998).

[38] D. Schmidt, M. Schubert, “Anisotropic Bruggeman effective medium approaches for slanted columnar thin films,” *J. Appl. Phys.* **114**, 083510 (2013).

CHAPTER 2: THZ TO MID-INFRARED DIELECTRIC PROPERTIES OF POLYMETHACRYLATES FOR STEREOLITHOGRAPHY

2.1 THz to mid-infrared dielectric properties of polymethacrylates for stereolithography

The fabrication of terahertz (THz) optics with arbitrary shapes via polymethacrylate-based stereolithography is very attractive as it may offer a rapid, low-cost avenue towards optimized THz imaging applications.[1] In order to design such THz optical components appropriately, accurate knowledge of the complex dielectric function of the materials used for stereolithographic fabrication is crucial. In this paper we report on the complex dielectric functions of several polymethacrylates frequently used for stereolithographic fabrication. Spectroscopic ellipsometry data sets from the THz to mid-infrared spectral range were obtained from isotropically cross-linked polymethacrylate samples. The data sets were analyzed using stratified layer optical model calculations with parameterized model dielectric functions. While the infrared spectral range is dominated by a number of strong absorption features with Gaussian profiles, these materials are found to exhibit only weak absorption in the THz frequency range. In conclusion, we find that thin transmissive THz optics can be efficiently fabricated using polymethacrylate-based stereolithographic fabrication.

2.1.1 Introduction

THz optical components produced by additive manufacturing techniques have received considerable interest in recent years as cost effective rapid-prototyping solutions

---

[1] Reprinted by permission from Springer Nature Customer Service Centre GmbH: Springer S. Park, Y. Li, D. B. Fullager, S. Schöche, C. Herzinger, G. D. Boreman, and T. Hofmann, "Terahertz to Mid-infrared Dielectric Properties of Polymethacrylates for Stereolithographic Single Layer Assembly," *J. Infrared, Millimeter, Terahertz Waves* **40**, 971 - 979 (2019). © 2019

for THz optical components such as lenses [1], filters and waveguides [2, 3]. A large body of literature has reported on the performance and optical properties of THz optical components fabricated using 3D printing techniques [4, 5, 6, 7].

Several publications are dedicated to the THz optical properties of the materials suitable for 3D printing [4, 5]. However, the major focus to date is on materials and optical components fabricated using fused deposition-based techniques [1, 2, 4]. The advantages of fused deposition-based techniques are primarily the low instrument and fabrication costs as well as the large variety of compatible materials [8]. The resolution and surface finish of fused deposition-based techniques are limited by the nozzle diameter through which the materials are applied. Current state-of-the-art fused deposition-based printers have nozzle diameters that range on the order of several hundred µm [9, 10]. Stereolithography, in contrast, has been demonstrated to achieve resolution on the order of 10 µm and substantially better surface finish compared to other fabrication techniques [11, 12]. Therefore, stereolithography-based techniques are ideal methods of fabrication for THz optical components [13, 14].

Despite the rapidly increasing interest in 3D printed THz and infrared optical components, accurate infrared and THz dielectric function data on polymethacrylates available for stereolithography-based fabrication have not been reported yet. This hinders the development of optical components composed of such polymethacrylates and impedes the progress in simulation-based design of metamaterials with novel THz optical properties.

In this paper we report on the first ellipsometric measurements and the complex dielectric functions of stereolithography-compatible polymethacrylates in the mid-infrared and THz spectral range. Three different commercially available polymethacrylates (Formlabs Inc.) were investigated. We find that the polymethacrylates exhibit very similar THz optical properties but display characteristic differences in the absorption bands observed in the infrared spectral range. In the THz spectral range all investigated materials show sufficient transparency to allow the fabrication of thin transmissive optical components, in particular for the lower THz frequency range. A parameterized model dielectric function composed of harmonic oscillators with Gaussian broadening is derived and discussed.

2.1.2 Experiment

2.1.2.1 Sample Preparation

The samples studied here were prepared using UV-induced polymerization of the methacrylate-based resins in a mold as described below. This fabrication process ensured that the surface roughness is sufficiently small for infrared ellipsometry. For each sample, approximately 2 ml of resin was applied in between two microscope slides placed parallel to each other on a glass plate. Subsequently, a second glass plate was set on top of the spacers to shape the resin into a thin slab. The assembly was then placed in a UV oven (UVO cleaner model no. 42, Jelight Company Inc.) and was cured for 15 minutes until the resin was fully polymerized. As a result, the polymerized resin samples have parallel interfaces with low surface roughness and are suitable for accurate ellipsometric measurements in the infrared and THz spectral range. This fabrication approach was applied for three different methacrylate-based resins, which are commercially available (Formlabs Inc.) described by the vendor as "castable" (sample 1), "tough" (sample 2), and "black" (sample 3). All investigated samples have a nominal thickness of 1 mm.

2.1.2.2 Data Acquisition and Analysis

The polymethacrylate samples were investigated using a commercial infrared ellipsometer (Mark I IR-VASE, J.A. Woollam Company Inc.) and a commercial THz ellipsometer (THz-VASE, J.A. Woollam Company Inc.). The IR ellipsometer operates in a polarizer − sample − rotating compensator − analyzer configuration, while the THz ellipsometer uses a rotating polarizer − sample − rotating compensator − analyzer configuration as detailed in Ref. [15]. The infrared ellipsometer is equipped with a Fourier transform infrared (FTIR) spectrometer and employs a deuterated-triglycine sulfate (DTGS) detector. The THz ellipsometer is equipped with backward-wave oscillator source operating in the range from 100 to 180 GHz. Schottky diode frequency multipliers are used to extend the spectral range from 0.65 to 0.95 THz. A Golay cell is employed as a detector in the THz-VASE. Ellipsometric Ψ- and Δ-spectra were obtained in the infrared spectral range from 300 to 4000 cm^{-1} (9 to 120 THz) with a resolution of 4 cm^{-1} (0.1 THz) at three angles of incidence: $\Phi_a = 65^\circ$, 70°, and 75°. The THz ellipsometric data were obtained over range from 22 to 32 cm^{-1} (0.65 to 0.95 THz) with a resolution of 0.2 cm^{-1} (5 GHz) at the same angles of incidence as for the infrared data.

The optical modeling and data analysis were performed using a commercial ellipsometry data analysis software package (WVASE32$^{\mathrm{TM}}$, J.A. Woollam Company). The complete ellipsometric data set obtained for each sample was analyzed using a three layer optical model composed of air − polymethacrylate − air. A model dielectric function was used to describe the infrared and THz optical response of the polymethacrylates. The model dielectric function incorporates a sum of Gaussian oscillators:

$$\varepsilon(\omega) = \varepsilon_1(\omega) + i\varepsilon_2(\omega) = \varepsilon_\infty + \sum_i \varepsilon_{\mathrm{Gau}}(A, \Gamma, \omega, \omega_o), \tag{2.1}$$

where the function $\varepsilon_{\mathrm{Gau}}(A, \Gamma, \omega, \omega_o)$ indicates an oscillator with Gaussian broadening. The oscillator amplitude, broadening, and resonance frequency are designated by A, Γ, ω_o, respectively. The oscillators are given analytically by their Gaussian form for the imaginary part $\varepsilon_2^{\mathrm{Gau}}(\omega)$ of the complex dielectric function $\varepsilon(\omega)$:

$$\varepsilon_2^{\mathrm{Gau}}(\omega) = A \exp\left(-\left(\frac{\omega - \omega_o}{f \cdot \Gamma}\right)^2\right) + A \exp\left(-\left(\frac{\omega + \omega_o}{f \cdot \Gamma}\right)^2\right), \tag{2.2}$$

where $1/f = 2\sqrt{\ln(2)}$. The corresponding values for $\varepsilon_1^{\mathrm{Gau}}(\omega)$ are determined by Kramers-Kronig integration of Eq. (2.2) during the Levenberg-Marquardt-based lineshape analysis of the experimental Ψ- and Δ-spectra.

During the lineshape analysis, relevant model parameters are varied until the best match between calculated model and experimental ellipsometry data is achieved. The best-model calculated spectra shown in Figs. 2.1 and 2.2 require 14 Gaussian oscillators with frequencies ranging from 40 to 3500 cm^{-1} for sample 1. The analysis for samples 2 and 3 required a model dielectric function composed of 15 distinct Gaussian oscillators in this energy range in order to describe the experimentally observed lineshapes.

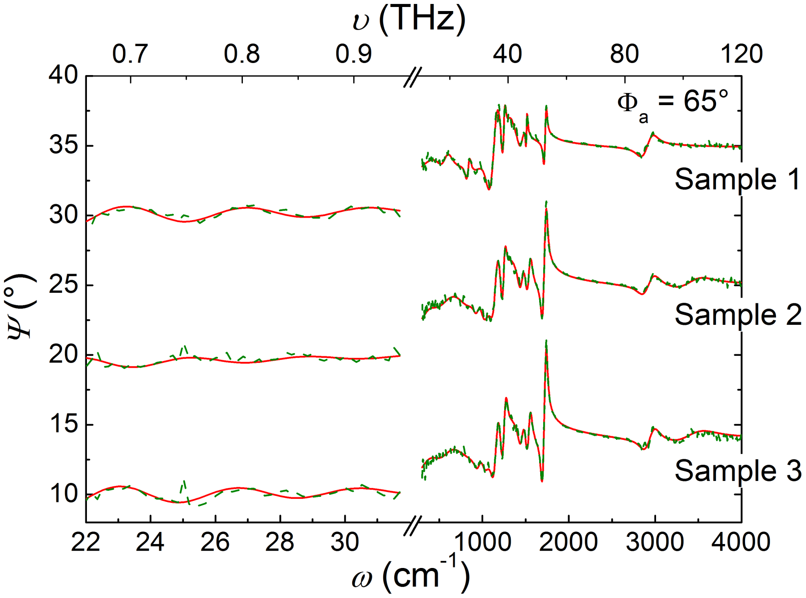

Figure 2.1: Best-model calculated (red solid lines) and experimental (dashed green lines) Ψ-spectra obtained at $\Phi_a = 65°$ for sample 1, 2, and 3. The infrared range is dominated by a number of distinct absorption bands while the THz range shows Fabry-Pérot oscillations as a result of the plane parallel interfaces of the samples. The Ψ-spectra of sample 2 and 3 are shifted with respect to the Ψ-spectrum of sample 1 by a constant offset of 12° and 22°, respectively.

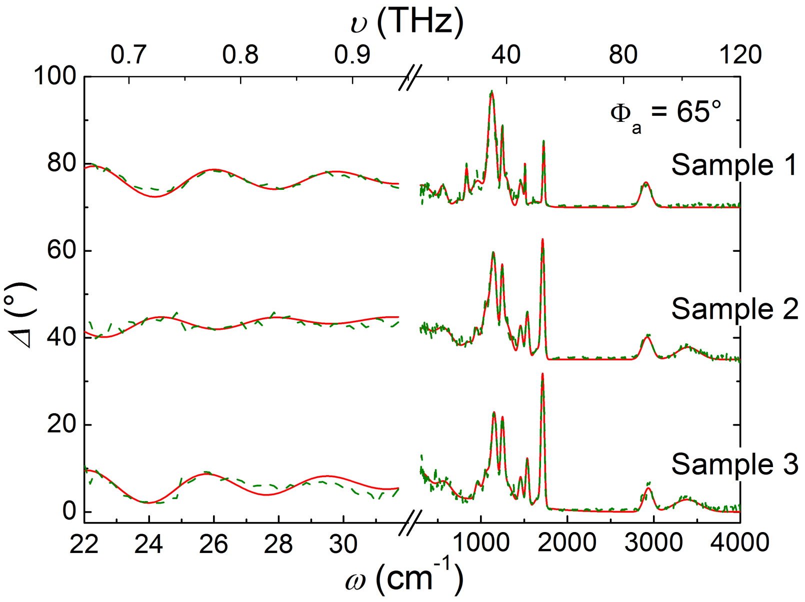

Figure 2.2: Best-model calculated (red solid lines) and experimental (dashed green lines) Δ-spectra obtained at $\Phi_a = 65°$ for sample 1, 2, and 3. Similar to the Ψ-spectra shown in Fig. 2.1, the infrared range is dominated by several distinct absorption bands while the THz range exhibits Fabry-Pérot oscillations as a result of the plane parallel interfaces of the samples. The Δ-spectra of sample 2 and 3 are shifted with respect to the Δ-spectrum of sample 1 by a constant offset of 35° and 70°, respectively.

2.1.3 Results and discussion

Figure 2.1 illustrates the experimental (dashed green lines) and the best-model calculated (solid red lines) Ψ-spectra of all three samples at the angle of incidence Φ_a $= 65°$ for the spectral range from 22 to 4000 cm^{-1}. The corresponding Δ-spectra are shown in Fig. 2.2. Note that experimental Ψ- and Δ-spectra were obtained for $\Phi_a = 65°, 70°$, and 75° and were analyzed simultaneously. Only the data for $\Phi_a =$ 65° is shown here for clarity. The experimental and best-model calculated data are in very good agreement for all investigated samples. All three samples show a very similar THz and infrared response where Fabry-Pérot oscillations are observed in the range from 22 to 32 cm^{-1} (0.65 to 0.95 THz) and distinct absorption bands are found in the range from 300 to 4000 cm^{-1} (9 to 120 THz).

A subtle damping in the Fabry-Pérot oscillations in Fig. 2.1 and 2.2 can be noticed.

This is accounted for in the model with a broad, shallow oscillator at $\omega = 40$ cm^{-1}. While the Fabry-Pérot oscillations of samples 1 and 3 have very similar amplitudes, the amplitudes of the Fabry-Pérot oscillations for samples 2 are distinctly smaller, indicating a lower transparency in this spectral range for sample 2.

Although very similar at a first glance, the investigated polymethacrylates show subtle differences in the mid-infrared spectral range from $\omega = 500$ to 2000 cm^{-1}. In this spectral range, sample 1 exhibits a peak at approximately 800 cm^{-1}, which is not observed in sample 2 and 3. At higher wavenumbers, at approximately 3400 cm^{-1}, samples 2 and 3 show a distinct absorption peak that is not present in sample 1. Thus, sample 1 can be easily distinguished from the other investigated polymethacrylate samples by its unique infrared fingerprint. The polymethacrylates in sample 2 and 3, however, show a very similar response in the infrared spectral range. Thus, a differentiation between the two materials in this spectral range requires quantification of oscillator amplitude and broadening parameters.

Figs. 2.3 and 2.4 show the real and imaginary parts of the model dielectric functions $\varepsilon(\omega)$ of all three samples for comparison. As discussed, all samples show similar responses in the infrared and THz ellipsometric data shown in Figs. 2.1 and 2.2 and correspondingly, the model dielectric functions of these samples are very similar. Strong absorption bands can be identified in the range from $\omega = 500$ to 2000 cm^{-1}. This allows a fingerprint identification of the materials in this spectral range [16].

In the THz spectral range from 0.65 to 0.95 THz (22 to 32 cm^{-1}) the permittivity for the samples shows little dispersion and absorption, which results in the Fabry-Pérot oscillations in these layers with plane parallel interfaces as seen in Figs. 2.1 and 2.2. Sample 1 shows the smallest $\varepsilon_2(\omega)$ while sample 2 shows the largest $\varepsilon_2(\omega)$, which makes the material in sample 1 ("castable", Formlabs Inc.) more suitable for transmissive optics. In comparison with the materials commonly used for fused deposition-based fabrication techniques, the absorption coefficients of the investigated materials are comparable. All samples exhibit absorption coefficient values larger than 10 cm^{-1} over the range from 0.65 to 0.95 THz, which is similar to that of nylon and polylactic acid 90. Polystyrene and butadiene over the same spectral range exhibit values below 5 cm^{-1} [4]. Here we account for the absorption in this spectral range by using a broad and shallow Gaussian oscillator, which is located in the spectral gap between operational ranges of the THz and infrared ellipsometers. Its resonance frequency was approximated at $\omega = 40$ cm^{-1}, which was not further varied during the model analysis.

Tables 2.1 and 2.2 summarize the best-model oscillator parameters for the dielectric response of the polymethacrylates in sample 1, 2, and 3 for comparison. The oscillator frequency ω_o and broadening Γ are given in units of cm^{-1}, while amplitude A is dimensionless. Error bars in parentheses represent the 90% confidence limits of the respective oscillator parameters.

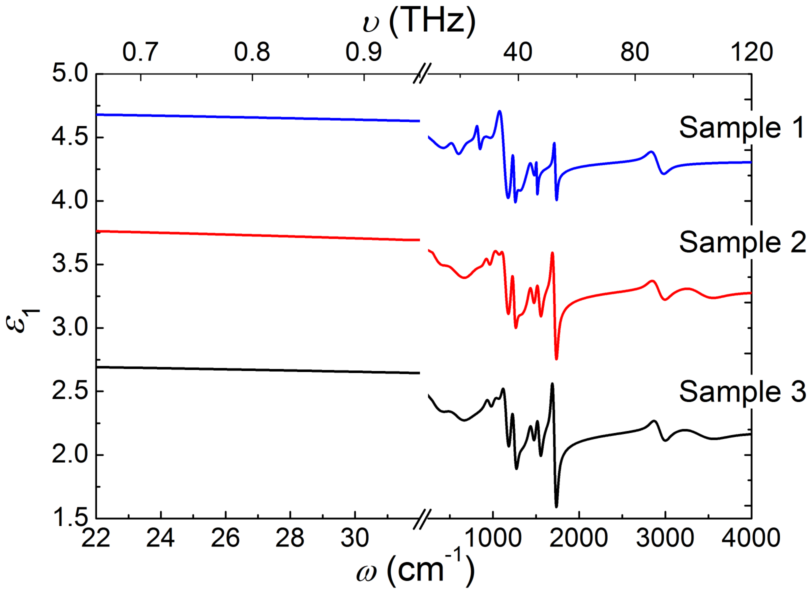

Figure 2.3: Best-model calculated real part of the complex dielectric function $\varepsilon(\omega)$ for sample 1, 2, and 3 are shown in solid lines. The major contributions to the dispersive behavior of all three samples occur in spectral range from 300 to 4000 cm^{-1}. The best-model parameters of the model dielectric function are given in Tabs. 2.1 and 2.2. Note that the $\varepsilon_1(\omega)$-spectra of sample 2 and 1 are shifted with respect to the $\varepsilon_1(\omega)$-spectrum of sample 3 by a constant offset of 1 and 2, respectively.

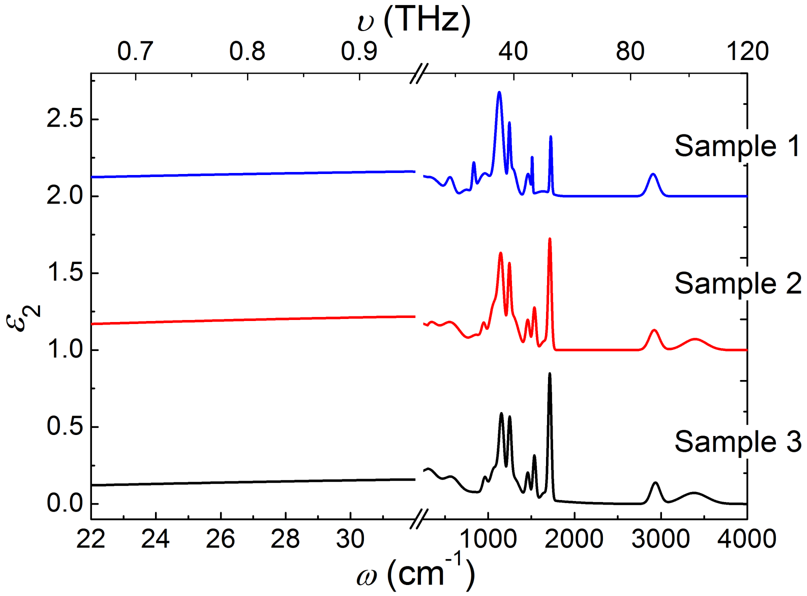

Figure 2.4: Best-model calculated imaginary part of the complex dielectric function $\varepsilon(\omega)$ for sample 1, 2, and 3 are shown in solid lines. The major contributions to the absorptive behavior of all three samples occur in infrared spectral range from 300 to 4000 cm^{-1}, while only a broad and shallow absorption was observed throughout the THz range. The best-model parameters are given in Tabs. 2.1 and 2.2. Note that the $\varepsilon_2(\omega)$ spectra of sample 2 and 1 are shifted with respect to the $\varepsilon_2(\omega)$ spectrum of sample 3 by a constant offset of 1 and 2, respectively.

2.1.4 Summary and conclusion

In this work we report accurate complex dielectric function values of three different polymethacrylates that are available for stereolithography-based manufacturing with commercial 3D printers in the infrared and THz spectral range. A model dielectric function composed of multiple oscillators with Gaussian broadening was found to appropriately render the THz and infrared ellipsometric responses. While the investigated materials are transparent in the THz spectral range, the infrared spectral range is dominated by distinct absorption bands. In contrast to materials commonly used for fused deposition-based fabrication techniques, such as acrylonitrile butadiene styrene or polystyrene, polymethacrylates analyzed here exhibit relatively high absorption across THz range [4]. However they are still sufficiently transparent for the fabrication of thin transparent THz optics, such as Fresnel lenses. We antici-

Table 2.1: Comparison of the best-model oscillator energies of the absorption bands identified for samples 1-3 in the range from 22 to 4000 cm^{-1}(0.65 to 120 THz). The parentheses indicate a 90% confidence interval for the corresponding digits.

	Sample 1	Sample 2	Sample 3
Number	ω_o (cm^{-1})	ω_o (cm^{-1})	ω_o (cm^{-1})
1	40*	40*	40*
2	318 (28)	322 (29)	292 (18)
3	564 (6)	557 (29)	578 (23)
4	744 (13)	874 (23)	739 (314)
5	834 (1)	949 (3)	961 (4)
6	962 (4)	1070 (9)	1070 (7)
7	1130 (1)	1149 (1)	1156 (1)
8	1245.7 (4)	1245 (1)	1249 (1)
9	1286 (4)	1281 (7)	1297 (21)
10	1461 (1)	1460 (1)	1459 (1)
11	1510.3 (4)	1536 (1)	1535.8 (4)
12	1635 (13)	1655 (11)	1648 (7)
13	1725.5 (3)	1725.5 (3)	1713.6 (2)
14	2909 (2)	2922 (2)	2935 (2)
15	-	3395 (7)	3382 (7)

* Value not further varied during the fit process.

Table 2.2: Comparison of the best-model parameters for the amplitude and broadening of the Gaussian oscillators identified for samples 1-3 with energies as shown in Tab. 2.1 in the range from 22 to 4000 cm^{-1}(0.65 to 120 THz). The parentheses indicate a 90% confidence interval for the corresponding digits.

	Sample 1		Sample 2		Sample 3	
Number	A	Γ (cm^{-1})	A	Γ (cm^{-1})	A	Γ (cm^{-1})
1	0.164 (14)	59 (61)	0.234 (19)	59 (49)	0.164 (14)	56 (40)
2	0.125 (20)	306 (86)	0.14 (5)	172 (84)	0.186 (29)	279 (65)
3	0.103 (19)	95 (17)	0.182 (9)	310 (87)	0.098 (19)	199 (37)
4	0.039 (6)	120 (39)	0.088 (15)	174 (73)	0.081 (18)	1474 (305)
5	0.177 (12)	36 (3)	0.107 (32)	57 (11)	0.094 (10)	59 (8)
6	0.149 (4)	179 (16)	0.297 (17)	121 (20)	0.162 (49)	102 (20)
7	0.665 (7)	99.5 (18)	0.508 (65)	70 (5)	0.495 (33)	68 (4)
8	0.354 (1)	29.3 (13)	0.366 (19)	37 (2)	0.423 (40)	46 (3)
9	0.176 (6)	98 (7)	0.225 (9)	158 (12)	0.117 (14)	140 (34)
10	0.140 (6)	61 (4)	0.191 (6)	55 (3)	0.160 (7)	50 (3)
11	0.231 (1)	13 (1)	0.275 (6)	45 (1)	0.279 (7)	41 (1)
12	0.032 (3)	210 (28)	0.060 (5)	103 (20)	0.044 (5)	72 (16)
13	0.372 (8)	24.7 (7)	0.704 (16)	42 (1)	0.821 (8)	42.5 (5)
14	0.144 (4)	133 (4)	0.1304 (4)	139 (5)	0.138 (4)	124 (4)
15	-	-	0.072 (4)	305 (17)	0.072 (3)	353 (18)

pate that the parameterized dielectric functions reported here will help to improve first-principle calculations of the infrared and THz optical responses of 2D and 3D structures composed of these materials.

2.2 THz optical properties of polymethacrylates after thermal annealing

Polymer based stereolithographic additive manufacturing has been established for the rapid and low-cost fabrication of THz optical components due to its ability to construct complex 3D geometries with high resolution.[2] For polymer based or integrated optics, thermal annealing processes are often used to optimize material properties. However, despite the growing interest in THz optics fabricated using stereolithography, the effects of thermal annealing on the THz dielectric properties of polymethacrylates compatible with stereolithography has not been studied yet. In this manuscript we report on the THz ellipsometric response of thermally annealed polymethacrylates prepared using UV polymerization. Our findings indicate that the investigated polymethacrylate maintain a stable optical response in THz spectral range from 650 to 950 GHz after thermal annealing at temperatures up to 70 °C for several hours.

2.2.1 Introduction

Fabrication of THz optical components using additive manufacturing methods has been reported as an efficient alternative to long established fabrication routes such as molding or single-point diamond machining [1, 2, 3]. THz optical components have been primarily fabricated using fused filament deposition, which allows the deposition of a wide range of THz transparent materials. The main advantages of fused filament deposition are the lower instrument and material costs. However, fused filament deposition suffers from a low spatial resolution and surface finish, which is mainly limited by the nozzle diameter [8]. Stereolithography, on the other hand, has been reported to accomplish spatial resolutions on the order of 10 µm. In addition, the surface finish of components fabricated by stereolithography is substantially better

---

[2] Reprinted with permission from S. Park, Y. Li, D. B. Fullager, M. Lata, P. Kühne, V. Darakchieva, T. Hofmann, "Terahertz optical properties of metamaterials and optical components fabricated using polymer-based additive manufacturing," *J. Vac. Sci. Technol. B* **37**, 062924 (2019). © 2019, American Vacuum Society.

compared to other additive manufacturing fabrication techniques [11, 12].

Recently, metalization of stereolithographically fabricated parts was demonstrated to be an effective way of prototyping reflective THz optics [14, 17]. Furthermore, polymers compatible with stereolithography were found to be transparent in THz spectral range to potentially enable the fabrication of transmissive optics [18]. Thus, stereolithographic fabrication may open up new pathways for the manufacturing of polymethacrylate-based or integrated THz optical components.

Polymers are known to undergo morphological changes when heated to temperatures below the melting point, or annealed [19]. Morphological changes are often accompanied by alterations in mechanical and optical properties. Therefore heat-treatment-induced morphological changes have been used to modify optical and mechanical material properties for integrated optics such as fiber Bragg gratings[20, 21] and polymer-based solar cells, for instance [22, 23]. Thus, the thermal stability of polymers is an important aspect to consider when designing an optical component to ensure its performance. However, while thermally induced changes in the mechanical properties of various polymers including PMMA, polycarbonate, and polystyrene, are well investigated, information on thermal effects in the THz optical properties is still scarce [24, 19, 25].

In this paper, we sought to investigate THz optical response of bulk polymethacrylates subjected to annealing processes. A common polymethacrylate that is compatible with a stereolithographic fabrication has been selected for this investigation. THz spectroscopic ellipsometry was performed before and after the annealing processes. The polymethacrylate studied here was found to maintain its ellipsometric response in the THz spectral range after annealing at moderate temperature of up to 70 °C. Experimental and best-model calculated THz $\cos(2\Psi)$ and $\sin(2\Psi)\cos(\Delta)$ spectra are presented. A parameterized model dielectric function composed of oscillators with Gaussian broadening was used for the data analysis and is discussed here.

2.2.2 Experiment

2.2.2.1 Sample Preparation

The samples studied here were prepared using UV-induced polymerization of the "black" resin available from Formlabs Inc. For each sample, approximately 2 ml of resin was applied in between two microscope slides positioned parallel to each other on a glass plate. Subsequently, a second glass plate was set on top of the spacers to shape the resin into a thin slab. The assembly was then placed in a UV oven (UVO cleaner model no. 42, Jelight Company Inc.) and was cured for 15 minutes until the resin was fully polymerized. As a result, the finished sample has parallel interfaces with low surface roughness and is suitable for accurate ellipsometric measurements in the THz spectral range. The expected interference oscillations in the THz spectral range due to the plain parallel interfaces will aid in the detection of small changes in the dielectric function, which is a well known interference enhancement approach and frequently used in the visible spectral range [26]. The same procedure was applied to create a total of three identical samples. Once UV polymerized, two samples were thermally annealed in a precision oven at 70 °C for two different lengths of time, 2 and 4 hours, respectively. For comparison, one sample was not thermally annealed and investigated as a reference.

2.2.2.2 Data Acquisition and Analysis

The thermally annealed polymethacrylate samples were investigated using a custom-built THz spectroscopic ellipsometer system, which is described in detail in Ref. [27]. The ellipsometer employs a rotating analyzer configuration (polarizer − sample − rotating analyzer). The instrument is equipped with a backward-wave oscillator source operating in a spectral range from 97 to 179 GHz, which can be extended up to 1010 GHz using GaAs Schottky diode frequency multipliers. A Golay cell was used as a detector. The instrument was calibrated using a regression calibration method as detailed in Ref. [28]. Further details on the noise performance are provided in Ref. [27]. Ellipsometric $\cos(2\Psi)$ and $\sin(2\Psi)\cos(\Delta)$ spectra were obtained over range from 650 to 950 GHz with a resolution of 5 GHz at two incidence angles: $\Phi_a = 70^\circ$ and 75°.

The un-annealed reference sample was investigated over a wider spectral range using a commercial infrared ellipsometer (Mark I IR-VASE, J.A. Woollam Company Inc.) and a commercial THz ellipsometer (THz-VASE, J.A. Woollam Company Inc.). The IR ellipsometer operates in a polarizer − sample − rotating compensator − analyzer configuration, while the THz ellipsometer uses a rotating polarizer − sample − rotating compensator − analyzer configuration as detailed in Ref. [15].

Ellipsometric $\cos(2\Psi)$ and $\sin(2\Psi)\cos(\Delta)$ spectra were obtained in the infrared spectral range from 300 to 4000 cm^{-1} (9 to 120 THz) with a resolution of 4 cm^{-1} (0.1 THz) at three angles of incidence: $\Phi_a = 65^\circ$, 70°, and 75°. The THz ellipsometric data were obtained over the range from 22 to 32 cm^{-1} (0.65 to 0.95 THz) with a resolution of 0.2 cm^{-1} (5 GHz) at the same angles of incidence as for the infrared data. The optical modeling and data analysis were performed using a commercial ellipsometry data analysis software package (WVASE32$^{\text{TM}}$, J.A. Woollam Company). The ellipsometric data sets are analyzed using stratified-layer optical model calculations which consist of three layers, ambient/polymethacrylate/ambient [29].

The ellipsometric data obtained for the reference sample was used to develop a model dielectric function for the polymethacrylate, which is composed of a sum of oscillators with Gaussian broadening:

$$\varepsilon(\omega) = \varepsilon_1(\omega) + i\varepsilon_2(\omega) = \varepsilon_\infty + \sum_i \varepsilon_{Gau}(A, \Gamma, \omega, \omega_o), \tag{2.3}$$

where the function $\varepsilon_{\text{Gau}}(A, \Gamma, \omega, \omega_o)$ indicates an oscillator with Gaussian broadening. The oscillator amplitude, broadening, and resonance frequency are designated by A, Γ, ω_o, respectively. The oscillators are given analytically by their Gaussian form for the imaginary part $\varepsilon_2^{\mathrm{Gau}}(\omega)$ of the complex dielectric function $\varepsilon(\omega)$:

$$\varepsilon_2^{\mathrm{Gau}}(\omega) = Ae^{\left(-\left(\frac{\omega-\omega_o}{f\cdot\Gamma}\right)^2\right)} + Ae^{\left(-\left(\frac{\omega+\omega_o}{f\cdot\Gamma}\right)^2\right)}, \tag{2.4}$$

where $1/f = 2\sqrt{\ln(2)}$. The corresponding values for $\varepsilon_1^{\mathrm{Gau}}(\omega)$ are determined by Kramers-Kronig integration of Eq. (2.4) during the Levenberg-Marquardt-based line shape analysis of the experimental spectra.

2.2.3 Results and discussion

Figure 2.5 and 2.6 illustrate the experimental (dashed green lines) and the best-model calculated (solid red lines) $\cos(2\Psi)$ and $\sin(2\Psi)\cos(\Delta)$ spectra of the un-annealed polymethacrylate reference sample, respectively, at two angles of incidence $\Phi_a = 65°$ and $75°$ for the spectral range from 0.65 to 0.95 THz, and from 9 to 120 THz.

Note that experimental $\cos(2\Psi)$ and $\sin(2\Psi)\cos(\Delta)$ spectra were obtained for $\Phi_a = 65°, 70°$, and $75°$ and analyzed simultaneously, however, for clarity, the data for $\Phi_a = 70°$ is omitted here. The experimental and best-model calculated data are in very

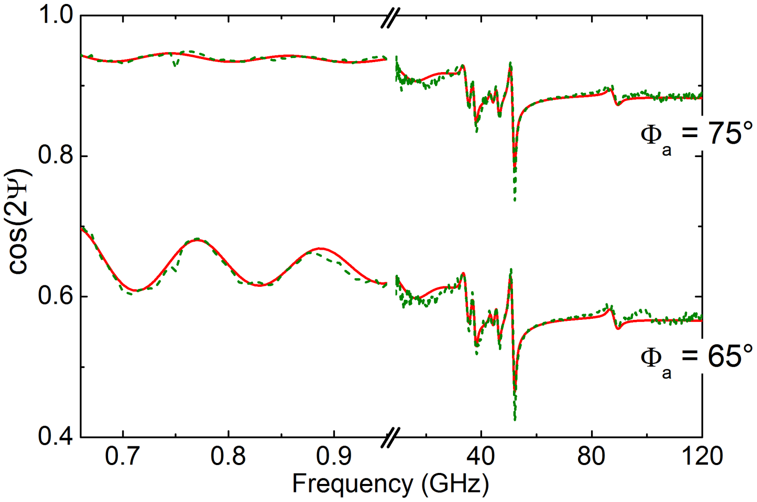

Figure 2.5: Best-model calculated (solid red lines) and experimental (dashed green lines) $\cos(2\Psi)$ spectra obtained at $\Phi_a = 65°$ and $75°$ for the un-annealed reference sample. The infrared range is dominated by a number of distinct absorption bands while the THz range shows Fabry-Pérot oscillations as a result of the plane parallel interfaces of the sample.

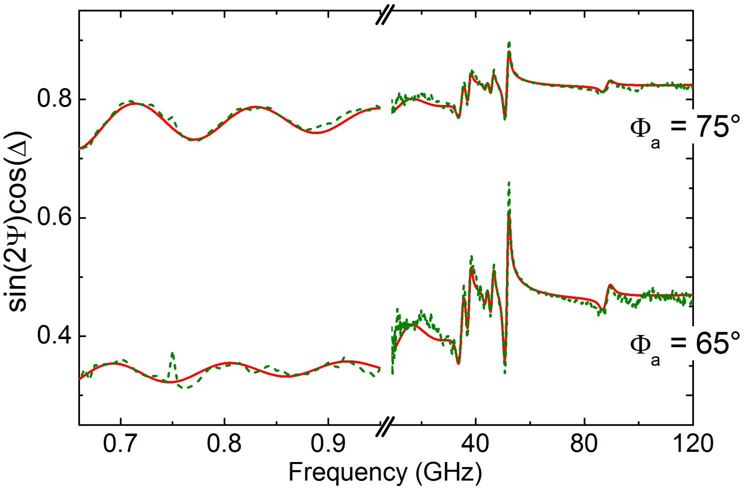

Figure 2.6: As Fig. 2.5, but for the best-model calculated (solid red lines) and experimental (dashed green lines) $\sin(2\Psi)\cos(\Delta)$ spectra obtained at $\Phi_a = 65°$ and 75° for the un-annealed reference sample.

good agreement for the non-annealed reference sample. Fabry-Pérot oscillations are observed in the range from 0.65 to 0.95 THz, indicating that the sample is transparent in this spectral window. The IR range (9 to 120 THz), on the other hand, is dominated by a number of distinct absorption features with Gaussian broadening profile. Further details on the best-model parameters are provided in Tabs. 1 and 2 in Ref. [18].

Figures 2.8 and 2.9 show the experimental and best-model calculated $\cos(2\Psi)$ and $\sin(2\Psi)\cos(\Delta)$ spectra obtained for the samples annealed for 2 and 4 hours, respectively. Similar to the ellipsometric data of the reference sample shown in Figs. 2.5 and 2.6, the $\cos(2\Psi)$ and $\sin(2\Psi)\cos(\Delta)$ spectra of the annealed samples are dominated by Fabry-Pérot oscillations in spectral range from 650 to 950 GHz. The experimental data obtained for both annealed samples were analyzed using the model dielectric function established for the reference sample without further varying the best-model oscillator parameters. In order to obtain a good agreement between experimental and model-calculated data, only the parameters for the sample thickness were varied. The best-model thicknesses for 2 hours and 4 hours annealed samples were 1080 µm ± 1 µm and 1086 µm ± 1 µm, respectively. These thickness values are in an excel-

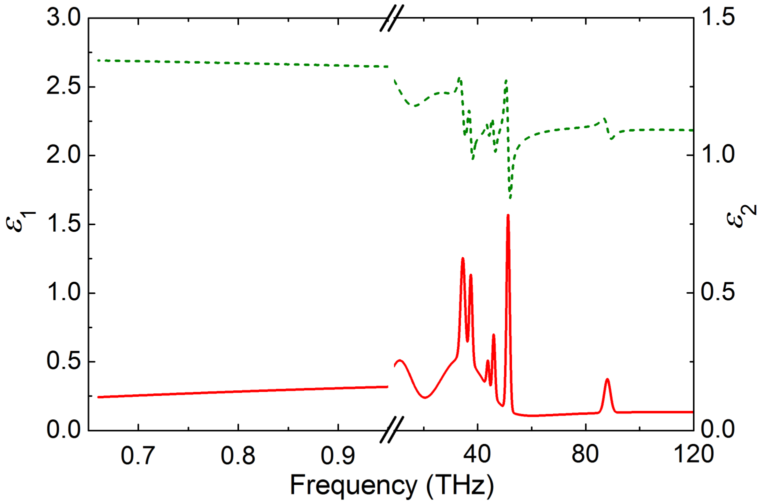

Figure 2.7: Best-model calculated real (dashed green line) and imaginary part (solid red line) of the complex dielectric function $\varepsilon(\omega)$ for the data shown in Figs. 2.5 and 2.6 is depicted. The major absorption features occur in the range from 9 to 120 THz. Below 9 THz only a broad and shallow absorption can be observed. The best-model parameters are omitted here and the interested reader is referred to Ref. [18].

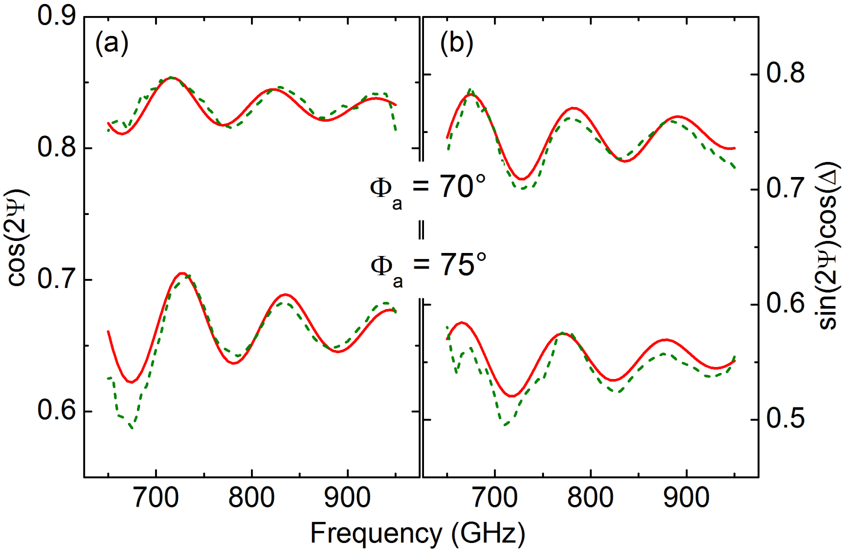

Figure 2.8: (a) Experimental (green dotted lines) and best-model calculated (red solid lines) cos(2Ψ) spectra of the polymethacrylate sample which was annealed for 2 hours obtained at $\Phi_a = 70°$ and 75°. Fig. 2.8 (b) Same as (a) but for the $\sin(2\Psi)\cos(\Delta)$ spectra.

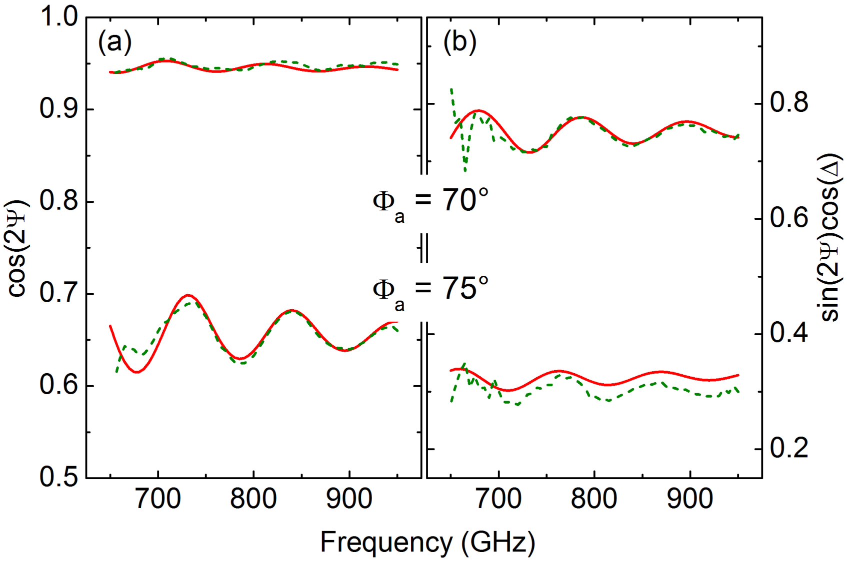

Figure 2.9: (a) Experimental (green dotted lines) and best-model calculated (red solid lines) cos(2Ψ) spectra of the polymethacrylate sample which was annealed for 4 hours obtained at $\Phi_a = 70°$ and 75°. Fig. 2.9 (b) Same as (a) but for the $\sin(2\Psi)\cos(\Delta)$ spectra.

lent agreement with the nominal thickness of the samples, which is 1000 µm. This suggests that annealing for up to 4 hours at a temperature of 70 °C does not lead to any measurable changes in the THz dielectric function. A slight reduction of the interference amplitude at higher THz frequencies can be noticed in Figs. 2.8 and 2.9. We have attributed this reduction to a broad and shallow absorption located outside of the accessible spectral range of the THz ellipsometer at approximately 1.2 THz. For further details regarding this broad absorption, the interested reader is referred to Ref. [18].

2.2.4 Summary and conclusion

A common polymethacrylate compatible with a commercial stereolithography system was investigated before and after thermal annealing by spectroscopic THz ellipsometry. A model dielectric function consisting of Gaussian oscillators was established using THz and infrared ellipsometric data obtained from an un-annealed sample. This model dielectric function was also found to accurately render the experimental $\cos(2\Psi)$ and $\sin(2\Psi)\cos(\Delta)$ spectra from thermally annealed samples in THz spectral range. In conclusion, the investigated polymethacrylate was found to maintain a stable optical response in THz spectral range after thermal annealing at temperatures up to 70 °C.

REFERENCES

[1] A. D. Squires, E. Constable, and R. A. Lewis, "3d printed terahertz diffraction gratings and lenses," *J. Infrared Millim. Terahertz Waves* **36**, 72 (2015).

[2] M. Weidenbach, D. Jahn, A. Rehn, S. F. Busch, F. Beltrán-Mejía, J. C. Balzer, and M. Koch, "3d printed dielectric rectangular waveguides, splitters and couplers for 120 ghz," *Opt. Express* **24**, 28968 (2016).

[3] A. Kaur, J. C. Myers, M. I. M. Ghazali, J. Byford, and P. Chahal, "Affordable terahertz components using 3d printing," *2015 IEEE 65th Electronic Components and Technology Conference (ECTC)*, 2071 (2015).

[4] S. F. Busch, M. Weidenbach, M. Fey, F. Schfer, T. Probst, and M. Koch, "Optical properties of 3d printable plastics in the thz regime and their application for 3d printed thz optics," *J. Infrared Millim. Terahertz Waves* **35**, 993 (2014).

[5] S. F. Busch, M. Weidenbach, J. C. Balzer, and M. Koch, "Thz optics 3d printed with topas," *J. Infrared Millim. Terahertz Waves* **37**, 303 (2016).

[6] W. D. Furlan, V. Ferrando, J. A. Monsoriu, P. Zagrajek, E. Czerwińska, and M. Szustakowski, "3d printed diffractive terahertz lenses," *Opt. Lett.* **41**, 1748 (2016).

[7] K. Y. Park, N. Wiwatcharagoses, and P. Chahal, "Wafer-level integration of micro-lens for thz focal plane array application," *2013 IEEE 63rd Electronic Components and Technology Conference*, 1912 (2013).

[8] X. Yan and P. Gu, "A review of rapid prototyping technologies and systems," *Comput. Aided Des.* **28**, 307 (1996).

[9] T. C. Okwuosa, B. C. Pereira, B. Arafat, M. Cieszynska, A. Isreb, and M. A. Alhnan, "Fabricating a shell-core delayed release tablet using dual fdm 3d printing for patient-centred therapy," *Pharm. Res.* **34**, 427 (2017).

[10] B. Zhang, Y. Guo, H. Zirath, and Y. P. Zhang, "Investigation on 3-d-printing technologies for millimeter- wave and terahertz applications," *Proc. IEEE* **105**, 723 (2017).

[11] T. D. Ngo, A. Kashani, G. Imbalzano, K. T. Q. Nguyen, and D. Hui, "Additive manufacturing (3d printing): A review of materials, methods, applications and challenges," *Compos. B. Eng* **143**, 172 (2018).

[12] A. I. Shallan, P. Smejkal, M. Corban, R. M. Guijt, and M. C. Breadmore, "Cost-effective three-dimensional printing of visibly transparent microchips within minutes," *Anal. Chem.* **18**, 3124 (2014).

[13] W. J. Otter and S. Lucyszyn, "Hybrid 3-d-printing technology for tunable thz applications," *Proc. IEEE* **105**, 756 (2017).

[14] D. B. Fullager, S. Park, C. Hovis, Y. Li, J. Reese, E. Sharma, S. Lee, C. Evans, G. D. Boreman, and T. Hofmann, "Metalized poly-methacrylate off-axis parabolic mirrors for terahertz imaging fabricated by additive manufacturing," *J. Infrared Millim. Terahertz Waves* **40**, 269 (2019).

[15] H. Fujiwara, Spectroscopic Ellipsometry: Principles and Applications, (John Wiley & Sons2007).

[16] D. B. Fullager, G. D. Boreman, and T. Hofmann, "Infrared dielectric response

of nanoscribe ip-dip and ip-l monomers after polymerization from 250 cm^{-1} to 6000 cm^{-1}," *Opt. Mater. Express* **7**, 888 (2017).

[17] J. A. Colla, R. E. M. Vickers, M. Nancarrow, and R. A. Lewis, "3d printing metallised plastics as terahertz reflectors," *J. Infrared Millim. Terahertz Waves* **40**, 752 (2019).

[18] S. Park, Y. Li, D. B. Fullager, S. Schöche, C. M. Herzinger, G. D. Boreman, and T. Hofmann, "Terahertz to mid-infrared dielectric properties of polymethacrylates for stereolithographic single layer assembly," *J. Infrared Millim. Terahertz Waves* **40**, 971 (2019).

[19] E. W. Fischer, "Effect of annealing and temperature on the morphological structure of polymers," *Pure Appl. Chem.* **31**, 113 (1972).

[20] W. Yuan, A. Stefani, M. Bache, T. Jacobsen, B. Rose, N. Herholdt-Rasmussen, F. K. Nielson, S. Andersen, O. B. Sorensen, K. S. Hansen, and O. Bang, "Improved thermal and strain performance of annealed polymer optical fiber bragg gratings," *Opt. Commun.* **284**, 176 (2011).

[21] G. Woyessa, K. Nielsen, A. Stefani, C. Markos, and O. Bang, "Temperature insensitive hysteresis free highly sensitive polymer optical fiber bragg grating humidity sensor," *Opt. Express* **24**, 1206 (2016).

[22] T. Erb, U. Zhokhavets, G. Gobsch, S. Raleva, B. Stühn, P. Schilinsky, C. Waldauf, and C. J. Brabec, "Correlation between structural and optical properties of composite polymer/fullerene films for organic solar cells," *Adv. Funct. Mater.* **15**, 1193 (2005).

[23] G. Li, Y. Yao, H. Yang, V. Shrotriya, G. Yang, and Y. Yang, "Solvent annealing effect in polymer solar cells based on poly(3-hexyltheopene) and methanofullerenes," *Adv. Funct. Mater.* **17**, 1636 (2007).

[24] T. Brady and G. Yeh, "Yielding behavior of glassy amorphous polymers," *J. Appl. Phys.* **42**, 4622 (1971).

[25] Y. Fu and J. R. Lackowicz, "Spectroscopy: A closer look at polymer annealing," *Nature* **472**, 178 (2011).

[26] J. N. Hilfiker, N. Singh, T. Tiwald, D. Convey, S. M. Smith, J. H. Baker, and H. G. Tompkins, "Survey of methods to characterize thin absorbing films with spectroscopic ellipsometry," *Thin Solid Films* **516**, 7979 (2008).

[27] P. Kühne, N. Armakavicius, V. Stanishev, C. M. Herzinger, M. Schubert, and V. Darakchieva, "Advanced terahertz frequency -domain ellipsometry instrumentation for in situ and ex situ applications," *IEEE Trans. Terahertz Sci. Technol.* **8**, 257 (2018).

[28] B. Johs, "Regression calibration method for rotating element ellipsometers," *Thin Solid Films* **234**, 395 (1993).

[29] G. E. Jellison, Handbook of ellipsometry, (William Andrew, 2005).

CHAPTER 3: THZ ONE-DIMENSIONAL PHOTONIC CRYSTALS AND DEFECT MODES

3.1 One-dimensional Photonic Crystals Fabricated Using Stereolithographic Single Layer Assembly for the Terahertz Spectral Range

A polymer-based one-dimensional photonic crystal with a photonic bandgap in terahertz frequency range was designed and fabricated through stereolithography and was characterized using THz spectroscopy.[1] The photonic crystal studied here consists of alternating compact and low-density layers. The compact layers were fabricated from fully polymerized polymethacrylate without any intentional internal structure. The low-density layers consist of sub-wavelength sized columns, where the volume density was selected to provide sufficient contrast between the dielectric functions of adjacent layers. The photonic crystal samples were fabricated in a single step using a commercial stereolithography system and polymethacrylate compatible with the system. Transmission spectroscopy in a range from 82 to 125 GHz was used to determine the THz spectral response of the sample. The transmission data were analyzed using stratified optical layer model calculations. A distinct photonic bandgap with a center frequency of 111 GHz was observed in the experimental transmission spectra. Bruggeman effective medium approximation was found to accurately describe the dielectric function of the low-density layers. An excellent agreement between the relevant model parameters and the corresponding design parameters was found, indicating the versatility of the approach for the fabrication of photonic crystals for the

---

[1] Reprinted by permission from Springer Nature Customer Service Centre GmbH: Springer S. Park, Y. Li, B. Norton, M. McLamb, G. D. Boreman, and T. Hofmann, “One-dimensional Photonic Crystals Fabricated Using Stereolithographic Single Layer Assembly for the Terahertz Spectral Range,” *J. Infrared, Millimeter, Terahertz Waves* **41**, 542 - 551 (2020). © 2020

THz spectral range.

3.1.1 Introduction

The development of optical systems for THz frequencies requires improvements in the manufacturing and prototyping of optical components designed for this spectral range. In recent years, additive manufacturing has been introduced as an effective approach for rapid prototyping of THz optical elements such as lenses [1], filters [2], waveguides and diffractive components [3, 4], for instance. So far, the prevalent additive manufacturing technique used for the fabrication of THz optical components is fused filament deposition [5]. The main advantage of fused filament deposition is its compatibility to a wide range of materials suitable for THz optical applications. In addition, the instrument and fabrication costs are lower compared to other additive manufacturing techniques [6]. However, fused filament deposition suffers from a low spatial resolution and a comparatively poor surface finish [7, 8]. The spatial resolution is primarily limited by the nozzle diameter through which material filaments are heated and fused. Commonly achieved resolutions are on the order of several hundreds of µm [9].

Stereolithography, in contrast, has been demonstrated to achieve spatial resolutions on the order of 10 µm and substantially smaller surface roughness compared to other additive manufacturing techniques [6, 10]. Recently, reflective optical components have been successfully fabricated for the THz spectral range by metalizing polymer-based, stereolithographically fabricated reflectors [11, 12]. The THz optical responses achieved with these reflective surfaces are comparable with commercially available optics and surface roughness of approximately 5 µm was obtained [12]. In addition to reflective components, broad-band absorber structures have been realized using different additive manufacturing approaches [13, 14]. Similar to the complex geometries required to achieve broad-band absorption behavior of materials in the THz spectral range, periodic structures that exhibit bands with very high reflectivity can be realized using dielectric materials [15]. Such so-called photonic crystals are composed of spatially periodic arrangements of sub-wavelength scale constituents [16]. As a result, these materials affect the propagation of electromagnetic waves and photonic bandgaps are formed similar to electronic bandgaps in solid state materials [17]. Consequently, the characteristics of the photonic bandgap depend on the unit cell of the photonic crystal. Its spectral position and width can therefore be easily tuned by adjusting the geometry of the photonic crystal [18].

Many publications have demonstrated one-dimensional (1D) photonic crystals designed for the THz spectral range [19, 20, 21]. Several groups have investigated polymer-based 1D photonic crystals using various fabrication methods including stacking of polymeric films [22], and combination of drop-casting and film extrusion [23]. However, polymer-based 1D photonic crystals fabricated using stereolithography have not been reported yet. Here we demonstrate the stereolithographic fabrication of 1D photonic crystals with a photonic bandgap in the THz spectral range. A polymethacrylate, which is semitransparent in the THz spectral range, is used here for the first time for this application. This approach holds the promise of a simplified fabrication of THz photonic crystals for which otherwise requires complex ceramic-epoxy-based processes [24].

3.1.2 Experiment

3.1.2.1 Design and fabrication

The 1D photonic crystals investigated here are composed of alternating compact and low-density layers with plane parallel interfaces fabricated from a single type of polymethacrylate as shown in Figs. 3.1 and 3.2. The low-density layers are composed of columns with a square base. The columns are oriented normal to the interface between adjacent layers and are arranged in a square lattice pattern as shown in the inset of Fig. 3.1, where one unit cell is depicted with its dimensions. The compact layers are fabricated from fully polymerized polymethacrylate, without any intentional internal structure.

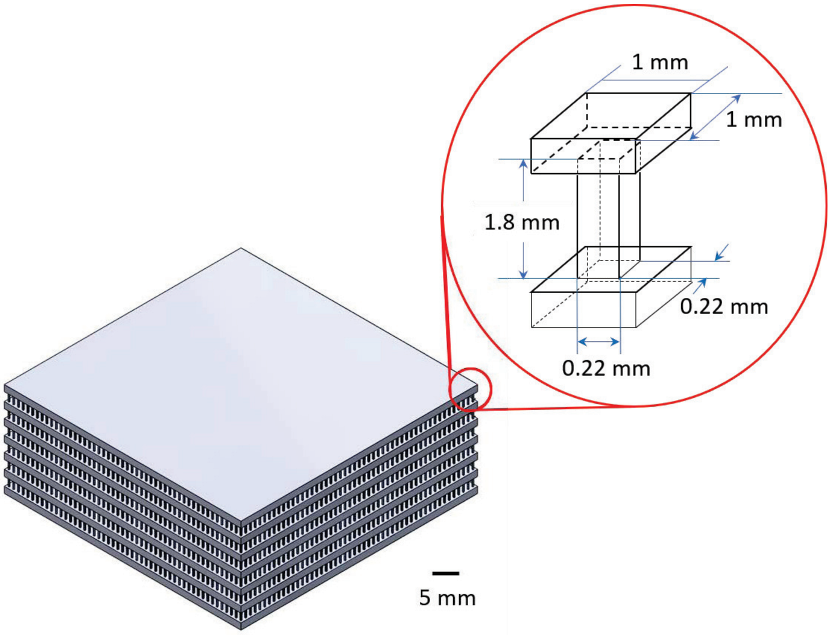

Figure 3.1: CAD model of the 1D photonic crystal investigated here. The low-density layers are composed of vertical columns with a square base that are arranged in a square lattice pattern. The dimensions of the unit cell of the low-density layer are displayed in the inset.

By adjusting the volume density of the columns of the low-density layers, the effective dielectric function $\varepsilon_{\mathrm{low}}^{\mathrm{eff}}$ of these layers can be tailored over a wide range. The geometry of the photonic crystal investigated here was optimized to form a photonic bandgap with a center frequency of 112 GHz as described further below. Optical model calculations further revealed that this design approach could be scaled for center frequencies of up to 500 GHz with the resin employed here (black v3, Formlabs Inc.). The fabrication of 1D photonic crystals with band gaps higher than 500 GHz is currently limited due to a broad and shallow absorption present in the employed polymethacrylate. This absorption feature is centered at approximately 1.2 THz and has been identified for a number of resins, which are commonly used for commercial, polymethacrylate-based stereolithography systems [25].

Stratified layer optical model calculations were applied here to optimize the geometry of the 1D photonic crystal for the desired photonic bandgap frequency of 112 GHz. The frequency was selected for compatibility with the spectroscopic equipment employed for the experimental inspection of the fabricated crystal. Stratified layer optical model calculations allow a fast and accurate evaluation of transmission and reflection spectra for 1D photonic crystals. This approach is an effective alternative to time consuming finite element-based simulations, which are often required for the numerical evaluation of photonic crystal structures [26]. Here, a commercial software package (WVASE32$^{\mathrm{TM}}$, J.A. Woollam Company) was used for the stratified optical model calculations shown here. The employed optical model consists of 6 alternating pairs of compact and low-density layers with an extra compact layer in an air ambient.

The dielectric function of the low-density layers $\varepsilon_{\mathrm{low}}^{\mathrm{eff}}$ is described using the Bruggeman effective medium approximation. This homogenization approach allows an accurate description of the THz optical response of the low-density layers. The resultant complex dielectric function depends on the volumetric fraction of the columnar polymethacrylate inclusions f_{i} and their dielectric function ε_{i} [27]:

$$\begin{aligned}\varepsilon_{\mathrm{low}}^{\mathrm{eff}}(f_{\mathrm{i}}) &= \frac{1}{4}\Big\{(3f_{\mathrm{i}}-1)\varepsilon_{\mathrm{i}}+(2-3f_{\mathrm{i}})\varepsilon_{\mathrm{h}} \pm \\ &\quad \sqrt{[(3f_{\mathrm{i}}-1)\varepsilon_{\mathrm{i}}+(2-3f_{\mathrm{i}})\varepsilon_{\mathrm{h}}]^2+8\varepsilon_{\mathrm{i}}\varepsilon_{\mathrm{h}}}\Big\}.\end{aligned} \tag{3.1}$$

The complex dielectric functions of the inclusions (black v3, Formlabs Inc.) and the host (air) are denoted by ε_{i} and ε_{h}, respectively.

The dielectric function of the compact layers is denoted by $\varepsilon_{\mathrm{com}}$. The dielectric functions $\varepsilon_{\mathrm{com}}$ and ε_{i} are assumed to be identical during the data analysis and were determined previously through spectroscopic ellipsometry in the infrared and THz spectral range using a UV polymerized resin sample (black v3, Formlabs Inc.) as reported in reference [25].

In order obtain a 1D photonic crystal with a bandgap centered at approximately 112 GHz, the thickness of the low-density layers, the thickness of the compact layers, and the volumetric fraction of the columnar structures comprising the low-density layers were varied within the parameter window limited by the voxel size of the stereolithographic system employed here.

As a result of these model calculations, the nominal geometry of the photonic crystal was obtained (see Fig. 3.1). The thickness of the compact layers was selected to be 1300 µm and the thickness of the low-density layers was determined to be 1800 µm. The volume density of the columnar inclusions f_{i} was selected to be 0.05. A crystal composed of 6 alternating pairs with an extra compact layer was selected and the transmission spectrum calculated using this nominal geometry is shown in Fig. 3.3 (a). The minimum transmittance achieved at the center frequency of $f \approx 112$ GHz is approximately 0.005.

Photonic crystals with the desired dimensions were designed using a commercial 3D CAD software (SolidWorks, Dassault Systèmes). The dimensions of the unit cell are shown in the inset of Fig. 3.1 and determine f_i of the low-density layer and thereby its dielectric function. The fabricated photonic crystal has a surface area of 5×5 cm^2. The photonic crystal was synthesized in a single stereolithographic fabrication step using a commercially available stereolithography system (Form2, Formlabs. Inc.) with a resin compatible with the system (black v3, Formlabs. Inc.). The employed stereolithography system uses an inverted bottom-to-top fabrication approach and utilizes a UV laser with wavelength of 405 nm to photopolymerize the resin layer by layer, forming complex three-dimensional objects [28]. The inverted bottom-to-top fabrication requires support structures to underpin the sample components during the fabrication process. This allows an arbitrary orientation of the sample with respect to the polymerization plane [28]. Here, the photonic crystal samples were oriented at 45° to effectively prevent any unpolymerized resin from accumulating within the low-density layers during the fabrication process.

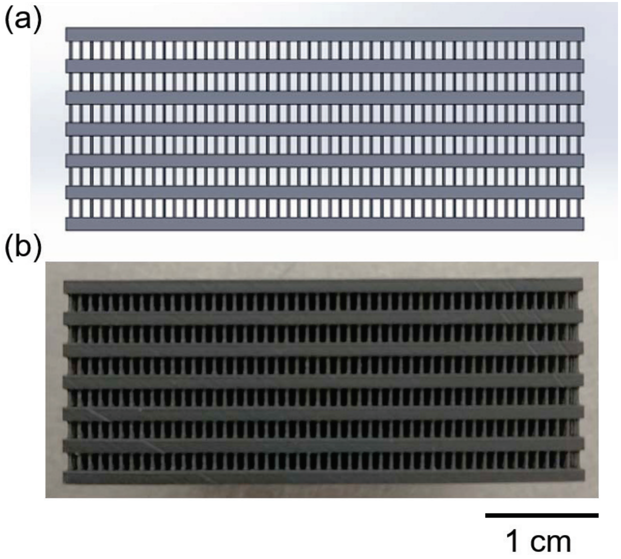

Figure 3.2: A side view of (a) the CAD model of the investigated 1D photonic crystal showing six pairs of compact and low-density layers. (b) Photographic image of the side view of the stereolithographically fabricated 1D photonic crystal. Upon visual inspection, the fabricated sample appears to be close to true-to-form as compared to the CAD design. Small deviations from the as-designed dimensions are revealed during the analysis of the THz transmission spectra shown in Fig. 3.3.

After the polymerization, the sample was immersed in isopropanol for 15 min and subsequently rinsed thoroughly for an additional 10 min to remove all excess unpolymerized resin. After the rinsing process, the sample was placed in a precision oven at 60 °C for 5 min in order to evaporate any excess isopropanol. After the heating process, the sample was cured in a UV oven for 20 min to ensure complete polymerization.

Figure 3.2 shows a side view of the CAD model (a) and a photographic image of the fabricated photonic crystal sample (b) for comparison. Upon visual inspection a very good agreement between the CAD design and the fabricated photonic crystal can be observed, indicating that both polymerization and post-process curing result in a near true-to-form sample structure. It can further be noted that the unpolymerized resin appears to have been completely removed between the columnar structures of the low-density layers. A complete removal of the unpolymerized resin is crucial for the THz response of the photonic crystal. Any remaining unpolymerized resin would alter the volumetric fraction of the inclusions f_i of the low-density layers, which would lead to a change in the dielectric function $\varepsilon_{\mathrm{low}}^{\mathrm{eff}}(f_{\mathrm{i}})$ of the low-density layers and thus alter the position and width of the photonic bandgap.

3.1.2.2 Data Acquisition and Analysis

Normal incidence THz transmission measurements were carried out for the fabricated photonic crystals over the spectral range from 82 to 125 GHz with a 0.1 GHz spectral resolution. An electronic synthesizer (Synthesizer, Virginia Diodes Inc.) in combination with an extension module (Virginia Diodes Inc.) served as a source. A 60 mm focal length lens was used to collimate the radiation emitted by the extension module prior to interacting with the sample. The radiation transmitted through the sample was then focused using a second 60 mm focal length lens, and detected with a broadband power meter (PM3, Erickson Instruments).

The experimental transmission data was analyzed through stratified layer model calculations using a commercial software package (WVASE32$^{\mathrm{TM}}$, J.A. Woollam Company). During the analysis, the thickness of the low-density layers and the thickness of the compact layers were varied using a Levenberg-Marquardt-based algorithm until the best-match between model-calculated and experimental data was obtained. Note that the thicknesses of the layers were not varied independently. Instead, it was assumed that the layer thicknesses of all compact layers are identical. Correspondingly, the thicknesses of all low-density layers were assumed to be the same and varied collectively. The dielectric function of the compact layers $\varepsilon_{\mathrm{com}}$ was obtained using THz and infrared spectroscopic ellipsometry as reported in Ref. [25]. The dielectric function of the low-density layers $\varepsilon_{\mathrm{low}}^{\mathrm{eff}}$ was adjusted by varying the volume fraction of the columnar inclusions f_i as described in Eqn. (3.1). Similar to the layer thicknesses, it was assumed that f_i is identical for all low-density layers and laterally homogeneous across the extension of the layers.

3.1.3 Results and discussion

Figure 3.3 (a) depicts the calculated normal incidence transmission spectrum for the nominal geometry in the spectral range from 82 to 125 GHz. A distinct photonic

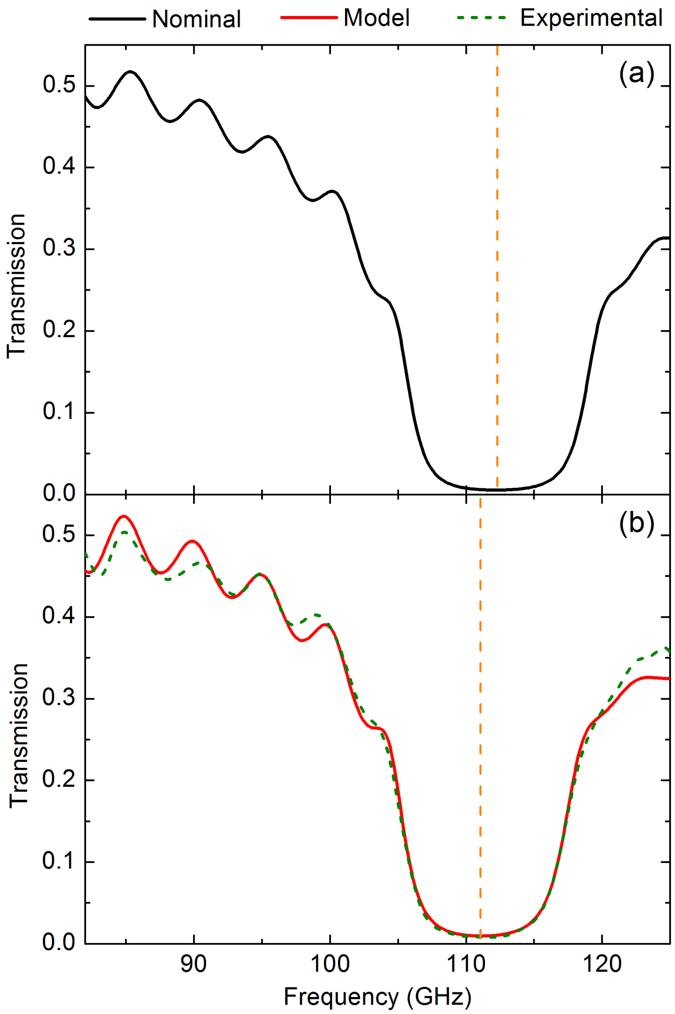

Figure 3.3: (a) Calculated normal incidence transmission spectrum from the nominal geometry (black solid line). (b) Experimental (green dashed line) and best-fit model calculated (red solid line) THz transmission spectrum of a stereolithographically fabricated 1D photonic crystal measured at normal incidence. All data sets show a distinct photonic bandgap with over 99% reduction in transmission over the band. While the photonic bandgap obtained for the nominal geometry is centered at 112 GHz, the experimental and best-model calculated data appear to be slightly red-shifted with a center frequency of approximately 111 GHz.

bandgap centered at 112 GHz can be clearly observed. At 112 GHz the calculated transmission drops to 0.005. The experimental (dashed green line) and best-model calculated (solid red line) normal incidence transmission spectra obtained for the stereolithographically fabricated photonic crystal are shown in Fig. 3.3 (b).

The experimental and best-model calculated spectra are in good agreement over the entire spectral range. Both the photonic bandgap, which is observed at 111 GHz, as well as the side lobes are well reproduced in the best-model calculated spectrum. At the center of the bandgap the transmitted signal is reduced by 99%. The bandgap observed for the fabricated photonic crystal is red-shifted by approximately 1 GHz compared to the photonic crystal with nominal geometry. The best-model parameters obtained during the data analysis were 1350 ± 2 µm, 1743 ± 3 µm and 0.062 ± 0.001 for the layer thickness of the compact and the low-density layers, and the volumetric fraction of the columnar inclusions f_i of the low-density layers, respectively. Both the geometrical parameters and the volumetric fraction of the columns f_i deviate slightly from the nominal parameters selected during the design in order to obtain a photonic bandgap at 112 GHz. This deviation is likely due to the limited spatial resolution of the commercial stereolithography system.

Model calculations reveal, that the red-shift of the center frequency of the photonic bandgap is primarily due to the slight deviations of the layer thicknesses from their nominal values. The best-model parameter $f_i = 0.062 \pm 0.001$ also differs from the as-designed value of 0.05. It is tentatively assumed here that this discrepancy is due to the selection of a rectangular base unit cell for the columnar structures of the low-density layers, which is likely to suffer from losses in fidelity at the edges. Using a rectangular base for the columnar inclusions results in drastically reduced CAD file sizes compared to circular base geometries and thus in reduced fabrication times. The overall attenuation observed in transmission spectrum outside of the bandgap is attributed to the broad absorption in this spectral range inherent to the polymethacrylate used for fabrication, as described in Ref. [25]. Based on our model calculations and previous experiments with stereolithographically fabricated reflective optics, we estimate the surface roughness to be insignificant and the thickness non-uniformity to be below 3% for all layers [12]. Implementing a thickness non-uniformity of up to 3% in our model calculations did not result in significant changes in the lineshape of the model-calculated transmission spectra. Thus, thickness non-uniformity and interface roughness are not considered for the best-fit model calculated data shown in Fig. 3.3. It can further be noticed that the data sets obtained for the nominal geometry and the fabricated sample exhibit distinct side-lobes at frequencies below the photonic bandgap. The occurrence of side-lobes with amplitudes similar to those observed for the photonic crystal with nominal geometry is indicative of negligible layer non-uniformity [26].

3.1.4 Summary and conclusion

In this work, we report on the demonstration of polymethacrylate based 1D photonic crystals fabricated using stereolithography. The investigated 1D photonic crystals consist of 6 alternating pairs of compact polymethacrylate layers and low-density layers with an extra compact layer. While the compact layers are fabricated from fully polymerized polymethacrylate without any intentional internal structure, the low-density layers are composed of arrays of sub-wavelength sized polymethacrylate columns oriented perpendicular to the layer interfaces.

The photonic crystal was synthesized in a single stereolithographic fabrication step. The THz optical response of the fabricated crystal was experimentally evaluated using transmission spectroscopy in the spectral range from 82 to 125 GHz at normal incidence. The experimental transmission spectra exhibit the signature of a photonic bandgap with a center frequency of 111 GHz, which is found to be red-shifted by 1 GHz from the bandgap predicted for a 1D photonic crystal with the nominal geometry.

The THz transmission data were analyzed using optical model calculations. A good agreement was found between the experimental and best-model THz transmission data. During the analysis the dielectric function of the compact layers was assumed to be identical to that of bulk polymethacrylate, while the dielectric function of the low-density layers was well described using a Bruggeman effective medium approach. The analysis revealed slight deviations of the fabricated from the nominal geometry. These deviations are the cause of the observed red-shift and are likely due to the limited spatial resolution of the stereolithography system employed here.

Model calculations predicted that polymethacrylate-based stereolithography system employed here can be used to fabricate 1D photonic crystals with bandgap center frequencies of up to approximately 500 GHz. Our findings further indicate that the upper limit of the bandgap frequency for the 1D photonic crystal design discussed here is currently not limited by the spatial resolution of commonly available stereolithography systems, but rather hindered by a broad absorption which is observed for a number of commercially available polymethacrylate based resins as shown in reference [25].

3.2 Highly Localized Defect Mode in Polymer-based THz Photonic Crystals Fabricated Using Stereolithography

A polymer-based one-dimensional photonic crystal with a defect mode was demonstrated for the terahertz frequency range.[2] The photonic crystal was designed to achieve a photonic bandgap centered around 100 GHz with a narrow defect mode at the center frequency. The defect mode allowed a narrow band transmission at the center of photonic bandgap, while the transmitted signal was suppressed in the rest of the bandgap. The photonic crystal incorporated two identical sets of alternating compact and low-density layer pairs symmetrically enclosing a defect layer. The compact

---

[2] Reprinted by permission from Springer Nature Customer Service Centre GmbH: Springer S. Park, Y. Li, M. McLamb, B. Norton, G. D. Boreman, and T. Hofmann, "Highly Localized Defect Mode in Polymer-Based THz Photonic Crystals Fabricated Using Stereolithography," *J. Infrared, Millimeter, Terahertz Waves* **41**, 825 - 833 (2020). © 2020

layers consisted entirely of polymethacrylate with no intentional internal structures, while the low-density layers were composed of sub-wavelength sized columns. The columnar structures had a volumetric fraction selected to provide a desired index contrast between the adjacent layers. The photonic crystal samples were fabricated in a single step stereolithography using a commercial system. THz transmission spectroscopy measurements were carried out to determine the optical response of the sample in a range from 82 to 125 GHz. Stratified optical layer model calculations were used to evaluate the transmission data. A distinct photonic bandgap with a defect mode centered at 99 GHz was observed in the experimental transmission spectra. A good agreement between the relevant model parameters and the corresponding design parameters was found.

3.2.1 Introduction

Additive manufacturing techniques have been recognized as rapid and cost-efficient solutions for rapid prototyping of THz optical elements such as gratings [1], waveguides [3, 4], broad-band absorbers [14, 13], and anisotropic metamaterials [29]. Among the additive manufacturing techniques used for the fabrication of THz optical components, stereolithography has demonstrated a superior spatial resolution on the order of 10 µm and a substantially smaller surface roughness compared to other techniques [6, 10]. Reflective THz optical components have been demonstrated by the metalization of stereolithographically fabricated, polymer-based reflectors [11, 12]. These reflective components exhibit a surface roughness of approximately 5 µm and can achieve THz optical responses comparable to commercially available optics [12].

THz frequency bands with very high reflectivity can also be realized by periodic structures consisting of dielectric materials [20]. Such spatially periodic arrangements of sub-wavelength scale constituents, commonly known as photonic crystals, influence the propagation of electromagnetic waves and form photonic bandgaps [17]. Photonic crystals have been studied extensively for wide range of applications, including those for the THz spectral range [30, 31, 23, 19]. The characteristics of the photonic bandgap, in which the propagation of electromagnetic radiation is forbidden, depend on the unit cell of the photonic crystal [17].

Breaking the periodicity of a photonic crystal can lead to highly localized defect modes within the photonic bandgap [32]. A large body of literature can be found on the different approaches of creating defect modes in photonic crystals [33, 34, 35], as well as various applications of narrow defect modes including waveguides [31], resonant cavities [36], and lasers [37]. Many publications are dedicated to one-dimensional (1D) photonic crystals with defect modes operating in the THz spectral range [38, 39, 40, 41].

We have recently demonstrated a THz 1D photonic crystal using single-step polymethacrylate-based stereolithography [42]. Stereolithography enables fabrication of virtually any complex geometry with sub-wavelength sized constituents for THz spectral range. Stereolithography, therefore, could be a readily available new paradigm for the efficient fabrication of THz 1D photonic crystals, for which otherwise complex ceramic-epoxy-based processes are required [24, 15].

In this paper, we report for the first time on design and fabrication of 1D photonic crystals with so-called twinning defects [43] using polymethacrylate-based stereolithography. A narrow defect mode in the photonic crystal demonstrated here was obtained by a defect layer symmetrically enclosed with two identical pairs of alternating layers. Stereolithography is demonstrated to be a versatile approach for fabrication of THz 1D photonic crystals with designed defects.

3.2.2 Experiment

3.2.2.1 Design and fabrication

The 1D photonic crystals demonstrated here comprise two sets of alternating compact and low-density layer pairs symmetrically enclosing a defect layer as shown in Fig. 3.4. The alternating compact and low-density layers have plane parallel interfaces and were fabricated using a single step polymethacrylate based stereolithography. The low-density layers consist of sub-wavelength sized columnar structures with a square base oriented normal to the parallel interfaces of layers. The inset of Fig. 3.4 illustrates one unit cell of the columnar structures including the dimensions of the columnar structures and adjacent layers.

The compact layers are composed entirely of polymethacrylate with no intentional internal structure and thus exhibit a higher polymethacrylate density than the adja-

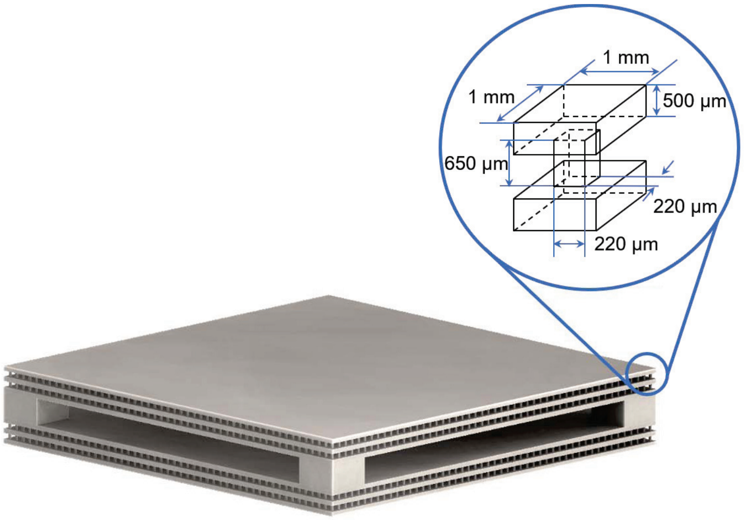

Figure 3.4: CAD model of the 1D photonic crystal with the twinning defect investigated here. The low-density layers are composed of vertical columns with a square base that are arranged in a square lattice pattern as shown in the inset.

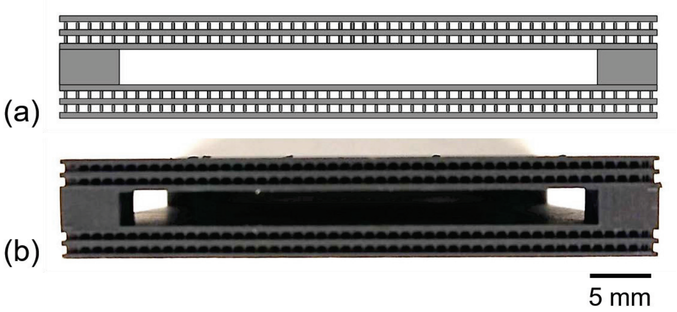

Figure 3.5: (a) A side view of the CAD model of the photonic crystal showing the alternating layers and the defect layer (b) Photographic image of a side view of the fabricated photonic crystal sample. The fabricated sample appears to be close to true-to-form compared to the nominal CAD design.

cent low-density layers. The dielectric function of the compact layers is denoted by $\varepsilon_{\mathrm{com}}$ and is based on the previously reported dielectric function of the polymethacrylate (black v3, Formlabs Inc.) employed here [25, 44]. The effective dielectric function of the low-density layers $\varepsilon_{\mathrm{low}}^{\mathrm{eff}}$ is calculated using the well-known Bruggeman effective medium approximation (EMA). This homogenization approach was previously reported to provide an accurate description of the optical response of layers with subwavelength sized inclusions (see for instance Ref. [42, 26]). The complex dielectric function resulting from this method is governed by the volumetric fraction of the polymethacrylate inclusions f_{i} and their dielectric function ε_{i} [27]:

$$\begin{aligned}\varepsilon_{\mathrm{low}}^{\mathrm{eff}}(f_{\mathrm{i}}) &= \frac{1}{4}\Big\{(3f_{\mathrm{i}}-1)\varepsilon_{\mathrm{i}} + (2-3f_{\mathrm{i}})\varepsilon_{\mathrm{h}} \pm \\ &\quad \sqrt{[(3f_{\mathrm{i}}-1)\varepsilon_{\mathrm{i}} + (2-3f_{\mathrm{i}})\varepsilon_{\mathrm{h}}]^2 + 8\varepsilon_{\mathrm{i}}\varepsilon_{\mathrm{h}}}\Big\}.\end{aligned} \tag{3.2}$$

The complex dielectric functions of the inclusions (black v3, Formlabs Inc.) and the host (air) are denoted by ε_{i} and ε_{h}, respectively, where $\varepsilon_{\mathrm{i}} = \varepsilon_{\mathrm{com}}$.

Spacers were placed on each corner of the square sample, to form a defect layer symmetrically enclosed in between a pair of 5 alternating compact and low-density layers. The defective layer has dielectric function of ε_{h} for air.

The geometry of the 1D photonic crystal was optimized through stratified layer optical model calculations to achieve desired spectral positions of the photonic bandgap and the defect mode. Stratified layer optical model calculations allow a fast and accurate evaluation of the optical response for 1D photonic crystals. This approach is an effective alternative to time consuming finite element based simulations, which are often required for the numerical evaluation of more complex photonic crystal structures [26]. Here, a commercial software package (WVASE32$^{\mathrm{TM}}$, J.A. Woollam Company) was employed for the stratified optical model calculations. The optical layer model developed here comprises 5 layers of alternating compact and low-density layers – a defect layer – 5 layers of alternating compact and low-density layers all in an air ambient. The center frequency of the photonic bandgap and the position of the defect mode within the bandgap were both optimized to be approximately 100 GHz, which is near the center of W-band frequencies. The thickness of the low-density layers, the thickness of the compact layers, and the volumetric fraction of the columnar structures comprising the low-density layers were varied within the parameter window limited by the resolution of the stereolithographic system employed here. Once the optimized geometry was obtained using the stratified layer model, finite element based calculations were performed for comparison using a commercial finite element modeling software (COMSOL Multiphysics, COMSOL Inc.). This was to ensure that the stratified layer model calculations can be used for the regression based evaluation of the experimental data by varying relevant parameters, which can be very time consuming using finite element based calculations.

As a result of these model calculations, the nominal geometry of the photonic crystal was obtained (see Figs. 3.4 and 3.5). The thickness of the compact layers was selected to be 500 µm and the thickness of the low-density layers was determined to be 650 µm. The volumetric fraction of the columnar inclusions f_{i} was selected to be 0.05. A crystal composed of two sets of alternating compact and low-density layer pairs and a 2950 µm defect layer with plane parallel interfaces was chosen as the final design. The normal incidence transmission spectrum calculated using stratified layer optical model (blue solid line) and finite element based model (symbols) for the same nominal geometry are shown in Fig. 3.6 (a). The two calculated spectra are virtually identical for the given geometry. The normal incidence transmission spectrum of the as-designed photonic crystal is dominated by a photonic bandgap in the range from approximately 80 GHz to 120 GHz where the transmission is suppressed by 95%. Centered at 100 GHz a sharp defect mode can be recognized where the maximum transmittance is approximately 0.55. Based on the excellent match between the transmission data obtained by EMA based stratified model calculations and finite element based calculations, we conclude that stratified layer model calculations can be used here to for the analysis of the experimental transmission data, substituting the considerably more time consuming finite element based modeling simulation process.

3D CAD model of the photonic crystals with the finalized dimensions were obtained using a commercial software package (SolidWorks, Dassault Systèmes). The fabricated photonic crystal has a surface area of 5×5 cm^2. The photonic crystal was obtained from a single stereolithographic fabrication step using a commercially available stereolithography system (Form2, Formlabs. Inc.) incorporating a resin compatible with the system (black v3, Formlabs. Inc.). The stereolithography system employed here uses an inverted bottom-to-top fabrication approach. This approach utilizes a UV laser with a wavelength of 405 nm to photopolymerize the resin layer by layer in order to achieve complex three-dimensional objects [45]. In inverted bottom-to-top fabrication processes, sample components must be fixed onto the build platform using support structures [45, 28]. This enables fabrication of samples with an arbitrary orientation with respect to the polymerization plane. Here, the parallel interfaces of photonic crystal samples were oriented perpendicular to the polymerization plane during the fabrication process to prevent any unpolymerized resin from accumulating within the low-density layers.

Following the polymerization process, the sample was immersed in isopropyl alcohol for 15 min and subsequently rinsed thoroughly for an additional 10 min in isopropyl alcohol to remove the excess unpolymerized resin. After the rinsing process, the sample was dried at room temperature until the isopropyl alcohol was completely evaporated from the sample. Upon visual inspection, the fabricated sample appeared to be close to true-to-form in comparison to the nominal CAD design as depicted in Fig. 3.5.

3.2.2.2 Data Acquisition and Analysis

The fabricated photonic crystals were characterized through normal incidence THz transmission spectroscopy over the spectral range of 82 to 125 GHz with a spectral resolution of 0.1 GHz. An electronic synthesizer (Synthesizer, Virginia Diodes Inc.) and an extension module (Virginia Diodes Inc.) were used jointly as a source. The radiation from the extension module was collimated using a lens with 60 mm focal length. The collimated radiation was then transmitted through the sample and was focused using a second 60 mm focal length lens, and detected by a broadband power meter (PM3, Erickson Instruments).

The experimental transmission data was analyzed by stratified layer model calculations employing a commercial software package (WVASE32$^{\text{TM}}$, J.A. Woollam Company). During the analysis, relevant geometric parameters (the thickness of the low-density layers, the thickness of the compact layers, the thickness of the cavity, the volume density of the lower density layers, and the thickness non-uniformity for all layers) were varied using a Levenberg-Marquardt-based algorithm until the model-calculated and experimental data were best matched. Note, that the thicknesses of the layers were assumed to be identical for all compact layers. Likewise, the thicknesses and volumetric fractions of all low-density layers were assumed to be the same and varied collectively. In addition, a thickness non-uniformity was included in the optical model to account for fabrication non-idealities. The thickness non-uniformity was assumed to be the same across all layers. The complex dielectric function of the polymethacrylate (ε_{i} and $\varepsilon_{\text{compact}}$) was not varied during the analysis.

3.2.3 Results and discussion

Figure 3.6 (b) depicts the experimental (dashed green line) and best-model calculated (solid red line) normal incidence transmission spectra obtained for the stereolithographically fabricated photonic crystal shown in Fig. 3.5 (b). Experimental data were obtained from 82 to 125 GHz. The best-model calculated data are extrapolated outside of the measured spectral range and show the optical response of the photonic crystal from 70 to 130 GHz.

The experimental and best-model calculated spectra are in very good agreement

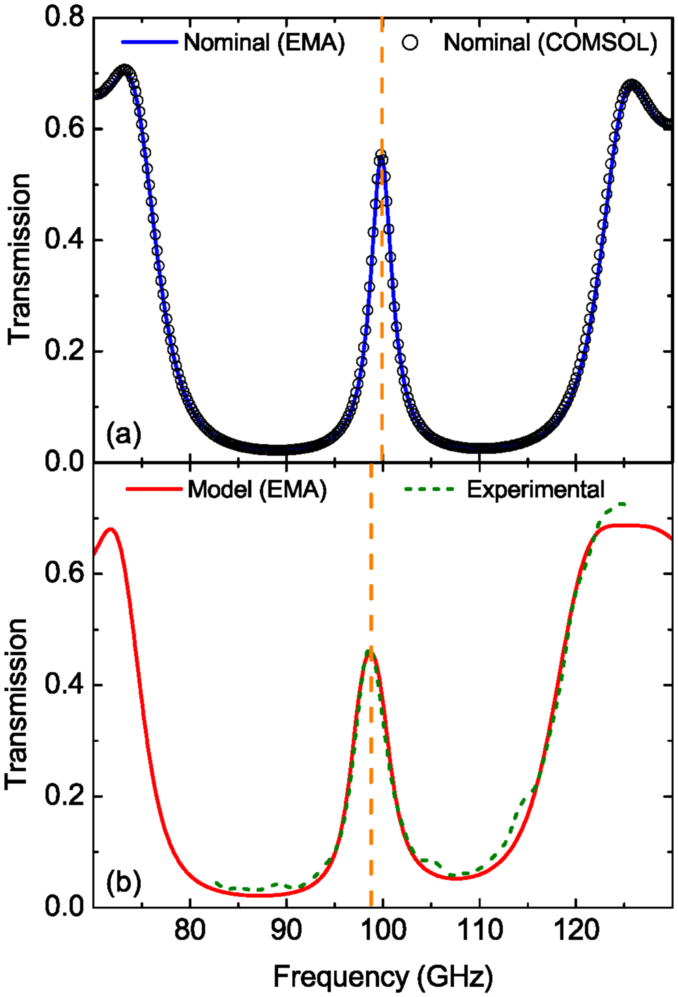

Figure 3.6: (a) Normal incidence transmission spectrum for the nominal geometry calculated using a stratified EMA layer model (blue solid line) and a finite element based model (symbols) in the spectral range from 70 to 130 GHz. Two calculated spectra are virtually identical for the given geometry. A distinct photonic bandgap with a narrow defect mode centered at 100 GHz can be clearly observed. (b) Best-model calculated (red solid line, 70 to 130 GHz) and experimental (dashed green line, 82 to 125 GHz) transmission spectra obtained at normal incidence for the photonic crystal sample. A defect mode is observed at 99 GHz while transmission is strongly suppressed across the rest of the photonic bandgap of the photonic crystal.

over the entire spectral range. A narrow defect mode can be observed at 99 GHz where a maximum transmission of 0.46 is achieved. 90% of transmitted signal in the range from 80 to 110 GHz is suppressed due to the photonic bandgap. The defect mode observed for the fabricated photonic crystal is slightly red-shifted compared to the response expected for the photonic crystal with nominal geometry depicted in Fig. 3.6 (a).

The best-model parameters obtained during the data analysis were 520 ± 3 µm, 675 ± 3 µm and 2901 ± 5 µm for the layer thickness of the compact, the low-density, and the twinning defect, respectively. The best-model value obtained for the volumetric fraction of the columnar inclusions f_{i} of the low-density layers was 0.11 ± 0.1, while the thickness non-uniformity was 3.1 ± 0.1%.

All best-model parameters deviate slightly from the nominal values selected during the design. We attribute these deviations to the limited spatial resolution of the commercial stereolithography system. However, while the deviation for the layer thicknesses is less than 5%, the volumetric fraction deviates by approximately a factor of two. Model calculations reveal that this substantial deviation only results in a slight (1 GHz) red-shift of the spectral positions of the photonic bandgap and the defect mode. The transmission amplitudes of both the photonic bandgap and the defect mode are only very slightly affected. This is a very interesting observation as the control of the volumetric fraction across the photonic crystal appears to be not crucial to obtain a desired optical response.

3.2.4 Summary and conclusion

A polymethacrylate-based 1D photonic crystal with a twinning defect was demonstrated using stereolithography. The investigated 1D photonic crystal samples were composed of two sets of alternating compact and low-density layer pairs symmetrically enclosing a defect layer. The compact layers consisted entirely of polymethacrylate with no intentional internal structures, while the low-density layers were composed of sub-wavelength sized columns oriented perpendicular to the layer interfaces.

The photonic crystal was fabricated in a single fabrication step using a commercial stereolithography system. The optical response of the fabricated crystal was investigated through THz transmission spectroscopy in the spectral range from 82 to 125 GHz at normal incidence. The experimental transmission spectrum exhibits a photonic bandgap with a sharp defect mode centered at 99 GHz. In comparison to the transmission spectra obtained using the nominal geometry, the defect mode in the experimental spectrum is slightly red-shifted by 1 GHz.

Stratified layer optical layer model was employed to analyze the THz transmission data. The dielectric function of the compact layers was based on the previously reported dielectric function of the bulk polymethacrylate. The dielectric function of the low-density layers was accurately described using a Bruggeman EMA. A good agreement between the experimental and best-model THz transmission spectra was found. Discrepancies between the fabricated from the nominal geometry were revealed from the analysis. These discrepancies are the cause of the observed red-shift and are likely due to the limited spatial resolution of the stereolithography system employed here.

REFERENCES

[1] A. D. Squires, E. Constable, and R. A. Lewis, “3d printed terahertz diffraction gratings and lenses,” *J. Infrared Millim. Terahertz Waves* **36**, 72 (2015).

[2] A. Kaur, J. C. Myers, M. I. M. Ghazali, J. Byford, and P. Chahal, “Affordable terahertz components using 3d printing,” in 2015 IEEE 65th Electronic Components and Technology Conference (ECTC), 2071–2076 (2015).

[3] M. Weidenbach, D. Jahn, A. Rehn, S. F. Busch, F. Beltrán-Mejía, J. C. Balzer, and M. Koch, “3d printed dielectric rectangular waveguides, splitters and couplers for 120 ghz,” *Opt. Express* **24**, 28968 (2016).

[4] J. Yang, J. Zhao, C. Gong, H. Tian, L. Sun, P. Chen, L. Lin, and W. Liu, “3d printed low-loss thz waveguide based on kagome photonic crystal structure,” *Opt. Express* **24**, 22454 (2016).

[5] S. F. Busch, M. Weidenbach, J. C. Balzer, and M. Koch, “Thz optics 3d printed with topas,” *J. Infrared Millim. Terahertz Waves* **37**, 303 (2016).

[6] T. D. Ngo, A. Kashani, G. Imbalzano, K. T. Q. Nguyen, and D. Hui, “Additive manufacturing (3d printing): A review of materials, methods, applications and challenges,” *Compos. B. Eng* **143**, 172 (2018).

[7] X. Yan and P. Gu, “A review of rapid prototyping technologies and systems,” *Computer-Aided Design* **28**, 307 (1996).

[8] R. Guo, E.-M. Stuebling, F. Beltran-Mejia, D. Ulm, T. Kleine-Ostmann, F. Ehrig, and M. Koch, “3d printed terahertz rectangular waveguides of

polystyrene and topas: a comparison," *J. Infrared Millim. Terahertz Waves* **40**, 1 (2019).

[9] B. Zhang, B. Seong, V. Nguyen, and D. Byun, "3d printing of high-resolution pla-based structures by hybrid electrohydrodynamic and fused deposition modeling techniques," *J. Micromech. Microeng.* **26**, 025015 (2016).

[10] A. I. Shallan, P. Smejkal, M. Corban, R. M. Guijt, and M. C. Breadmore, "Cost-effective three-dimensional printing of visibly transparent microchips within minutes," *Anal. Chem.* **18**, 3124 (2014).

[11] J. A. Colla, R. E. M. Vickers, M. Nancarrow, and R. A. Lewis, "3d printing metallised plastics as terahertz reflectors," *J. Infrared Millim. Terahertz Waves* **40**, 752 (2019).

[12] D. B. Fullager, S. Park, C. Hovis, Y. Li, J. Reese, E. Sharma, S. Lee, C. Evans, G. D. Boreman, and T. Hofmann, "Metalized poly-methacrylate off-axis parabolic mirrors for terahertz imaging fabricated by additive manufacturing," *J. Infrared Millim. Terahertz Waves* **40**, 269 (2019).

[13] S. Park, Z. Z. Clark, Y. Li, M. McLamb, and T. Hofmann, "A stereolithographically fabricated polymethacrylate broadband thz absorber," *2019 IEEE 16th International Conference on Smart Cities: Improving Quality of Life Using ICT & IoT and AI (HONET-ICT)*, 217 (2019).

[14] M. Petroff, J. Appel, K. Rostem, C. L. Bennett, J. Eimer, T. Marriage, J. Ramirez, and E. J. Wollack, "A 3d-printed broadband millimeter wave absorber," *Rev. Sci. Instrum.* **90**, 024701 (2019).

[15] S. Kirihara, "Fabrication of photonic crystal cavities for terahertz wave resonations," *Nanofabrication* 267 (2011).

[16] X. Lu, Y. Lee, S. Yang, Y. Hao, J. Evans, and C. Parini, “Extrusion freeforming of millimeter wave electromagnetic bandgap (ebg) structures,” *Rapid Prototyp. J.* **15**, 42 (2009).

[17] E. Yablonovitch, “Inhibited spontaneous emission in solid-state physics and electronics,” *Phys. Rev. Lett.* **58**, 2059 (1987).

[18] J. D. Joannopoulos, P. R. Villeneuve, and S. Fan, “Photonic crystals,” *Solid State Commun.* **102**, 165 (1997).

[19] W. Withayachumnankul, B. M. Fischer, and D. Abbott, “Quarter-wavelength multilayer interference filter for terahertz waves,” *Opt. Commun.* **281**, 2374 (2008).

[20] N. Krumbholz, K. Gerlach, F. Rutz, M. Koch, R. Piesiewicz, T. Kürner, and D. Mittleman, “Omnidirectional terahertz mirrors: A key element for future terahertz communication systems,” *Appl. Phys. Lett.* **88**, 202905 (2006).

[21] S.-Z. A. Lo and T. E. Murphy, “Nanoporous silicon multilayers for terahertz filtering,” *Opt. Lett.* **34**, 2921 (2009).

[22] D. Turchinovich, A. Kammoun, P. Knobloch, T. Dobbertin, and M. Koch, “Flexible all-plastic mirrors for the thz range,” *Appl. Phys. A* **74**, 291 (2002).

[23] C. Jansen, S. Wietzke, V. Astley, D. M. Mittleman, and M. Koch, “Mechanically flexible polymeric compound one-dimensional photonic crystals for terahertz frequencies,” *Appl. Phys. Lett.* **96**, 111108 (2010).

[24] W. Chen, S. Kirihara, and Y. Miyamoto, “Fabrication of three-dimensional micro photonic crystals of resin-incorporating tio2 particles and their terahertz wave properties,” *J. Am. Ceram. Soc.* **90**, 92 (2007).

[25] S. Park, Y. Li, D. B. Fullager, S. Schöche, C. M. Herzinger, G. D. Boreman, and T. Hofmann, "Terahertz to mid-infrared dielectric properties of polymethacrylates for stereolithographic single layer assembly," *J. Infrared Millim. Terahertz Waves* **40**, 971 (2019).

[26] Y. Li, D. B. Fullager, S. Park, D. Childers, R. Fesperman, G. Boreman, and T. Hofmann, "High-contrast infrared polymer photonic crystals fabricated by direct laser writing," *Opt. Lett.* **43**, 4711 (2018).

[27] W. Cai and V. Shalaev, Optical metamaterials: fundamentals and applications, (Springer, New York, 2010).

[28] G. Taormina, C. Sciancalepore, M. Messori, and F. Bondioli, "3d printing processes for photocurable polymeric materials: technologies, materials, and future trends," *J. Appl. Biomater. Func.* **16**, 151 (2018).

[29] S. Park, Y. Li, D. Fullager, S. Schöche, C. Herzinger, S. Lee, and T. Hofmann, "Terahertz-frequency dielectric anisotropy in three-dimensional methacrylates fabricated by stereolithography," *Opt. Lett.* **45**, 1982 (2020).

[30] P. Russell, "Photonic crystal fibers," *Science* **299**, 358 (2003).

[31] S.-Y. Lin, E. Chow, V. Hietala, P. R. Villeneuve, and J. Joannopoulos, "Experimental demonstration of guiding and bending of electromagnetic waves in a photonic crystal," *Science* **282**, 274 (1998).

[32] E. Yablonovitch, T. Gmitter, R. Meade, A. Rappe, K. Brommer, and J. Joannopoulos, "Donor and acceptor modes in photonic band structure," *Phys. Rev. Lett.* **67**, 3380 (1991).

[33] D. R. Smith, R. Dalichaouch, N. Kroll, S. Schultz, S. L. McCall, and P. M.

Platzman, “Photonic band structure and defects in one and two dimensions,” *J. Opt. Soc. Am. B* **10**, 314 (1993).

[34] H. Han, H. Park, M. Cho, and J. Kim, “Terahertz pulse propagation in a plastic photonic crystal fiber,” *Appl. Phys. Lett.* **80**, 2634 (2002).

[35] H.-Y. Lee and T. Yao, “Design and evaluation of omnidirectional one-dimensional photonic crystals,” *J. Appl. Phys.* **93**, 819 (2003).

[36] Y. Akahane, T. Asano, B.-S. Song, and S. Noda, “High-q photonic nanocavity in a two-dimensional photonic crystal,” *Nature* **425**, 944 (2003).

[37] O. Painter, R. Lee, A. Scherer, A. Yariv, J. O’brien, P. Dapkus, and I. Kim, “Two-dimensional photonic band-gap defect mode laser,” *Science* **284**, 1819 (1999).

[38] Y. Yu, J. Cai, J. Sun, Z. Zhang, and H. Qin, “Fabrication and characterization of a wide-bandgap and high-q terahertz distributed-bragg-reflector micro cavities,” *Opt. Commun.* **426**, 84 (2018).

[39] H. Němec, L. Duvillaret, F. Garet, P. Kužel, P. Xavier, J. Richard, and D. Rauly, “Thermally tunable filter for terahertz range based on a one-dimensional photonic crystal with a defect,” *J. Appl. Phys.* **96**, 4072 (2004).

[40] H. Němec, P. Kužel, L. Duvillaret, A. Pashkin, M. Dressel, and M. Sebastian, “Highly tunable photonic crystal filter for the terahertz range,” *Opt. Lett.* **30**, 549 (2005).

[41] F. Rutz, N. Krumbholz, L. Micele, G. de Portu, D. Mittleman, and M. Koch, “Improved dielectric mirrors for the thz frequency range,” *Millimeter-Wave and Terahertz Photonics*, **6194**, 61940K (2006).

[42] S. Park, Y. Li, B. Norton, M. McLamb, G. D. Boreman, and T. Hofmann, “One-dimensional photonic crystals fabricated using stereolithographic single layer as-

sembly for the terahertz spectral range," *J. Infrared Millim. Terahertz Waves* **41**, 542 (2020).

[43] H. Němec, L. Duvillaret, F. Quemeneur, and P. Kužel, "Defect modes caused by twinning in one-dimensional photonic crystals," *J. Opt. Soc. Am. B* **21**, 548 (2004).

[44] S. Park, Y. Li, D. B. Fullager, M. Lata, P. Kühne, V. Darakchieva, and T. Hofmann, "Terahertz optical properties of polymethacrylates after thermal annealing," *J. Vac. Sci. Technol. B* **37**, 062924 (2019).

[45] Formlabs, Installation and Usage Instructions Form 2 Desktop Stereolithrgraphy 3D Printer (2018).

CHAPTER 4: MECHANICAL TUNING OF THE THZ PHOTONIC BANDGAP IN POLYMER-BASED ONE-DIMENSIONAL PHOTONIC CRYSTALS

4.1 Mechanical Tuning of the Terahertz Photonic Bandgap of 3D-Printed One-Dimensional Photonic Crystals

Mechanical tuning of a 3D-printed, polymer-based one-dimensional photonic crystal was demonstrated in the terahertz spectral range.[1] The investigated photonic crystal consists of 13 alternating compact and low-density layers and was fabricated through single-step stereolithography. While the compact layers are entirely polymethacrylate without any intentional internal structures, the low-density layers contain sub-wavelength sized slanted columnar inclusions to allow the mechanical compression in a direction normal to the layer interfaces of the photonic crystal. Terahertz transmission spectroscopy of the photonic crystal was performed in a spectral range from 83 to 124 GHz as a function of the compressive strain. The as-fabricated photonic crystal showed a distinct photonic bandgap centered at 109 GHz, which blue shifted under compressive stress. A maximum shift of 12 GHz in the bandgap center frequency was experimentally demonstrated. Stratified optical models incorporating simple homogeneous and inhomogeneous compression approximations were used to analyze the transmission data. A good agreement between the experimental and model-calculated transmission spectra was found.

---

[1] Reprinted by permission from Springer Nature Customer Service Centre GmbH: Springer S. Park, B. Norton, G. D. Boreman, and T. Hofmann, "Mechanical Tuning of the Terahertz Photonic Bandgap of 3D-Printed One-Dimensional Photonic Crystals," *J. Infrared, Millimeter, Terahertz Waves* **42**, 220 - 228 (2021). © 2021

4.1.1 Introduction

Additive manufacturing techniques have recently gained attention as tools for direct fabrication of classical optical components including lenses [1, 2, 3], filters [4, 5], waveguides and diffractive optics [6, 7] for the terahertz (THz) spectral range. While the majority of the research is focused on fused-filament deposition approaches, stereolithography has been demonstrated as a viable alternative in particular for applications where low surface roughness and high spatial resolution are required [8, 9]. State-of-the-art commercial stereolithography systems can achieve spatial resolutions on the order of 10 µm and therefore allow the synthesis of functional THz optical components with significantly improved surface roughness compared to other additive manufacturing techniques [10]. The spatial resolution achieved with stereolithography systems further enables the fabrication of polymethacrylate-based, one-dimensional photonic crystals for the THz spectral range [11].

Photonic crystals are composed of periodically arranged sub-wavelength-sized constituents, which influence propagation of electromagnetic radiation by forming photonic bandgaps [12]. Propagation of electromagnetic radiation with energies within the photonic bandgap is prohibited, resulting in spectral regions with high reflectivity [13]. The characteristics of the photonic bandgap, such as spectral position and width, depend on the geometry of the unit cell and the dielectric properties of the photonic crystal [12]. This dependency can be utilized to achieve dynamically tunable photonic crystals through thermal [14] and electrical stimuli [15, 16]. Several publications demonstrated tunable photonic crystals and other dynamic optical components in THz spectral range [17, 18, 19, 20].

Common to these tuning approaches is to change the dielectric function of the photonic crystal constituents, which results in a change of the energy of the photonic bandgap [21]. Mechanical tuning of photonic crystals has also been studied, in which geometrical changes of the photonic crystal structure are primarily exploited [22].

While a large body of literature exists on mechanically tunable photonic crystals designed for the infrared and visible spectral range, e.g. [23, 24, 25], mechanical tuning of photonic crystals designed for the THz spectral range has not yet been widely explored [26].

In this paper, we demonstrate the mechanical tuning of stereolithographically fabricated one-dimensional photonic crystals in the THz frequency range. We achieve the maximum shift of 12 GHz in the center frequency of the photonic bandgap by applying compressive stress normal to the layer interfaces of the photonic crystal. Stratified optical layer calculations are used to analyze THz transmission spectra obtained at normal incidence in the range from 83 to 124 GHz.

4.1.2 Experiment

4.1.2.1 Design and fabrication

The photonic crystals studied here are composed of six low-density and seven compact layers alternating throughout the structure. The alternating layers have plane parallel interfaces and were fabricated through single step stereolithography, using a single polymethacrylate which is semitransparent in the THz spectral range [9]. The compact layers consist of polymethacrylate without any intentional internal structure. The low-density layers are composed of sub-wavelength sized columnar structures with a square base oriented at 45° with respect to the layer interfaces. A schematic of the photonic crystal including the unit cell is depicted in Fig. 4.1. The orientation of the columnar structures was chosen so that the low-density layers are compressible when subjected to an external force normal to the layer interfaces as indicated by the arrows in Fig. 4.1.

Stratified optical layer model calculations using the commercial software package (WVASE32$^{\text{TM}}$, J.A. Woollam Co., Inc.) were employed to determine an optimal design of a photonic crystal with a bandgap located in the F-band with a center frequency of approximately 112 GHz. Optical model calculations for the design shown in

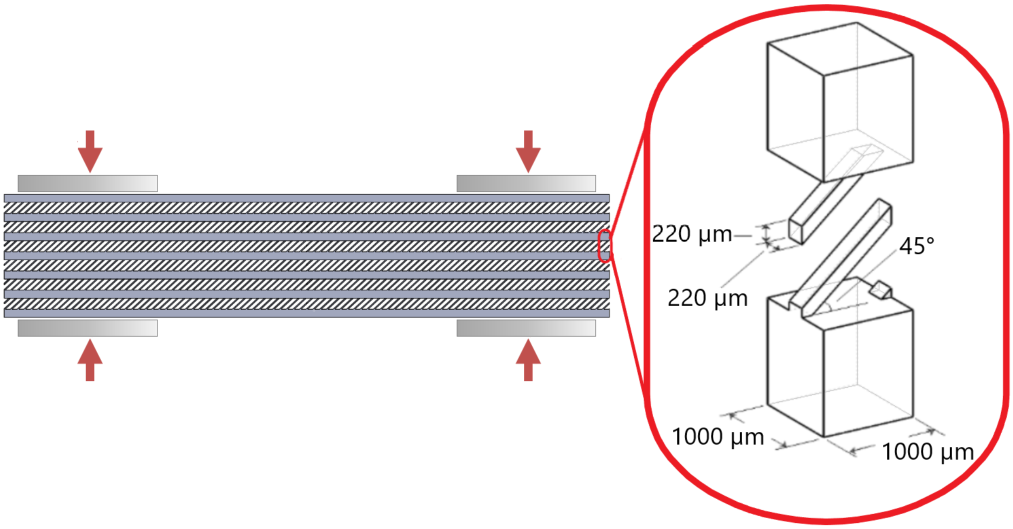

Figure 4.1: A side view schematic of the photonic crystal composed of 13 alternating compact and low-density layers. The direction of the external force is normal to the layer interfaces as indicated by the red arrows. The low-density layers are composed of columnar structures oriented at 45° with respect to the layer interfaces and arranged in square lattice pattern as shown in the inset. The slanting plane is perpendicular to the interface of the layers.

Fig. 4.1 only require the knowledge of the dielectric function of the compact layers as the dielectric function of the low-density layers can be obtained using the Bruggeman effective medium approximation [11, 27]. The dielectric function of the polymethacrylate (black v4, Formlabs Inc.), which was used for the fabrication of the photonic crystals investigated here, is well known and was determined using spectroscopic ellipsometry in the infrared and THz spectral range [9]. The dielectric function for the low-density layers $\varepsilon_{\mathrm{l}}^{\mathrm{eff}}$ is described using the Bruggeman effective medium approximation as the columnar structures shown in Fig. 4.1 are sufficiently small compared to the wavelength of the incident THz radiation.

$\varepsilon_{\mathrm{l}}^{\mathrm{eff}}$ can be expressed as a function of the volumetric fraction of the columnar inclusions f_{i}, the dielectric function of the columnar inclusions ε_{i}, which in our case is the dielectric function of the polymethacrylate, and the dielectric function of the host ε_{h}, air [28]:

$$\varepsilon_{\mathrm{l}}^{\mathrm{eff}}(f_{\mathrm{i}}) = \frac{1}{4}\Big\{(3f_{\mathrm{i}}-1)\varepsilon_{\mathrm{i}} + (2-3f_{\mathrm{i}})\varepsilon_{\mathrm{h}} \pm \sqrt{[(3f_{\mathrm{i}}-1)\varepsilon_{\mathrm{i}} + (2-3f_{\mathrm{i}})\varepsilon_{\mathrm{h}}]^2 + 8\varepsilon_{\mathrm{i}}\varepsilon_{\mathrm{h}}}\Big\}. \tag{4.1}$$

For slanted columnar inclusions with a square cross section arranged in a square lattice pattern as shown in Fig. 4.1, the volumetric fraction of the inclusions f_{i} can be expressed as a function of the thickness of the low-density layer d_{l} and a coefficient f_0, derived from the width of the columnar structures w_{c}, the width of the unit cell w_{u}, and the length of the columnar structures l_{c}:

$$f_{\mathrm{i}}(d_{\mathrm{l}}) = \frac{w_{\mathrm{c}}^2 l_{\mathrm{c}}}{w_{\mathrm{u}}^2}\frac{1}{d_{\mathrm{l}}} = f_0\frac{1}{d_{\mathrm{l}}}. \tag{4.2}$$

Thus, $\varepsilon_{\mathrm{l}}^{\mathrm{eff}}$ presented in Eqn. (4.1) is a function of the low-density layer thickness d_{l}. The optimized nominal values to achieve a photonic bandgap centered at 112 GHz are $f_{\mathrm{i}} = 0.05$, $d_{\mathrm{l}} = 1800$ µm, and $d_{\mathrm{c}} = 1300$ µm.

Figure 4.2 shows the calculated transmission spectra for the nominal photonic crystal design in the range from 82 to 125 GHz for several different compressive strain values $\Delta d_{\mathrm{l}}/d_{\mathrm{l}} = 0$, , 0.10, and 0.15. It can be clearly seen that the photonic bandgap, which is centered around 112 GHz for $\Delta d_{\mathrm{l}}/d_{\mathrm{l}} = 0$, shifts to higher frequencies as the compressive strain is increased. For $\Delta d_{\mathrm{l}}/d_{\mathrm{l}} = 0.15$, a center frequency of 120 GHz can be observed. The minimum transmission of the photonic bandgap also slightly increases with increasing compressive strain. For the calculations, a homogeneous compression model was implemented. In this model, the low-density layers are assumed to be homogeneously compressed and thus their dielectric function can be expressed as a function of the thickness following Eqns. (4.1) and (4.2).

The photonic crystal structure was designed using a 3D CAD software (SolidWorks, Dassault SystÃšmes) and fabricated using a commercial 3D printer (Form 2, Formlabs

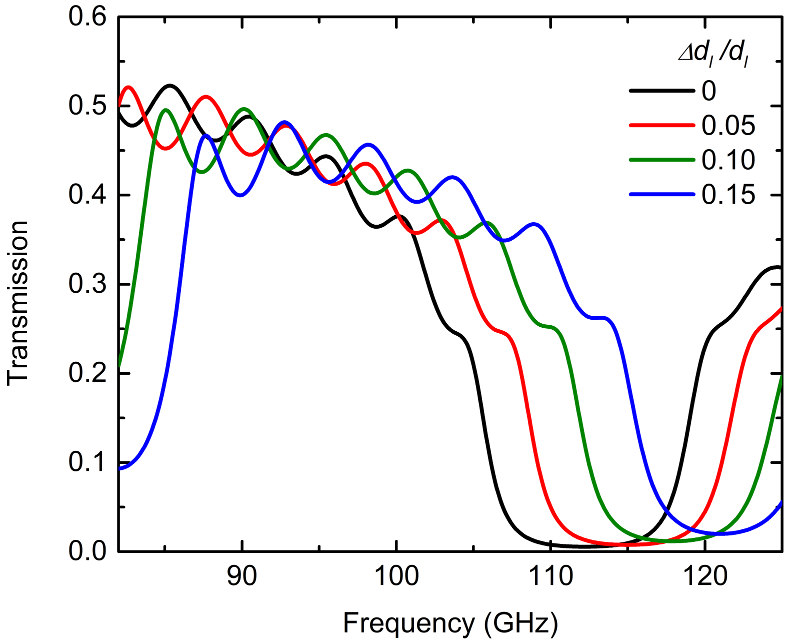

Figure 4.2: Model calculated spectra of the photonic crystal for compressive strain values in the low-density layers, $\Delta d_\mathrm{l}/d_\mathrm{l} = 0$, 0.05, 0.10, and 0.15. The bandgap center frequency is blue shifted and the minimum transmission slightly increases with increasing compressive strain.

Inc.). The printer uses an inverted top-down approach, employing a 405 nm UV laser to polymerize a photosensitive resin (black v4, Formlabs Inc.) onto a printing platform layer by layer. This requires support structures to keep the printed object fixed to the printing platform, which allows the object to be printed in an arbitrary position. The photonic crystals investigated here were oriented at a 45° angle relative to the normal of the printing platform to prevent any unpolymerized resin from accumulating within the structure throughout the printing process. After the photonic crystal was printed, all support structures were removed and the sample was placed in an isopropanol bath for 20 minutes. It was then thoroughly rinsed with isopropanol for additional 10 minutes before it was dried using pressurized air to remove any excess resin or isopropanol from the low-density layers.

4.1.2.2 Data Acquisition and Analysis

An electronic synthesizer (Virginia Diodes Inc.) connected to an extension module (Virginia Diodes Inc.) was used as a source. The emitted radiation was collimated using a 60 mm focal length lens before being transmitted through the photonic crystal sample. The beam transmitted through the photonic crystal was then focused into a broadband power meter (PM3, Erickson Instruments) using a second 60 mm focal length lens and the power was recorded as a function of frequency and compressive strain, which was measured using a micrometer caliper. Figure 4.1 illustrates how the photonic crystal was compressed to mechanically tune its optical response. The direction of the compressive stress is indicated by red arrows. The photonic crystal was orientated such that the polarization direction of the source radiation is parallel to the slanting plane of the columnar structures. This high-symmetry orientation avoids polarization mode conversion due to form-birefringence caused by the slanted columnar structures, which were in Ref. [29]. The spectral response of the photonic crystal was measured for two compressive strain values $\Delta d_{\rm l}/d_{\rm l}$ = 0.18±0.01, and 0.21±0.01 in the range from 83 to 124 GHz with a resolution of 0.1 GHz.

The experimental THz transmission data shown in Fig. 4.3 were analyzed using stratified layer model calculations employing a commercial software package (WVASE32$^{\rm TM}$, J.A. Woollam Company). The optical model used to analyze the un-strained, as fabricated photonic crystal is composed of 13 layers alternating between compact and low-density material as shown in comparison with a schematic of a section of the photonic crystal in Fig. 4.4 a). A LevenbergâMarquardt algorithm is used during the analysis to vary the optical model parameters until the best-match between experimental and model calculated data is achieved. For the as-fabricated photonic crystal the thickness of the constituent layers were varied during the analysis. It was assumed that the dielectric function and layer thickness of the compact and low-density layers is constant throughout the photonic crystal. Therefore, the corresponding parameters

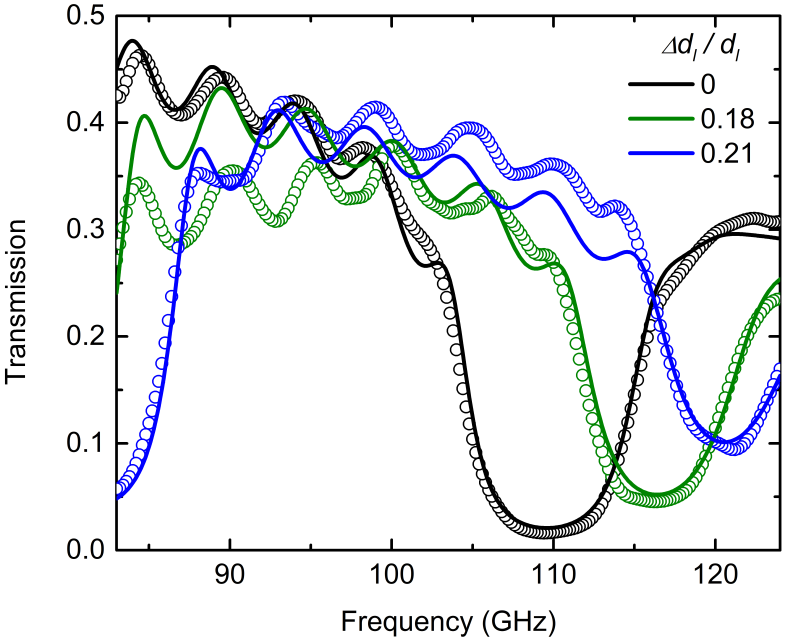

Figure 4.3: Experimental (circles) and best-model calculated (solid lines) transmission spectra of the photonic crystal for different compressive strain values, $\Delta d_\mathrm{l}/d_\mathrm{l}$, in the spectral range from 83 to 124 GHz. Compressing the crystal results in a blue shift of the bandgap's center frequency. The bandgap center frequencies for $\Delta d_\mathrm{l}/d_\mathrm{l} = 0$, 0.18, and 0.21 are found to be 109 GHz, 116 GHz, and 121 GHz with the minimum transmission of 0.02, 0.05, and 0.1, respectively.

of the optical model d_c, d_l, and $\varepsilon_1^\mathrm{eff}$ were varied for all layers simultaneously.

The simple homogeneous compression model introduced in Sect. 4.1.2.1 is insufficient to describe the experimental transmission spectra obtained for the photonic crystal under compressive stress (see Fig. 4.3). Therefore a simple form of an inhomogeneous compression is implemented in the optical model used to analyze the experimental transmission data obtained for the photonic crystal under compressive stress. For this model, which is shown schematically in Fig. 4.4 b), each low-density layer consists of three layers where the low-density layers adjacent to compact layers are treated as incompressible. Thus the resulting three low-density layers resemble a very simple approximation of the experimentally observed compression gradient. The low-density layer thickness, the compact layer thickness, and the volume fraction of the columnar inclusions were varied during this model analysis.

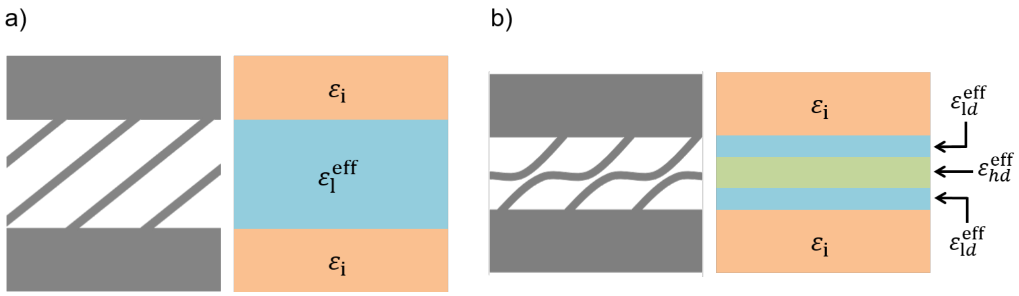

Figure 4.4: Schematic of a set of low-density and compact layers (side view) before a) and after compression b). The layer optical model is shown in comparison. While the low-density and compact layers of the un-strained photonic crystal can be described in the optical model as homogeneous thin films with a thickness d_l and d_c, respectively, this model breaks down for the strained samples. An accurate description of the experimental results needs to account for the experimental inhomogeneous compression. The low density layers are therefore approximated by three layers (d_ld, d_hd) in the optical model. The dielectric functions of these layers are denoted by $\varepsilon_\mathrm{ld}^\mathrm{eff}$ and $\varepsilon_\mathrm{hd}^\mathrm{eff}$.

4.1.3 Results and discussion

Figure 4.3 shows the experimental (circles) and best-model (solid lines) transmission spectra in the spectral range from 83 to 124 GHz and compressive strain $\Delta d_\mathrm{l}/d_\mathrm{l}$ values of 0, 0.18, and 0.21 at normal incidence. All spectra show a distinct photonic bandgap and typical sidelobes. It can be clearly seen that the photonic bandgap shifts to higher frequencies as a function of the compressive strain $\Delta d_\mathrm{l}/d_\mathrm{l}$. In addition to the spectral shift of the main photonic band gap, a secondary photonic bandgap is shifting into experimentally accessible spectral window for the largest strain $\Delta d_\mathrm{l}/d_\mathrm{l} = 0.21$.

The best-model calculated transmission spectra render the experimentally observed response well. In comparison to the calculated transmission spectra obtained with a homogeneous compression model as shown in Fig. 4.2, it can be noted that the increase in the transmission minimum and the change in the shape of the photonic bandgap is well reproduced in the inhomogeneous compression model-based calculated spectra. All experimental transmission spectra were analyzed simultaneously using optical models for which common parameters (ε_i, $\varepsilon_\mathrm{ld}^\mathrm{eff}$, d_c, and d_ld) were not varied independently.

For the un-strained, as-fabricated photonic crystal the model analysis yields d_c=1426±3 µm for the thickness of the compact layers and d_l=1659±5 µm for the thickness of the low-density layers. The best-fit parameters found for the fabricated crystal deviate slightly from the nominal values. We attribute this small deviation to the resolution of the stereolithography system employed here, which has a nominal layer resolution of 25 µm in the direction orthogonal to the polymerization plane and a nominal laser spot size of 140 µm [29].

For a compressive strain of $\Delta d_l/d_l = 0.18 \pm 0.01$, the center frequency of the photonic bandgap is shifted by 7 GHz to 116 GHz, while the transmission minimum increases to 0.05. The best-model parameters for the thicknesses of the low density layers is d_{ld} = 332±10 µm and d_{hd} =714±22 µm. The best-model value for the compressive strain $\Delta d_l/d_l = 0.17 \pm 0.03$, is found to be in good agreement with the value determined mechanically using a micrometer caliper.

For a compressive strain of $\Delta d_l/d_l = 0.21 \pm 0.02$ the center frequency of the photonic bandgap is shifted by 12 GHz to 121 GHz, while the transmission minimum increases to 0.1. In addition, the high-frequency flank of a second photonic bandgap is emerging at the lower end of the experimentally accessible spectral window. The best-model parameters for the thicknesses of the low density layers is d_{ld} = 332±10 µm and d_{hd} =574±22 µm. The best-model value for the compressive strain $\Delta d_l/d_l = 0.25 \pm 0.03$. Similar to the lower compressive strain this values is also found in good agreement with the mechanically determined value.

4.1.4 Summary and conclusion

A mechanically tunable, one-dimensional THz photonic crystal fabricated using stereolithography has been demonstrated for the F-band. The photonic crystal is composed of 13 alternating compact and low-density layers. The compact layers consist of polymethacrylate without any intentional internal structure. The low-density layers are composed of sub-wavelength sized columnar structures that are oriented at 45° relative to the layer interfaces. This slanted columnar design allows the mechanical compression in a direction normal to the layer interfaces.

THz transmission spectroscopy of the photonic crystal was performed in a spectral range from 83 to 124 GHz at normal incidence as a function of the applied compressive stress. The as-fabricated photonic crystal shows a distinctive photonic bandgap centered at 109 GHz. Under compressive stress, applied perpendicular to the layer interfaces, the photonic bandgap shifts to higher frequencies. The largest observed shift is 12 GHz for a compressive strain of $\Delta d_l/d_l = 0.21 \pm 0.02$.

Stratified layer model calculations were used to analyze the THz transmission spectra. An optical model composed of 13 alternating compact and low-density layers. The effective dielectric function of the low-density layers was described through Bruggeman effective medium approximation. This model was found to render the experimental spectrum obtained for as-fabricated photonic crystal accurately. However, this model was found to be insufficient to describe the THz transmission data obtained for photonic crystals subjected to different compressive stresses. Spectral signatures indicative of inhomogeneous compression were observed and led to the development of a simple inhomogeneous compression model, which describes the experimentally observed transmission spectra well.

In conclusion, a mechanically tunable photonic crystal for the THz spectral range is demonstrated using a simple stereolithographic fabrication. We envision a wide range of THz applications including surveillance and sensing for such a structure. Our design allows the mechanical tuning of the photonic bandgap within the F-band.

4.2 Mechanical Tuning of Defect Modes in Polymer-based Terahertz One-dimensional Photonic Crystals Fabricated by Stereolithography

Mechanical tuning of defect modes in a polymer-based one-dimensional photonic crystal was demonstrated for the terahertz spectral range.[2] A sharp defect mode in the photonic bandgap was achieved by symmetrically enclosing a defect layer with two identical pairs of alternating compact and low-density layers. By adjusting the thickness of the defect layer, the spectral position of the defect mode within the photonic bandgap was easily controlled. Normal incidence transmission spectroscopy in a spectral range from 82 to 125 GHz was used to determine the THz spectral response for different defect layer thicknesses. The transmission data were analyzed using stratified optical layer model calculations. Spectral shift of the center frequency of the narrow transmission peak within a distinct photonic bandgap was observed in the experimental transmission spectra. The shift was achieved by mechanical tuning of the defect layer thickness. A good agreement between the relevant model parameters and the corresponding design parameters was found.

4.2.1 Introduction

Advancement in terahertz (THz) optical systems requires optical components that can manipulate the THz wave propagation. Band-stop and band-pass filters that allow broad-band reflection or selective transmission at desired frequencies are some of the essential components for developing an optical system. A well-known solution for such applications utilizes photonic crystals, which are spatially periodic arrangements of sub-wavelength scale constituents that form frequency regions in which the propagation of electromagnetic radiation is prohibited [12]. A photonic crystal, in

---

[2] S. Park, V. P. Stinson, M. McLamb, G. D. Boreman, T. Hofmann, "Mechanical tuning of defect modes in polymer-based terahertz one-dimensional photonic crystals fabricated by stereolithography," accepted in *Opt. Eng.* (2021). © 2021 Society of Photo-Optical Instrumentation Engineers. One print or electronic copy may be made for personal use only. Systematic reproduction and distribution, duplication of any material in this paper for a fee or for commercial purposes, or modification of the content of the paper are prohibited.

its simplest form, can be realized as alternating layers of two dielectrics in one dimension [13]. Such one-dimensional (1D) photonic crystal structures can be realized using dielectric materials for the THz spectral range to exhibit bands in their spectral response with very high reflectivity [30, 31, 32, 20, 33].

When the periodicity of photonic crystal structures is broken, highly localized transmission bands can be formed within the photonic bandgaps [34]. One of the several ways to create such defect modes in photonic crystals is a so-called twinning defect. Such defect modes are formed by two identical pairs of alternating layers symmetrically enclosing a defect layer in a photonic crystal [35]. Many examples of twinning defect modes in 1D photonic crystals have been reported for the THz spectral range [17, 36, 37]. Controlling the spectral characteristics of defect modes is an attractive subject for applications like optical communication and signal multiplexing. Several publications demonstrate mechanically tunable defect modes, based on 1D photonic crystals fabricated by stacking plane parallel layers of dielectric materials [38]. While the stacking method can provide a simple and low-cost solution, it requires each constituent layer of the photonic crystals to be separately fabricated and assembled.

Recently, we have demonstrated polymer-based THz 1D photonic crystals fabricated by stereolithography with high reflection features in the W-band [11]. Stereolithographically fabricated 1D photonic crystals were also successfully used to achieve narrow defect modes [39] as well as mechanical tuning of the bandgap by applying a compressive force [40]. Stereolithography enables fabrication of virtually any complex geometry with sub-wavelength sized constituents for the THz spectral range, and therefore has been introduced as a new paradigm for realizing THz photonic crystals. THz 1D photonic crystals with mechanically tunable defect modes at virtually any spectral position, therefore, can be easily achieved by stereolithography.

In this paper, we report on design and fabrication of 1D photonic crystals with tunable defect modes using polymer-based stereolithography for the first time. The narrow defect mode the photonic crystal demonstrated here was obtained by a void defect layer symmetrically enclosed between two identical pairs of alternating layers. The thickness of the defect layer was controlled mechanically, which resulted in spectral shift in the defect mode within the photonic bandgap. Stereolithography is thus demonstrated to be a versatile approach for fabrication of THz 1D photonic crystals with mechanically tunable, designed defects.

4.2.2 Experiment

4.2.2.1 Design and fabrication

Figure 4.5 illustrates the 1D photonic crystal structure investigated here. The 1D photonic crystal consists of pairs of alternating compact and low-density layers, symmetrically enclosing a void layer. This void layer serves as a defect layer with

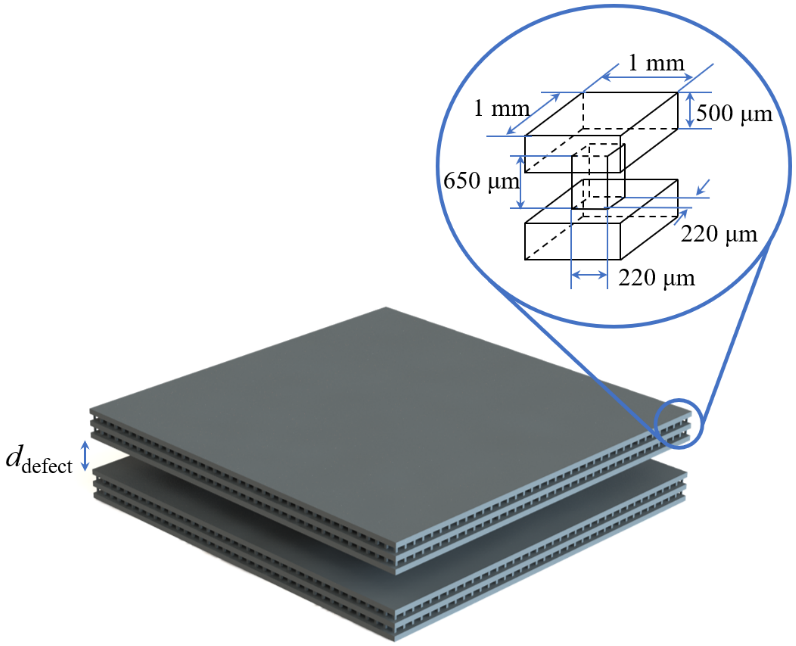

Figure 4.5: CAD model of the 1D photonic crystal with the twinning defect investigated here. The thickness of the void defect layer (d_{defect}) is mechanically tuned in the experiment. The low-density layers are composed of vertical columns with a square base that are arranged in a square lattice pattern as shown in the inset.

plane parallel interfaces, the thickness of which can be mechanically adjusted. The defect layer is a void space enclosed by a pair of Bragg reflectors which causes a sharp transmission mode within the highly reflective photonic bandgap of the photonic crystal. Such defects have been introduced in the literature as twinning defects [35]. This configuration can be compared to a FabryâPérot resonator formed with a pair of Bragg reflectors. Therefore the spectral and amplitude characteristics of the defect modes are governed by the characteristics of both the defect layer and the Bragg reflectors surrounding the defect layer [36]. The spectral position of a defect mode within the photonic bandgap is determined by the optical thickness of the defect layer. Thus the spectral position of the defect mode can be tuned by either varying the physical thickness or by changing the dielectric properties of the layer. In this manuscript we focus on the tuning of the defect mode by mechanical changing the physical thickness of the defect layer.

The design of tunable defect modes in PCs requires predictive formulas for the frequency dependence of the defect modes as function of physical parameters of photonic crystals. The transfer matrix method can provide a good approximation for the center frequency of the photonic bandgap as well as the frequency of the defect mode for one-dimensional photonic crystals [41]. The photonic crystal structure studied here can be expressed as $(HL)^2HDH(LH)^2$ where H and L stands for high and low index layers of the photonic crystal and the defect layer is denoted as D. Each layer of the photonic crystal can be expressed as [41]:

$$M_l = S_l P_l S_l^{-1};\;\; l = H, L, or D. \tag{4.3}$$

The matrix $\mathbf{S_l}$ from the Eq. 4.3 is defined as:

$$S_l^{TE} = \begin{pmatrix} 1 & 1 \\ n_l \cos\theta_l & -n_l \cos\theta_l \end{pmatrix} \qquad S_l^{TM} = \begin{pmatrix} \cos\theta_l & \cos\theta_l \\ n_l & -n_l \end{pmatrix} \tag{4.4}$$

Note that for normal incidence, the transverse electric (TE) and transverse magnetic (TM) modes become identical. The propagation matrix $\mathbf{P_l}$ from Eq. 4.3 is given as:

$$P_l = \begin{pmatrix} e^{i\phi_l} & 0 \\ 0 & e^{-i\phi_l} \end{pmatrix}; \qquad \phi_l = \frac{2\pi d_l}{\lambda} n_l \cos\theta_l, \tag{4.5}$$

where d_l is the thickness of the layer.

For a crystal embedded in air, expressed as Air/$(HL)^2HDH(LH)^2$/Air, the final transfer matrix becomes:

$$M_{final} = \begin{pmatrix} M11 & M12 \\ M21 & M22 \end{pmatrix} = S_0^{-1}(M_H M_L)^2 M_H M_D M_H (M_L M_H)^2 S_0. \tag{4.6}$$

The transmittance and the reflectance of the final system can be found as:

$$T = \left|\frac{1}{M_{11}}\right|^2 \qquad R = \left|\frac{M_{21}}{M_{11}}\right|^2. \tag{4.7}$$

The low-density layers consist of sub-wavelength sized columnar structures and thus exhibit polymethacrylate density lower than the adjacent compact layers. The inset of Fig. 4.5 depicts one unit cell of the columnar structures including the dimensions of the columnar structures and adjacent layers. The compact layers are composed entirely of polymethacrylate without any intentional internal structure. The dielectric function of these compact layers is thus that of the polymethacrylate employed here for fabrication, which is based on the previously reported dielectric function of the polymethacrylate (black v3, Formlabs Inc.) [9]. The effective dielectric function of the low-density layers is obtained using the well-known Bruggeman effective medium approximation (EMA), which has been reported to accurately depict the optical response of the layers with sub-wavelength scale inclusions. Detailed descriptions of its application can be found in our earlier publications on 1D photonic crystal structures with low-density layers for infrared and THz spectral ranges (see for instance [11, 27]).

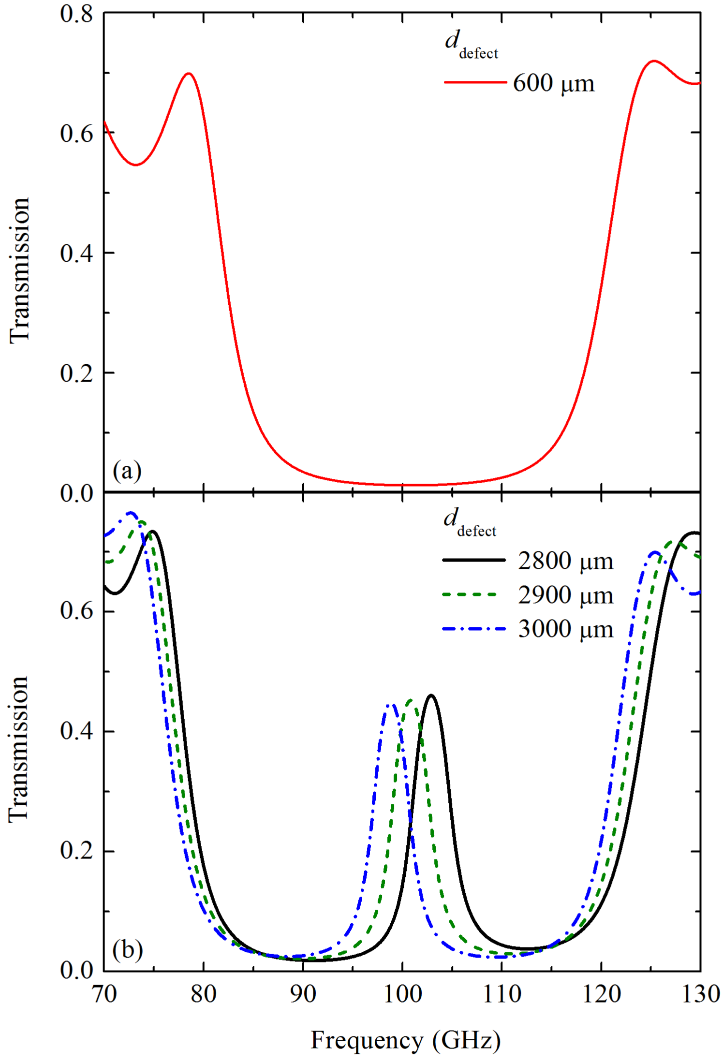

Figure 4.6: Normal incidence transmission spectra calculated using a stratified EMA layer model are shown for various defect layer thicknesses d_{defect} and the nominal geometry in the spectral range from 70 to 130 GHz. (a) A distinct photonic bandgap centered around 100 GHz is formed when d_{defect} is comparable to the low-density layer thickness of the photonic crystal. (b) Calculated photonic bandgaps with a narrow defect mode at the center of the bandgap show a clear shift in spectral position of the defect mode for $d_{\text{defect}} = 2800$, 2900, and 3000 μm

The geometrical parameters of the 1D photonic crystal were optimized to achieve desired spectral positions of the photonic bandgap and the defect mode within the

W-band. Here, a commercial software package (WVASE32$^{\text{TM}}$, J.A. Woollam Company) was employed to perform stratified optical layer model calculations for the optimization. The optical layer model comprises 5 layers of alternating compact and low-density layers − a void defect layer − 5 layers of alternating compact and low-density layers all in an air ambient. This geometry was previously used to successfully obtain a narrow defect mode in a 1D photonic crystal structure [39]. With a symmetrically enclosed defect layer whose thickness can be freely adjusted, such 1D photonic crystal structures are capable of creating broad photonic bandgaps as well as a narrow transmission band within the photonic bandgap depending on the defect layer thickness d_{defect}. The spectral position of the narrow transmission band can be easily adjusted by mechanical tuning of d_{defect}. Figure 4.6 (a) depicts model calculated data of a photonic bandgap when d_{defect} is comparable to the thickness of low-density layers and Fig. 4.6 (b) depicts the photonic bandgap with a defect mode, with a shifting spectral position based on d_{defect}.

The geometrical parameters of the photonic crystal, including the thickness of the low-density layers, the thickness of the compact layers, and the volumetric fraction of the columnar structures comprising the low-density layers, were optimized to achieve a photonic bandgap and a sharp defect mode centered around 100 GHz. The optical model calculation well illustrates the shift in spectral position of this defect mode as a function of the defect mode thickness, as shown in Fig. 4.6 (b). As a result of these model calculations, the nominal geometry of the photonic crystal was finalized. The thickness of the compact layers and the low-density layers were selected to be 500 µm and 650 µm, respectively. The volumetric fraction of the columnar inclusions was chosen to be 0.05.

A 3D CAD model of the optimized photonic crystal was acquired using a commercial software (SolidWorks, Dassault Systèmes). The photonic crystal was stereolithographically fabricated with a commercially available stereolithography system

(Form2, Formlabs. Inc.) and resin (black v4, Formlabs. Inc.). The fabricated samples were thoroughly cleaned for 15 minutes with isopropyl alcohol using a cleaning device compatible with the stereolithography system (Form Wash, Formlabs. Inc.) to remove any excess unpolymerized resin. The samples were subsequently dried using compressed air in order to remove any isopropyl alcohol from the surfaces and the internal structures.

4.2.2.2 Data Acquisition and Analysis

Normal incidence THz transmission spectroscopy was performed over the spectral range of 82 to 125 GHz with 0.1 GHz spectral resolution to characterize the fabricated photonic crystal. An electronic synthesizer (Synthesizer, Virginia Diodes Inc.) and an extension module (WR9.0SGX, Virginia Diodes Inc.) were used in combination as the THz source. The radiation exiting the extension module was collimated using a lens with 60 mm focal length. The collimated radiation was then transmitted through the sample and was then focused using a second 60 mm focal length lens, and detected by a broadband power meter (PM5B, Erickson Instruments). The two pairs of alternating layers comprising the photonic crystal were each fixed onto the optical table and a single-axis translation stage, respectively. The air layer with plane parallel interfaces formed at the center of the photonic crystal structure served as a defect layer in this experiment. By mechanically adjusting the position of layers fixed onto a translation stage, d_{defect} was controlled. The spectral response of the photonic crystal was measured for six different thickness values.

The experimental transmission data were analyzed using stratified layer model calculations using a commercial software package (WVASE32$^{\text{TM}}$, J.A. Woollam Company). All experimental data were analyzed through a simultaneous fitting process. During the analysis, geometric parameters (the thickness of the low-density layers, the thickness of the compact layers, the thickness of the defect layer, the volume density of the lower density layers, and the thickness non-uniformity for the defect layer) were varied until the model-calculated data best matched the experimental data, using a Levenberg-Marquardt-based algorithm. Note that the thicknesses of the layers were assumed to be identical for all compact layers. Likewise, the thicknesses of all low-density layers and their volume densities were assumed to be the same and varied collectively.

4.2.3 Results and discussion

Figure 4.7 (a) illustrates the experimental (symbols) and best-fit model (solid line) data for d_{defect} comparable to the low-density layer of the photonic crystal in the spectral range from 70 to 130 GHz. A distinct photonic bandgap centered around 100 GHz can be clearly noticed. Figure 4.7 (b) shows the experimental (symbols) and best-fit model (solid lines) data for the spectral response of the photonic crystal for three different d_{defect} values. The change in spectral position of the narrow transmission within the photonic bandgap is observed as expected from the model calculations. Experimental and best-fit model spectra are in good agreement over the measured spectral range. The narrow transmission peak observed around 99, 100, and 101 GHz for each d_{defect} as well as the suppression of transmission over the photonic bandgap are well reproduced in the best-model calculated spectra.

The best-model parameters obtained during the data analysis were 524 ± 8 µm, 622 ± 13 µm for the compact layer thickness and the low-density layer thickness, respectively. The experimentally achieved d_{defect} values were 2816 ± 8 µm, 2943 ± 8 µm, and 3070 ± 8 µm. The volumetric fraction of the columnar inclusions of the low-density layers was 0.04 ± 0.01, while the thickness non-uniformity was 4.8 ± 0.1%. The geometrical parameters deviate slightly from the nominal values selected during the design, which is likely due to the limited spatial resolution of the commercial stereolithography system.

A transmission over 0.34 is achieved for the defect modes for all d_{defect} values investigated, while the transmission is well suppressed in the spectral range covered by the photonic bandgap for all measured spectra. The maximum tunable range of the defect mode is limited primarily by the width of the photonic bandgap and is approximately 37 GHz for our fabricated structure. The FWHM spectral width of the defect modes are approximately 6 GHz for all measured data. The maximum transmission observed in the experimental data is lower than the value predicted from

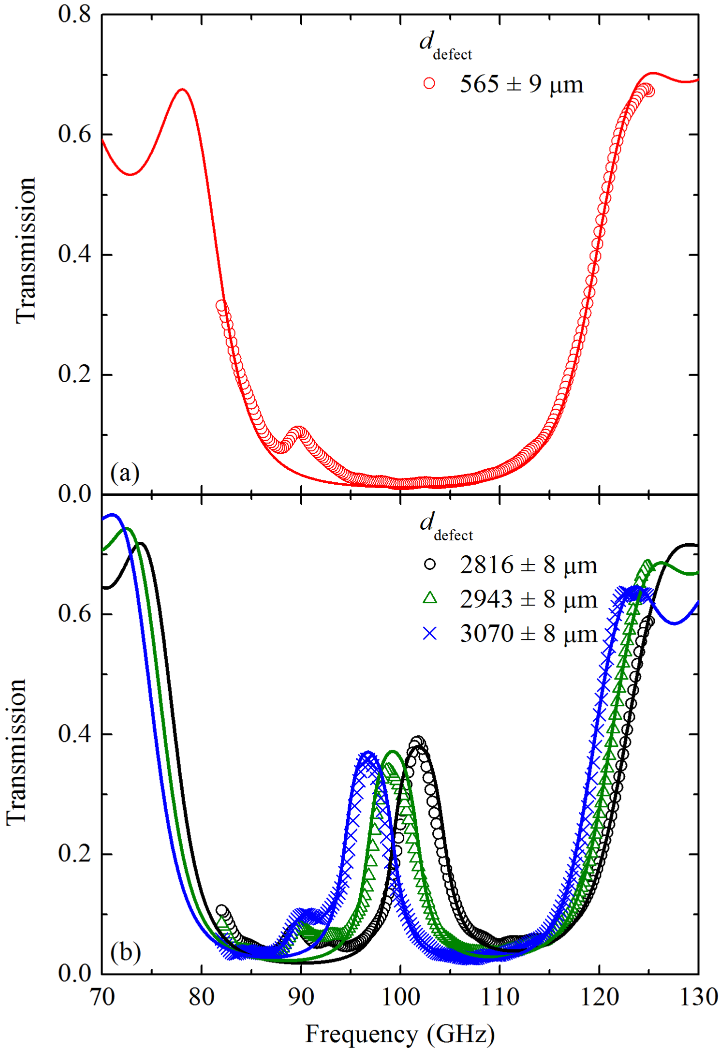

Figure 4.7: Experimental (symbols, 82 to 125 GHz) and best-model calculated (solid lines, 70 to 130 GHz) transmission spectra for normal incidence on the photonic crystal samples for various defect layer thicknesses d_{defect} (a) A distinct photonic bandgap formed with center frequency around 100 GHz is observed when d_{defect} is comparable to the low-density layer thickness of the photonic crystal. (b) A clear shift of a defect mode is observed for three different d_{defect}.

the model calculations, which was well over 0.4 for all defect layer thicknesses. This is attributed to the thickness non-uniformity of the defect layer, which was revealed during the model analysis.

A small parasitic transmission located at approximately 90 GHz can be noticed in all experimental transmission spectra, implying the presence of extra defective features within the investigated crystal. The amplitude and spectral position of this peak remains constant for all experimental data associated with different defect layer thicknesses, indicating that it is not directly related to the defect layer. This low transmission feature is therefore tentatively attributed to defects resulting from the fabrication process such as excess resin left within the structure or other imperfection introduced within the alternating low-density and compact layers.

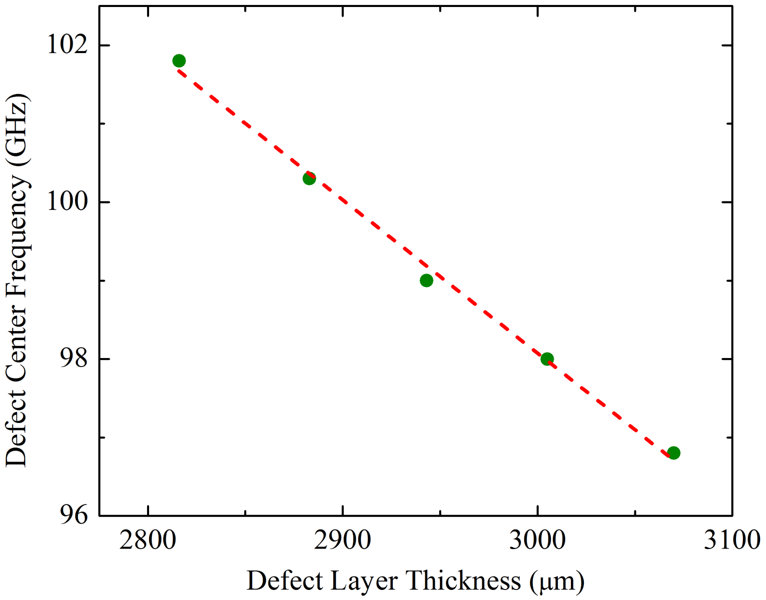

Figure 4.8: Center frequency of the defect modes as a function of defect layer thickness d_{defect} for the fabricated photonic crystal structures. Linear correlation between the center frequency and d_{defect} can be clearly observed. Analysis revealed that a 1 GHz shift is achieved with approximately 51 µm of adjustment in d_{defect}.

Figure 4.8 depicts the shift in defect mode center frequency as a function of defect layer thickness d_{defect}. The center frequency of defect modes was found to be linearly correlated with d_{defect}, where 1 GHz shift is achieved with approximately 51 µm of

d_{defect} adjustment. The tuning range of the narrow transmission band is limited primarily by the bandwidth of the photonic bandgap of the photonic crystal. For the photonic crystal investigated here a theoretical tuning range from 85 to 115 GHz can be achieved.

4.2.4 Summary and conclusion

Mechanical tuning of a defect mode in the form of a narrow transmission peak in a stereolithographically fabricated 1D photonic crystal was demonstrated. The 1D photonic crystal studied here is composed of two sets of alternating compact and low-density layer pairs enclosing a defect layer located in the middle of the structure. While the compact layers are fabricated entirely from polymethacrylate without any intentional internal structure, the low-density layers comprise arrays of sub-wavelength sized polymethacrylate columns oriented perpendicular to the layer interfaces. The THz optical response of the stereolithographically fabricated crystal was experimentally obtained using normal incidence transmission spectroscopy. The spectral responses of the samples have been measured in the spectral range from 82 to 125 GHz for 6 different values of the defect layer thickness d_{defect}. The model calculations and experimental data revealed that the fabricated structures are capable of creating a photonic bandgap as well as a photonic bandgap with a sharp defect mode within the bandgap by simple mechanical translation. The spectral position of the sharp defect mode was easily tuned by mechanically adjusting the defect layer thickness. Approximately 5 GHz shift in spectral position of the defect mode was experimentally demonstrated.

The THz transmission data were analyzed using optical layer model calculations. The dielectric function of the low-density layers was described using a Bruggeman effective medium approach, while the dielectric function of bulk polymethacrylate was directly used to represent the dielectric function of the compact layers. A good agreement was found between the experimental and best-model THz transmission data. The center frequency of defect modes was found to be linearly correlated with d_{defect}, where 1 GHz shift is achieved with approximately 51 µm of d_{defect} adjustment. Only slight deviations of the fabricated structure from the nominal geometry was identified from the analysis. A slight thickness non-uniformity in the defect layer due to unintentional misalignment of the samples was found to affect the maximum transmission amplitude achieved by the photonic crystal.

In conclusion, mechanical tuning of the defect modes formed by a twinning defect was demonstrated with a stereolithographically fabricated 1D photonic crystal for the first time. A linear correlation between the spectral position of the sharp defect mode and the void defect layer thickness was experimentally found. Our design suggests an innovative way to create and control defect modes in the THz spectral range.

REFERENCES

[1] A. D. Squires, E. Constable, and R. A. Lewis, “3d printed terahertz diffraction gratings and lenses,” *J. Infrared Millim. Terahertz Waves* **36**, 72 (2015).

[2] S. F. Busch, M. Weidenbach, J. C. Balzer, and M. Koch, “Thz optics 3d printed with topas,” *J. Infrared Millim. Terahertz Waves* **37**, 303 (2016).

[3] A. I. Hernandez-Serrano, M. Weidenbach, S. F. Busch, M. Koch, and E. Castro-Camus, “Fabrication of gradient-refractive-index lenses for terahertz applications by three-dimensional printing,” *J. Opt. Soc. Am. B* **33**, 928 (2016).

[4] A. Kaur, J. C. Myers, M. I. M. Ghazali, J. Byford, and P. Chahal, “Affordable terahertz components using 3d printing,” *2015 IEEE 65th Electronic Components and Technology Conference (ECTC)*, 2071 (2015).

[5] M. Ortiz-Martinez, E. Castro-Camus, and A. Hernandez-Serrano, “Guided-mode filters for terahertz frequencies fabricated by 3d printing,” *J. Infrared Millim. Terahertz Waves* **40**, 731 (2019).

[6] J. Yang, J. Zhao, C. Gong, H. Tian, L. Sun, P. Chen, L. Lin, and W. Liu, “3d printed low-loss thz waveguide based on kagome photonic crystal structure,” *Opt. Express* **24**, 22454 (2016).

[7] W. D. Furlan, V. Ferrando, J. A. Monsoriu, P. Zagrajek, E. Czerwińska, and M. Szustakowski, “3d printed diffractive terahertz lenses,” *Opt. Lett.* **41**, 1748 (2016).

[8] D. B. Fullager, S. Park, C. Hovis, Y. Li, J. Reese, E. Sharma, S. Lee,

C. Evans, G. D. Boreman, and T. Hofmann, “Metalized poly-methacrylate off-axis parabolic mirrors for terahertz imaging fabricated by additive manufacturing,” *J. Infrared Millim. Terahertz Waves* **40**, 269 (2019).

[9] S. Park, Y. Li, D. B. Fullager, S. Schöche, C. M. Herzinger, G. D. Boreman, and T. Hofmann, “Terahertz to mid-infrared dielectric properties of polymethacrylates for stereolithographic single layer assembly,” *J. Infrared Millim. Terahertz Waves* **40**, 971 (2019).

[10] T. D. Ngo, A. Kashani, G. Imbalzano, K. T. Q. Nguyen, and D. Hui, “Additive manufacturing (3d printing): A review of materials, methods, applications and challenges,” *Compos. B. Eng* **143**, 172 (2018).

[11] S. Park, Y. Li, B. Norton, M. McLamb, G. D. Boreman, and T. Hofmann, “One-dimensional photonic crystals fabricated using stereolithographic single layer assembly for the terahertz spectral range,” *J. Infrared Millim. Terahertz Waves* **41**, 542 (2020).

[12] E. Yablonovitch, “Inhibited spontaneous emission in solid-state physics and electronics,” *Phys. Rev. Lett.* **58**, 2059 (1987).

[13] J. D. Joannopoulos, P. R. Villeneuve, and S. Fan, “Photonic crystals,” *Solid State Commun.* **102**, 165 (1997).

[14] M. Honda, T. Seki, and Y. Takeoka, “Dual tuning of the photonic band-gap structure in soft photonic crystals,” *Adv. Mater.* **21**, 1801 (2009).

[15] B. Li, J. Zhou, L. Li, X. J. Wang, X. H. Liu, and J. Zi, “Ferroelectric inverse opals with electrically tunable photonic band gap,” *Appl. Phys. Lett.* **83**, 4704 (2003).

[16] J. Xia, Y. Ying, and S. H. Foulger, “Electric-field-induced rejection-wavelength tuning of photonic-bandgap composites,” *Adv. Mater.* **17**, 2463 (2005).

[17] H. Němec, L. Duvillaret, F. Garet, P. Kužel, P. Xavier, J. Richard, and D. Rauly, “Thermally tunable filter for terahertz range based on a one-dimensional photonic crystal with a defect,” *J. Appl. Phys.* **96**, 4072 (2004).

[18] R. Wilk, N. Vieweg, O. Kopschinski, and M. Koch, “Liquid crystal based electrically switchable bragg structure for thz waves,” *Opt. express* **17**, 7377 (2009).

[19] N. Vieweg, N. Born, I. Al-Naib, and M. Koch, “Electrically tunable terahertz notch filters,” *J. Infrared Millim. Terahertz Waves* **33**, 327 (2012).

[20] S. F. Busch, E. Castro-Camus, F. Beltran-Mejia, J. C. Balzer, and M. Koch, “3d printed prisms with tunable dispersion for the thz frequency range,” *J. Infrared Millim. Terahertz Waves* **39**, 553 (2018).

[21] Y. Li, Y. Xiang, S. Wen, J. Yong, and D. Fan, “Tunable terahertz-mirror and multi-channel terahertz-filter based on one-dimensional photonic crystals containing semiconductors,” *J. Appl. Phys.* **110**, 073111 (2011).

[22] W. Park and J.-B. Lee, “Mechanically tunable photonic crystal structure,” *Appl. Phys. Lett.* **85**, 4845 (2004).

[23] K. Sumioka, H. Kayashima, and T. Tsutsui, “Tuning the optical properties of inverse opal photonic crystals by deformation,” *Adv. Mater.* **14**, 1284 (2002).

[24] M. Kimura, K. Okahara, and T. Miyamoto, “Tunable multilayer-film distributed-bragg-reflector filter,” *J. Appl. Phys.* **50**, 1222 (1979).

[25] K. Yoshino, Y. Kawagishi, M. Ozaki, and A. Kose, “Mechanical tuning of the optical properties of plastic opal as a photonic crystal,” *Jpn. J. Appl. Phys.* **38**, L786 (1999).

[26] P. Zhu, W. Yang, R. Wang, S. Gao, B. Li, and Q. Li, "Direct writing of flexible barium titanate/polydimethylsiloxane 3d photonic crystals with mechanically tunable terahertz properties," *Adv. Opt. Mater.* **5**, 1600977 (2017).

[27] Y. Li, D. B. Fullager, S. Park, D. Childers, R. Fesperman, G. Boreman, and T. Hofmann, "High-contrast infrared polymer photonic crystals fabricated by direct laser writing," *Opt. Lett.* **43**, 4711 (2018).

[28] W. Cai and V. Shalaev, Optical metamaterials: fundamentals and applications, (Springer, New York, 2010).

[29] S. Park, Y. Li, D. Fullager, S. Schöche, C. Herzinger, S. Lee, and T. Hofmann, "Terahertz-frequency dielectric anisotropy in three-dimensional methacrylates fabricated by stereolithography," *Opt. Lett.* **45**, 1982 (2020).

[30] D. Turchinovich, A. Kammoun, P. Knobloch, T. Dobbertin, and M. Koch, "Flexible all-plastic mirrors for the thz range," *Appl. Phys. A* **74**, 291 (2002).

[31] N. Krumbholz, K. Gerlach, F. Rutz, M. Koch, R. Piesiewicz, T. Kürner, and D. Mittleman, "Omnidirectional terahertz mirrors: A key element for future terahertz communication systems," *Appl. Phys. Lett.* **88**, 202905 (2006).

[32] W. Withayachumnankul, B. M. Fischer, and D. Abbott, "Quarter-wavelength multilayer interference filter for terahertz waves," *Opt. Commun.* **281**, 2374 (2008).

[33] C. Jansen, S. Wietzke, V. Astley, D. M. Mittleman, and M. Koch, "Mechanically flexible polymeric compound one-dimensional photonic crystals for terahertz frequencies," *Appl. Phys. Lett.* **96**, 111108 (2010).

[34] E. Yablonovitch, T. Gmitter, R. Meade, A. Rappe, K. Brommer, and

J. Joannopoulos, “Donor and acceptor modes in photonic band structure,” *Phys. Rev. Lett.* **67**, 3380 (1991).

[35] H. Němec, L. Duvillaret, F. Quemeneur, and P. Kužel, “Defect modes caused by twinning in one-dimensional photonic crystals,” *J. Opt. Soc. Am. B* **21**, 548 (2004).

[36] H. Němec, P. Kužel, L. Duvillaret, A. Pashkin, M. Dressel, and M. Sebastian, “Highly tunable photonic crystal filter for the terahertz range,” *Opt. Lett.* **30**, 549 (2005).

[37] Y. Yu, J. Cai, J. Sun, Z. Zhang, and H. Qin, “Fabrication and characterization of a wide-bandgap and high-q terahertz distributed-bragg-reflector micro cavities,” *Opt. Commun.* **426**, 84 (2018).

[38] A. Ferraro, D. C. Zografopoulos, R. Caputo, and R. Beccherelli, “Periodical elements as low-cost building blocks for tunable terahertz filters,” *IEEE Photon. Technol. Lett.* **28**, 2459 (2016).

[39] S. Park, Y. Li, M. McLamb, B. Norton, G. D. Boreman, and T. Hofmann, “Highly localized defect mode in polymer-based thz photonic crystals fabricated using stereolithography,” *J. Infrared Millim. Terahertz Waves* **41**, 825 (2020).

[40] S. Park, B. Norton, G. D. Boreman, and T. Hofmann, “Mechanical tuning of the terahertz photonic bandgap of 3d-printed one-dimensional photonic crystals,” *J. Infrared Millim. Terahertz Waves* **42**, 1 (2020).

[41] Y.-H. Chang, Y.-Y. Jhu, and C.-J. Wu, “Temperature dependence of defect mode in a defective photonic crystal,” *Opt. Commun.* **285**, 1501 (2012).

CHAPTER 5: POLYMER-BASED THZ ANISOTROPIC METAMATERIAL FABRICATED USING STEREOLITHOGRAPHY

5.1 Terahertz-frequency dielectric anisotropy in three-dimensional polymethacrylates fabricated by stereolithography

The anisotropic optical dielectric functions of slanted columnar layers fabricated using stereolithography from polymethacrylates are reported for the terahertz-frequency domain using generalized spectroscopic ellipsometry.[1] The slanted columnar layers are composed of spatially coherent columnar structures with a diameter of 100 µm and a length of 700 µm that are tilted by 45° with respect to the surface normal of the substrates. A simple biaxial (orthorhombic) layer homogenization approach is used to analyze the terahertz ellipsometric data obtained at three different sample azimuthal orientations. The permittivity along the major polarizability directions varies by almost 25%. Our results demonstrate that stereolithography allows tailoring of the polarizability and anisotropy of the host material, and provides a flexible alternative metamaterials fabrication method for the terahertz spectral range.

5.1.1 Introduction

Metamaterials have attracted continued interest for almost two decades due to their unique electromagnetic properties, which can differ substantially from their constituents and often do not exist in naturally occurring materials [1, 2, 3]. Commonly used lithographic fabrication techniques such as optical, electron-beam, femtosecond laser, or nanoimprint lithography, have been used to form metamaterials with

---

[1] S. Park, Y. Li, D. B. Fullager, S. Schöche, C. M. Herzinger, S. Lee, and T. Hofmann, "Terahertz-frequency dielectric anisotropy in three-dimensional polymethacrylates fabricated by stereolithography," *Opt. Lett.* **45**, 1982-1985 (2020). Reprinted with permission © The Optical Society.

sub-wavelength feature sizes [4]. Lithographic techniques, however, typically require expensive equipment, complicated processing steps, and long production time that limit the classes of metamaterials that can be practically fabricated with these approaches [4]. More recently two-photon polymerization and micro-stereolithography have been used to fabricate very complex three-dimensional (3D) architectures with nano- and microscale resolutions, respectively [5, 6, 7, 8]. So far, these layer-by-layer additive fabrication techniques have been applied for the synthesis of metamaterials with virtually arbitrary 3D architectures designed to operate in the infrared and visible spectral range [9, 10, 11].

For the terahertz (THz) spectral range, the spatial resolution needed for sub-wavelength metamaterial building blocks is in the range of several µm. Stereolithography with micro and nanometer resolution might therefore offer a readily accessible fabrication approach. So far stereolithography has been used to fabricate waveguide components, phase shifters, band pass filters and wave absorbers for the spectral range from 10 GHz to 1 THz [12, 13, 14].

Stereolithography or hybrid techniques in which the photopolymers, have been recognized as paradigm shifting techniques for the realization of tunable THz devices, however, investigation of tunable THz metamaterials only have been demonstrated using photolithography or micromachining and have not been reported for additive manufacturing techniques [15, 16, 12] In particular, structures that exhibit form-induced birefringence as well as approaches for accurate experimental measurement and analysis of the anisotropic optical properties have not been investigated so far.

In this letter we report on the anisotropic optical properties of 3D metamaterials composed of polymethacrylate slanted columnar structures fabricated using stereolithography. THz generalized spectroscopic ellipsometry has been demonstrated as a versatile technique for the characterization of anisotropic sculptured thin films [17, 18, 19, 20], and is employed here to accurately measure the THz optical response of fabricated structures. A simple homogenization approach is found to be sufficient to describe the THz biaxial behavior of the investigated structures.

5.1.2 Experiment

5.1.2.1 Design and fabrication

We have investigated two samples fabricated in a single fabrication step using a commercially available stereolithography system (Form 2, Formlabs, Inc.). The stereolithography system has a nominal layer resolution of 25 µm and in the direction orthogonal to the polymerization plane and the nominal laser spot size of 140 µm [21]. One sample is a bare, homogeneous polymethacrylate substrate with a nominal thickness of 3 mm and plane parallel interfaces. This sample served as a reference to determine the THz dielectric properties of bulk-like polymethacrylate and is based on a model dielectric function for polymethacrylates developed earlier [22]. The second sample is composed of a 500 µm thick slanted columnar polymethacrylate layer fabricated on top of a homogeneous polymethacrylate substrate with a nominal thickness of 1 mm. The diameter and spacing of the slanted columns are designed to be 100 µm and 200 µm, respectively. The slanting angle of the columnar structures

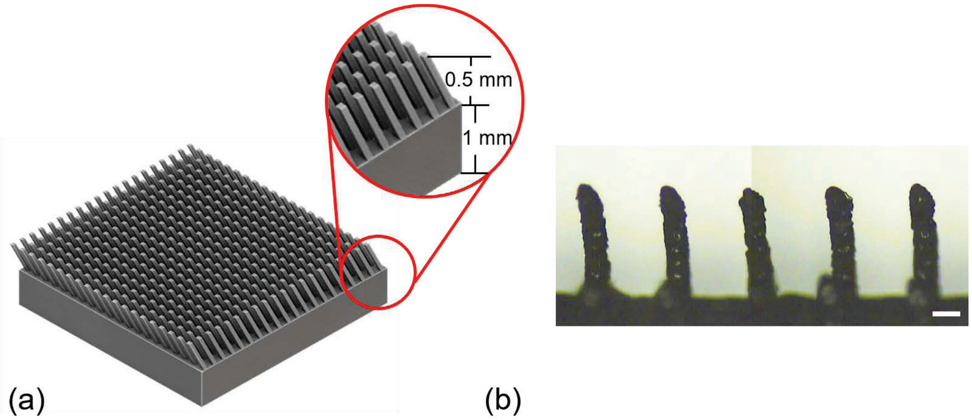

Figure 5.1: (a) A tilted top view image of the CAD rendering depicting the nominal geometry of the slanted columnar structures and substrate. The columnar structures have a diameter of 100 µm and are tilted by 45° with respect to the substrate normal. The spacing between the columns is 200 µm. (b) A tilted cross-sectional optical micrograph depicting the slanted columnar structures of the fabricated sample. The scale bar is 100 µm.

is 45° with respect to the substrate surface normal. Thus, the columnar structures have nominal length of approximately 700 µm. A CAD rendering of the sample with the slanted columnar film is provided in Fig. 5.1 (a), where a 6×6 mm^2 area of the sample is shown. The fabricated substrate area, which is identical for both samples, is 30×30 mm^2 in order to ensure that a sufficient signal-to-noise ratio was obtained with the THz ellipsometer used to acquire the experimental Mueller matrix data as described further below.

Following the photopolymerization, the samples were rinsed then sonicated in isopropyl alcohol for 10 min to remove any unpolymerized material. The nominal diameter of the fabricated columnar structures is approximately 28% smaller than the nominal laser spot size of the stereolithography system. It was experimentally determined that critical features substantially smaller than the nominal laser spot size can be achieved with the employed stereolithography system. Figure 5.1 (b) depicts a tilted cross-sectional optical micrograph obtained with the optical axis of the ×10 objective parallel to the slanting plane of the columnar structures. Therefore, the columnar structures appear to be normal to the substrate in the optical micrograph. The optical micrograph clearly shows that the diameter of the fabricated columnar structures is in excellent agreement with its nominal value of 100 µm. The spacing of the columns is also in very good agreement with the nominal value of 200 µm.

It can also be noted that surface roughness values of polymethacrylate samples fabricated with the employed stereolithography system are well below the nominal instrument resolution. The arithmetic mean deviation R_a and root mean squared deviation R_q were found to be 4 µm and 5 µm, respectively, for a stereolithographically fabricated THz optical component [23]. Therefore, the surface roughness induced by the stereolithographic fabrication process imposes only insignificant effects on the performance of optical components operating at THz frequencies. Consequently, surface roughness effects are neglected in the stratified optical layer model calculations used here to analyze the experimental Mueller matrix spectra.

5.1.2.2 Data Acquisition and Analysis

Generalized spectroscopic ellipsometry measurements were carried out in the spectral range from 210 to 350 GHz with a resolution of 2.5 GHz. A commercial frequency-domain THz ellipsometer (THz-VASE, J.A. Woollam, Co., Inc.) operating in a polarizer-sample-rotating compensator-analyzer configuration was used here. This instrument is capable of measuring 12 out of the 16 real-valued Mueller matrix elements M_{ij}, which connect the Stokes parameters before and after sample interaction [24]. The elements in the 4th column are inaccessible with this instrument due to the lack of a source side compensator [25]. Note that the M_{ij} values reported here are normalized with respect to M_{11}.

Experimental THz Mueller matrix spectra were obtained from the isotropic reference substrate at two angles of incidence $\Phi_a = 50^\circ$ and 70°, and analyzed to determine the dielectric function of bulk-like polymethacrylate. The dielectric functions of polymethacrylate used here is discussed in detail in Ref. [22].The slanted columnar sample was also investigated using THz-GSE at two different angles of incidence $\Phi_a = 50^\circ$ and 70°, and three different in-plane sample orientations φ. For the recorded in-plane orientations $\varphi = 0^\circ,\ 45^\circ$, and 90°, the columnar slanting plane is oriented perpendicular, oblique (45°), and parallel to the plane of incidence, respectively.

All obtained experimental ellipsometric data sets were analyzed using stratified layer model calculations obtained by a commercial software package (WVASE32$^{\mathrm{TM}}$, J.A. Woollam Company) [26, 27]. The employed optical model for the slanted columnar layer sample consists of four layers including air/homogeneous biaxial layer/polymethacrylate substrate/air. For the polymethacrylate substrate reference sample, a three layer model composed of air/polymethacrylate substrate/air was used.

A parameterized model dielectric function was used to describe the THz optical response of the bulk polymethacrylate. The employed model dielectric function is based on the dielectric function reported previously for a number of polymethacrylates compatible with the stereolithographic fabrication process [22, 28]. The dielectric function is composed of 15 oscillators with Gaussian broadening and accurately renders the THz and infrared optical response [22]. This model dielectric function was determined for a spectral range from 0.65 to 120 THz with a gap between 0.95 to 9 THz. The extension of the model dielectric function to the spectral range reported here required only minimal changes to ε_∞ and amplitude A of the lowest oscillator (see Eqn. (1) and Tab. 2 of Ref. [22]).

A homogeneous biaxial layer approach was employed to describe the optical response of the slanted columnar layer. This homogenization approach was first introduced for the analysis of Mueller matrix data obtained from columnar thin films in the visible spectral range [29, 30]. The films reported in Ref. [30] were composed of semi-transparent slanted columnar structures fabricated using glancing angle of incidence deposition. Schmidt *et al.* found that the optical response of these columnar thin films can be accurately described as an effective medium with biaxial properties [30]. The effective dielectric function tensor consisted of three components ε_a, ε_b, and ε_c oriented along the major polarizability directions $\vec{a}$, $\vec{b}$, and $\vec{c}$ of a monoclinic system, which was aligned with the slanted columnar geometry. $\vec{b}$ and $\vec{c}$ were oriented orthogonal and parallel to the columnar structure axis, respectively. The angle between axes $\vec{a}$ and $\vec{c}$ was given by the monoclinic angle β which was found to be 74.8°. Here an orthorhombic homogeneous biaxial model was used to describe the THz optical response of the polymethacrylate slanted columnar layer. The three major polarizability directions are orthogonal to each other, where $\vec{b}$ and $\vec{c}$ are oriented orthogonal and parallel to the columnar structure axis, respectively.

Nonlinear least squares methods were used to vary significant physical model parameters (slanted columnar layer thickness, substrate thickness, ε_∞, and A) until all model calculated data sets were matched simultaneously to the experimental data sets (best-model) [31].

5.1.3 Results and discussion

Figures 5.2 and 5.3 show experimental and best-model calculated Mueller matrix data obtained for the homogeneous reference substrate and the slanted columnar sample, respectively. A good agreement between the best-model calculated and the experimental data was found for both samples. For the homogeneous reference substrate only the non-trivial Mueller matrix data are shown here at an angle of incidence of $\Phi_a = 70°$ for clarity. The Mueller matrix spectra show distinct Fabry-Pérot interference patterns caused by the transparent substrate with a thickness of $d = (2.91 \pm 2)$ mm. The oscillation amplitude gradually dampens as the frequency increases, which is attributed to a broad, optically active vibrational mode with a resonance frequency outside of the investigated spectral range. The off-diagonal block Mueller matrix elements (M_{13}, M_{23}, M_{31}, M_{32}, M_{41}, and M_{42}; not shown here for brevity) are all within a range of ±0.03 as anticipated for an isotropic sample re-

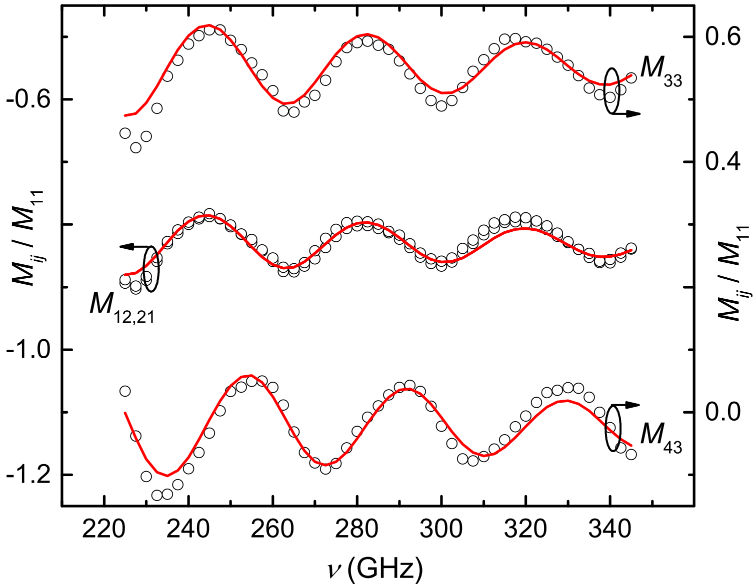

Figure 5.2: Experimental (symbols) and best-model calculated (solid lines) Mueller matrix spectra of the isotropic reference substrate. Note only the non-trivial Mueller matrix elements M_{12}, M_{21}, M_{33}, and M_{43} obtained at $\Phi_a = 70°$ are depicted for brevity.

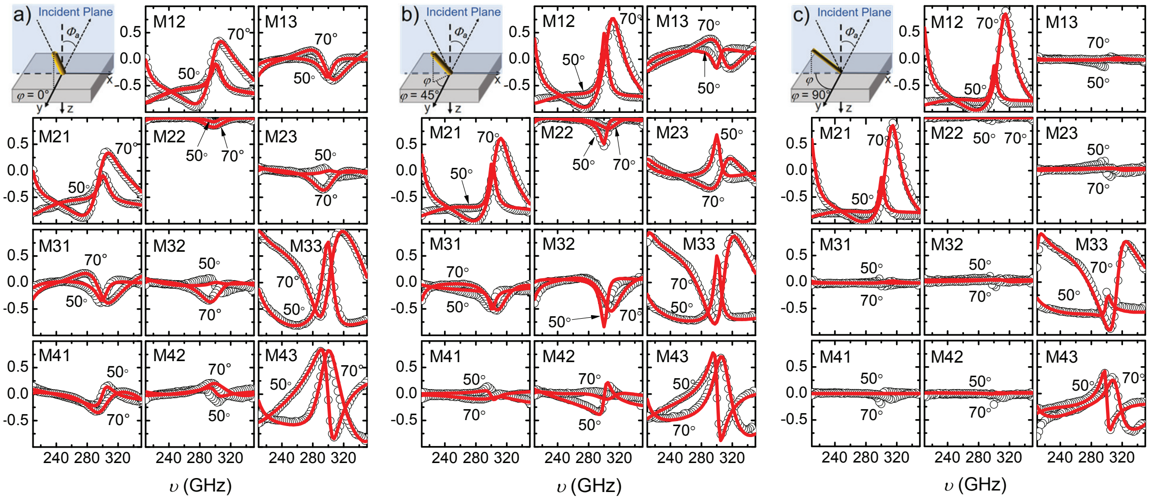

Figure 5.3: Experimental (symbols) and best-model calculated (solid lines) Mueller matrix spectra of the slanted columnar layer sample for three different in-plane orientations φ and two angles of incidence $\Phi_a = 50°$ and $70°$. Data for $\varphi = 0°$, $45°$ and $90°$ is shown in panels a), b), and c), respectively. The insets illustrate orientation of the slanting plane with respect to the plane of incidence.

sponse. Figure 5.4 c) depicts the best-model dielectric function of bulk-like polymethacrylate exhibiting slight absorption and very low dispersion as expected from comparison with THz measurements of other polymers [32].

Figure 5.3 depicts the experimental and best-model calculated THz Mueller matrix data for three different in-plane rotations $\varphi = 0°$, $45°$, and $90°$ at two angles of incidence $\Phi_a = 50°$ and $70°$ in panels a), b), and c), respectively. The best-fit parameters obtained from the data analysis were 399 ± 5 µm, 990 ± 2 µm for slanted columnar layer thickness and substrate thickness, and 2.2 ± 0.1 and 0.21 ± 0.01 for ε_∞ and A, respectively. The spectra are dominated by a sharp resonance at approximately 290 GHz due to a Fabry-Pérot interference originating from the substrate and the slanted columnar layer. The position of the Fabry-Pérot resonance is determined by the thickness of the substrate and the slanted columnar layer and varies with Φ_a. The highly anisotropic THz optical response due to the form-induced birefringence in the slanted columnar layer sample is evident in the non-zero off-diagonal block elements

(M_{13}, M_{23}, M_{31}, M_{32}, M_{41}, and M_{42}) for $\varphi = 0°$ and 45°. For $\varphi = 90°$, where the plane of incidence is parallel to the slanting plane, the off-diagonal block element values are vanishing. The largest values for $M_{31,13}$ and $M_{32,23}$ are on the order of ±0.5 while M_{41} and M_{42} are slightly smaller. Considering the Mueller matrix values being defined between 1 and −1, the slanted columnar layer exhibits a strong anisotropic THz response.

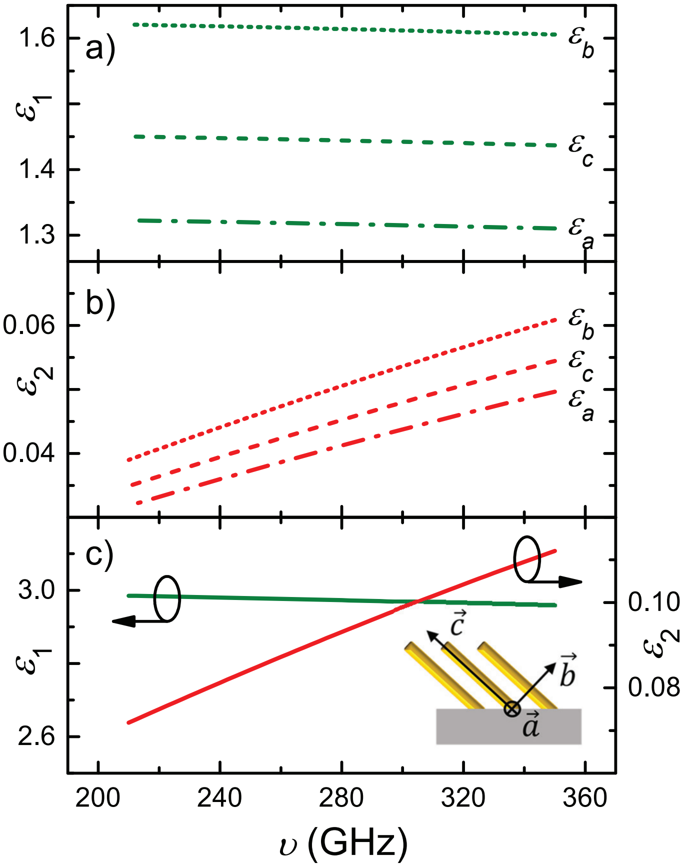

Figure 5.4: The real and imaginary part of the biaxial (orthorhombic, see inset) dielectric function ε_a, ε_b, ε_c obtained from the best-model calculation for the polymethacrylate slanted columnar layer are shown in panel a) and b), respectively. The isotropic dielectric function for the bulk-like polymethacrylate obtained from the reference substrate is shown for comparison in panel c).

The real and imaginary parts of the dielectric function of the slanted columnar layer along the major polarizability directions $\vec{a}$, $\vec{b}$, and $\vec{c}$ are illustrated in Fig. 5.4 a) and b), respectively. The isotropic dielectric function of the bulk-like polymethacrylate is shown for comparison (Fig. 5.4 c)). The optical properties of the slanted columnar layer exhibit a strong birefringence as well as dichroism over the entire investigated THz spectral range. The permittivity is found to be the largest along the direction perpendicular with the columns (ε_b), while the difference between the polarizability along $\vec{a}$ and $\vec{b}$ is approximately 25 %. The dichroism is small and follows the same trend as the birefringence. The experimental results substantiate the capability of polymethacrylate based stereolithography to create THz metamaterials with desired optical properties.

5.1.4 Summary and conclusion

In conclusion, stereolithography is presented as a versatile technique for the fabrication of the THz metamaterials. A stereolithographically fabricated structure composed of slanted polymethacrylate wires 100 µm in diameter and approximately 700 µm long was investigated. THz generalized ellipsometry measurements were performed to analyze the influence of form-induced birefringence on the bulk-like optical properties of polymethacrylate. A strong anisotropic response was detected from the slanted columnar layer structure, while the bulk-like response was found to be isotropic. We employed a simple homogenization approach, that successfully rendered the optical properties of the anisotropic sample. A strong birefringence as well as dichroism were observed in the ellipsometric data. Our results demonstrate that stereolithography is an effective way of fabricating THz metamaterials with tailored polarizability and anisotropy as well as virtually any arbitrary architecture. Maskless 3D photopolymerization is envisioned as a versatile technique for creating THz optical components with designed anisotropy for various applications, such as polarimetric detection.

5.2 Terahertz Anisotropic Response of Additively Manufactured One-Dimensional Photonic Crystals

A polymer-based, one-dimensional photonic crystal exhibiting anisotropic responses was demonstrated in the terahertz frequency range.[2] The photonic crystal was composed of alternating compact and low-density polymethacrylate layers. The low-density layers consist of sub-wavelength sized columns, which were slanted 45° with respect to the substrate surface normal to achieve form-birefringence. Normal incidence polarized terahertz transmission measurements were carried out for the characterization of the fabricated photonic crystals in the range from 82 to 125 GHz. The experimental data revealed a 2 GHz shift in the center frequency of the photonic bandgap as a function of in-plane orientation, well demonstrating the anisotropic behaviour of the fabricated crystal. The transmission data were analyzed using stratified optical layer model calculations. A good agreement was found between the relevant model parameters and the corresponding design parameters.

5.2.1 Introduction

Anisotropic materials are ubiquitous for traditional optical elements such as polarizers and wave plates [33, 34], and are essential to realize novel optical components including optical cloaking devices and hyperlenses [35, 36]. While optical anisotropy occurs in natural materials such as calcite [37], the performance of optical elements fabricated using such materials is limited by the materials' inherent anisotropic properties [38, 39]. Metamaterials, on the other hand, enable flexible tailoring of the anisotropic properties that can not be achieved with naturally occurring materials [40, 41, 42]. Metamaterials for visible and infrared spectral ranges have been continually studied, primarily using lithographic fabrication techniques includ-

---

[2] S. Park, V. P. Stinson, G. D. Boreman, and T. Hofmann, "Terahertz anisotropic response of additively manufactured one-dimensional photonic crystals," *Opt. Lett.* **46**, 3396-3399 (2021). Reprinted with permission © The Optical Society.

ing electron-beam lithography and nanoimprint lithography [43].

More recently, additive manufacturing methods including two-photon polymerization and stereolithography have been introduced as promising techniques for the fabrication of metamaterials operating in the infrared or larger wavelength ranges [44, 11]. Additive manufacturing techniques enable rapid and cost-effective synthesis of three-dimensional structures with virtually arbitrary geometries, allowing metamaterials to achieve optimal performance [45]. Especially in the terahertz (THz) frequency range, the spatial resolution needed for sub-wavelength metamaterial building blocks is in the range of several hundred µm; which is easily obtainable through current state-of-the-art commercial stereolithography systems [46]. Stereolithography provides superior spatial resolution compared to other common three-dimensional printing techniques and it has been recognized as a reliable method of fabricating THz optical components including reflectors and absorbers [23, 14].

One-dimensional (1D) photonic crystal structures for THz spectral range have been demonstrated using single-step, polymer-based stereolithography [47, 48, 49]. Photonic crystals, consisting of periodically arranged sub-wavelength scale constituents, form photonic bandgaps in which the propagation of electromagnetic radiation is prohibited [50]. The characteristics of photonic bandgaps such as spectral width and position are determined based on the unit cell of the crystal [51]. Non-cubic unit cells have been reported to induce anisotropic optical effects [52, 53].

1D photonic crystals have been consistently studied over the years due to their versatile usage in optical applications including optical filters and phase modulators [53, 54]. It is often desirable to have added tunability in order to adjust the spectral position of the photonic bandgap formed by photonic crystals. Obtaining such tunability with 1D photonic crystals can be realized by utilizing external stimuli such as mechanical forces and electrical signals [48, 55]. Another way of achieving tunable photonic bandgaps is employing anisotropic materials as constituents of the photonic crystal structures [56]. 1D photonic crystals constructed using anisotropic materials form polarization-sensitive photonic bandgaps without requiring application of external stimuli [52]. Anisotropic photonic crystals have been studied over a wide electromagnetic spectrum [57, 58]. However, examples of anisotropic photonic crystals are relatively scarce for the THz spectral range [59].

We have recently reported stereolithographically fabricated metamaterials consisting of sub-wavelength sized slanted columnar structures and their anisotropic optical properties in the THz spectral range [60]. The successful demonstrations of stereolithographically fabricated THz 1D photonic crystals and anisotropic metamaterials suggest that THz anisotropic metamaterials can be conveniently integrated into 1D photonic crystals through stereolithography to obtain a polarization-sensitive photonic bandgap.

In this letter we report on all-dielectric 1D photonic crystal that exhibits anisotropic optical responses in THz frequency range. Sub-wavelength sized slanted columnar structures have been integrated into 1D photonic crystal using stereolithography to achieve a polarization-sensitive photonic bandgap, allowing detection using simple THz polarized transmission measurements.

5.2.2 Experiment

5.2.2.1 Design and fabrication

The 1D photonic crystals studied here consist of 13 alternating compact and low-density layers that are 1300 µm and 1800 µm thick, respectively. The compact layers are homogeneous polymethacrylate with plane-parallel interfaces. The low-density layers are composed of sub-wavelength scale columnar structures. The columnar structures with a square cross section and a side length of 220 µm are slanted at 45° relative to the layer interfaces and are arranged in a square lattice pattern with spacing of 1 mm. The arrangement of the columnar structures with respect to the compact layers is illustrated in the inset of Fig. 5.5, in which the dimensions of

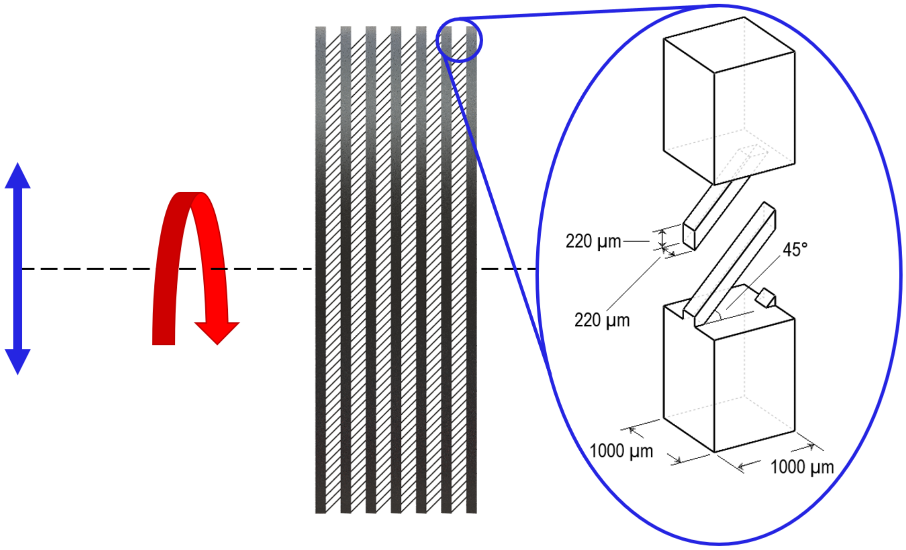

Figure 5.5: A side view schematic of the photonic crystal composed of 13 alternating compact and low-density layers. The direction of the polarization is indicated by the blue double-headed arrow, while the sample rotation is depicted as a red arrow. The low-density layers are composed of columnar structures oriented at 45° with respect to the layer interfaces and arranged in square lattice pattern as shown in the inset. The slanting plane is perpendicular to the interface of the layers.

these columnar structures are provided. Due to the slanted columnar structures, the low-density layers exhibit form-birefringence similar to that reported in Ref. [60, 30] and the optical properties of the photonic crystal depends on the polarization of the incident radiation.

The photonic crystal was fabricated in a single fabrication step using a commercial stereolithography system (Form 2, Formlabs, Inc.) with a polymethacrylate (black V4, Formlabs, Inc.) compatible with the system. Once the printing was completed, the sample was immersed in isopropyl alcohol for 10 min. It was then rinsed thoroughly with isopropyl alcohol for an additional 10 min and was dried using compressed air to ensure any remaining un-polymerized material was removed from the sample.

5.2.2.2 Data Acquisition and Analysis

Normal incidence polarized THz transmission spectroscopy was carried out for the characterization of the fabricated photonic crystals. An electronic synthesizer

(Synthesizer, Virginia Diodes Inc.) and an extension module (WR9.0SGX, Virginia Diodes Inc.) were used jointly as a source to produce linear, p-polarized radiation, which was collimated using a lens with 60 mm focal length. The collimated radiation was then transmitted through the sample and was focused using a second 60 mm focal length lens, and detected by a broadband power meter (PM5, Virginia Diodes Inc.). THz transmission spectra ranging from 82 to 125 GHz with 0.1 GHz resolution at three different in-plane sample orientations $\varphi = 0^\circ$, 45°, and 90° were obtained. Then another set of THz transmission spectra, ranging from 100 to 120 GHz, were measured as a function of φ ranging from 0° to 355° in 5° increments. The in-plane orientation φ in this experiment was defined as the angle between the slanting plane of the columns and the polarization direction of the incoming beam, i.e. $\varphi = 0^\circ$ when the slanting plane of the columns is parallel to the polarization direction of the incoming beam. The polarization direction of source radiation, axis of rotation, and direction of rotation of the sample are illustrated in Fig. 5.5 as a blue double headed arrow, dashed line, and a red arrow, respectively.

A subset of THz experimental transmission data were analyzed using stratified layer model calculations using a commercial software package (WVASE32$^{\mathrm{TM}}$, J.A. Woollam Company). The analysed data were transmission spectra ranging from 82 to 125 GHz at three different in-plane sample orientations ($\varphi = 0^\circ$, 45°, and 90°) and transmission measurements at two fixed frequencies (105 GHz and 115 GHz) as a function of φ from 0° to 355°. Levenberg-Marquardt-based algorithms were employed in this analysis to vary significant physical model parameters until all model calculated data and experimental data were best matched (best-model) [31]. The optical model used in the analysis consists of 7 compact layers and 6 low-density layers alternating in an air ambient, where the thicknesses of the compact layers and the low-density layers are denoted as d_{c} and d_{l}, respectively. The dielectric function of the compact layers is denoted by $\varepsilon_{\mathrm{com}}$ and was determined using infrared and THz spectroscopic ellipsometry as reported in Refs. [22, 28].

5.2.3 Results and discussion

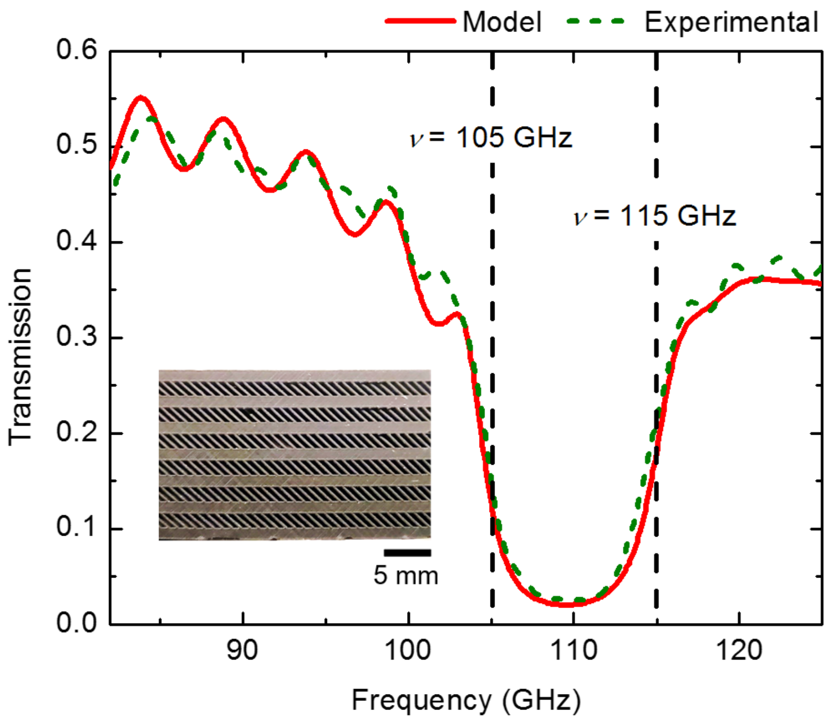

Figure 5.6: Experimental (green dashed line) and best-model calculated (red solid line) transmission spectra of the photonic crystal in the spectral range from 82 to 125 GHz for an in-plane orientation $\phi = 0°$. A cross-sectional optical image of a photonic crystal with identical dimensions is shown as an inset. The photonic bandgap centered around 109 GHz can be noticed. Black vertical dashed lines indicate the fixed frequencies (105 GHz and 115 GHz) where transmission data are separately reported.

The dielectric function of the low-density layers is described using a homogeneous biaxial layer approach, which was successfully used to render the anisotropic optical response of thin films composed of slanted columnar structures in the visible spectral range [29, 30]. Schmidt *et al.* demonstrated that a slanted columnar thin film can be described as a homogeneous medium whose biaxially anisotropic optical properties are well represented by a spatially constant dielectric function tensor [61]. Recently, we have applied this homogeneous biaxial layer approach to describe the biaxial response of additively manufactured, polymethacrylate-based metamaterials consisting of slanted columnar structures [60]. This optical model successfully rendered the THz generalized spectroscopic ellipsometry response obtained for a slanted columnar layer on top of a substrate layer, both fabricated using stereolithography.

Here, the low-density layers of the photonic crystals are composed of slanted columnar structures and are therefore analyzed using a biaxial, orthorhombic dielectric function tensor as previously demonstrated [60]. This tensor is described using three major components ε_a, ε_b, and ε_c along the major axes $\vec{a}$, $\vec{b}$, and $\vec{c}$ of an orthorhombic system as depicted in the inset of Fig. 5.8. The major polarizability axes are aligned with the slanted columns, where $\vec{a}$ is oriented perpendicular to the slanting plane and $\vec{b}$ and $\vec{c}$ are oriented perpendicular and parallel to the column axis, respectively. In order to avoid parameter correlation during the optical model analysis of the normal incidence transmission data, it was assumed that one of the major components of the dielectric function tensor ε_a is proportional to the value reported in Ref. [60]. It was also assumed that the dielectric function and layer thickness of the compact and low-density layers is constant throughout the photonic crystal. Therefore, the corresponding parameters of the optical model, d_{c}, d_{l}, ε_a, ε_b, ε_c, and $\varepsilon_{\mathrm{com}}$ were varied for all layers simultaneously.

Fig. 5.6 shows experimental and best-model calculated THz transmission data obtained for the spectral range from 82 to 125 GHz with 0.1 GHz resolution. The measurements and analysis were carried out for three different in-plane sample orientations $\varphi = 0°$, $45°$, and $90°$. A good agreement between the best-model calculated and the experimental data can be observed for all transmission spectra. Note that the data for $\varphi = 0°$ only are shown in Fig. 5.6. The photonic bandgap centered around 109 GHz can be noticed for $\varphi = 0°$ data, where the slanting plane of the columns is parallel to the incident polarization direction.

Fig. 5.7 depicts experimental polarized transmission data of the photonic crystal as a function of the in-plane orientation φ as a grey-scale contour plot. The experimental transmission data in the spectral range from 100 to 120 GHz with 0.1 GHz resolution

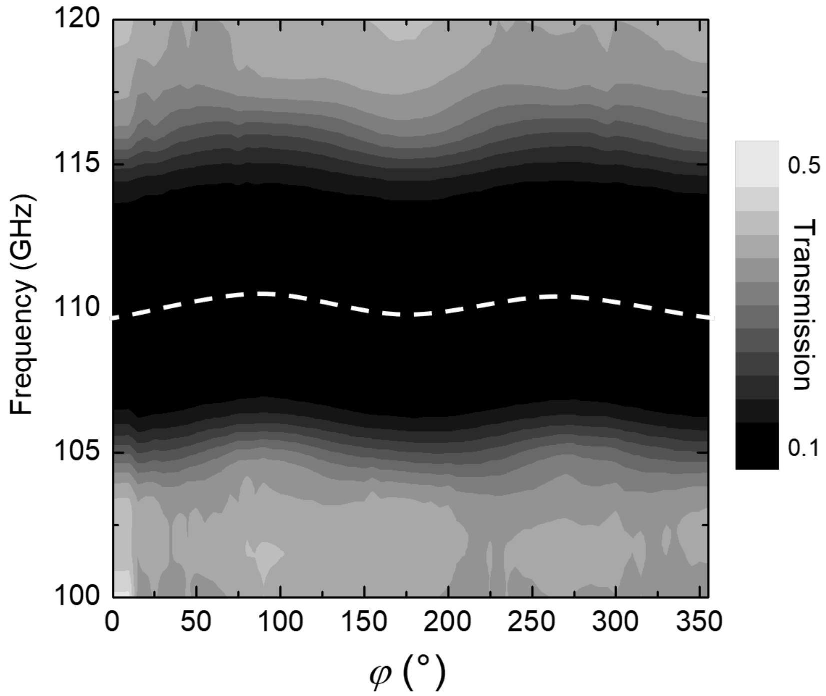

Figure 5.7: A grey-scale contour plot illustrating the experimental polarized transmission data of the photonic crystal in the spectral range from 100 to 120 GHz with 0.1 GHz resolution and in-plane orientation φ from 0° to 355° in 5° increments. The photonic bandgap can be easily identified, at the darkest area of the plot where over 90% of transmission is suppressed. The bandgap center frequency at each φ position, traced with a white dashed line, clearly indicates the shift in the center frequency due to sample rotation.

and φ from 0° to 355° with 5° increments are shown. At a first glance, the photonic bandgap, in which the most transmission is suppressed, can be easily identified as the darkest area of the plot. At the flanks of the photonic bandgap, in the vicinity of ν =105 GHz and 115 GHz, a periodic intensity variation can be clearly observed. The white dashed line in Fig. 5.7 traces the center frequency of the bandgap at each φ position along this periodic variation. This reveals a center frequency shift from approximately 109 GHz when the optical axis and the incident polarization direction are parallel to each other ($\varphi = 0°$, 180°) to 111 GHz when the optical axis and the incident polarization direction are perpendicular to one another ($\varphi = 90°$, 270°). The shift in the spectral position of the photonic bandgap is due to the anisotropic optical response of the photonic crystal.

Transmission data at two fixed frequencies (105 GHz and 115 GHz, indicated by vertical dashed lines in Fig. 5.6) as a function of the in-plane orientation angle are shown separately in Fig. 5.8 to illustrate this intensity variation at the bandgap flanks in further detail. A periodic intensity variation can be noticed, with distinct minima and maxima occurring at positions where the optical axis is parallel ($\varphi = 0°$, $180°$) or perpendicular ($\varphi = 90°$, $270°$) to the incident polarization direction. The transmitted intensity varies up to 25% at ν =105 GHz and 37% at ν =115 GHz when the optical axis is parallel or perpendicular to the incident polarization direction. A good agreement between the experimental (green dashed lines) and the model calculated (red solid lines) can be observed.

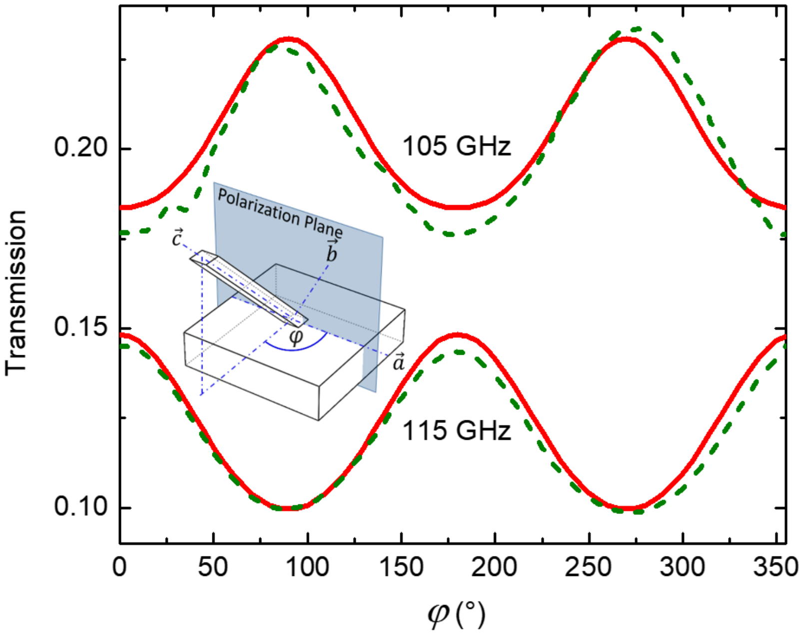

Figure 5.8: Experimental (green dashed lines) and best-model calculated (red solid lines) transmission data at 105 GHz and 115 GHz as a function of in-plane orientation φ from 0° to 355° in 5° increments. The inset illustrates the major axes $\vec{a}$, $\vec{b}$, and $\vec{c}$ of an orthorhombic system formed by the slanted columns in the low-density layers.

The best-fit parameters obtained from the data analysis were d_c = 1411±3 µm, d_l = 1642±3 µm for the layer thicknesses. The permittivity is found to be the largest in the direction along the columnar structures $\vec{c}$ (ε_c) and the smallest along $\vec{b}$ (ε_b). The real and imaginary parts of the dielectric function of the low-density layers along the major polarizability directions $\vec{a}$, $\vec{b}$, and $\vec{c}$ are illustrated in Fig. 5.9, which reveals a distinct birefringence and dichroism of the low-density layers.

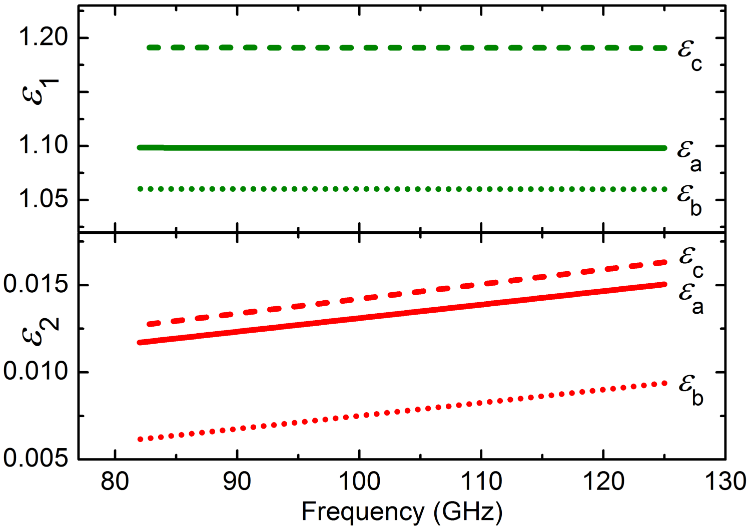

Figure 5.9: Real (ε_1, top) and imaginary (ε_2, bottom) parts of the biaxial dielectric function tensor ε_a, ε_b, and ε_c obtained from the best-model calculation for the anisotropic photonic crystal are shown. The permittivity was found to be the largest in the direction along the columnar axis (ε_c) and the smallest in the direction perpendicular to the columnar axis (ε_b).

5.2.4 Summary and conclusion

In conclusion, THz photonic bandgap shift due to anisotropy was demonstrated with a polymer based, 1D anisotropic photonic crystal fabricated using stereolithography. The photonic crystal composed of alternating compact and biaxial low-density layers. While the compact layers have no intentional internal structures, the low-density layers consist of sub-wavelength sized columnar structures that are slanted at 45° with respect to the layer interfaces. Simple, normal incidence polarized THz transmission measurements were able to reveal the anisotropic optical response of the fabricated photonic crystal. A distinct shift in the center frequency of the photonic bandgap was observed as a function of varying in-plane orientation of the sample. A stratified optical model was used to analyze the THz transmission data. A simple homogenization approach was employed here to render the biaxial properties of the low-density layers in the stratified optical model. A good agreement between the experimental and best-fit model data was found. Our results demonstrate that all-dielectric THz metamaterials with tailored anisotropic properties can be readily implemented in optical components through stereolithography.

REFERENCES

[1] R. A. Shelby, D. R. Smith, and S. Schultz, “Experimental verification of a negative index of refraction,” *Science* **292**, 77 (2001).

[2] J. B. Pendry and D. R. Smith, “Reversing light with negative refraction,” *Phys. today* **57**, 37 (2004).

[3] X. Zhao, Y. Wang, J. Schalch, G. Duan, K. Cremin, J. Zhang, C. Chen, R. D. Averitt, and X. Zhang, “Optically modulated ultra-broadband all-silicon metamaterial terahertz absorbers,” *ACS Photonics* **6**, 830 (2019).

[4] M. Mao, J. He, X. Li, B. Zhang, Q. Lei, Y. Liu, and D. Li, “The emerging frontiers and applications of high-resolution 3d printing,” *Micromachines* **8**, 113 (2017).

[5] S. Kawata, H.-B. Sun, T. Tanaka, and K. Takada, “Finer features for functional microdevices,” *Nature* **412**, 697 (2001).

[6] M. Farsari and B. N. Chichkov, “Two-photon fabrication,” *Nat. photonics* **3**, 450 (2009).

[7] X. Zheng, J. Deotte, M. P. Alonso, G. R. Farquar, T. H. Weisgraber, S. Gemberling, H. Lee, N. Fang, and C. M. Spadaccini, “Design and optimization of a light-emitting diode projection micro-stereolithography three-dimensional manufacturing system,” *Rev. Sci. Instrum.* **83**, 125001 (2012).

[8] Y. Li, D. Fullager, E. Angelbello, D. Childers, G. Boreman, and T. Hofmann,

"Broadband near-infrared antireflection coatings fabricated by three-dimensional direct laser writing," *Opt. Lett.* **43**, 239 (2018).

[9] A. Boltasseva and V. M. Shalaev, "Fabrication of optical negative-index metamaterials: Recent advances and outlook," *Metamaterials* **2**, 1 (2008).

[10] M. Thiel, J. Ott, A. Radke, J. Kaschke, and M. Wegener, "Dip-in depletion optical lithography of three-dimensional chiral polarizers," *Opt. Lett.* **38**, 4252 (2013).

[11] Y. Li, D. B. Fullager, S. Park, D. Childers, R. Fesperman, G. Boreman, and T. Hofmann, "High-contrast infrared polymer photonic crystals fabricated by direct laser writing," *Opt. Lett.* **43**, 4711 (2018).

[12] W. J. Otter and S. Lucyszyn, "Hybrid 3-d-printing technology for tunable thz applications," *Proc. IEEE* **105**, 756 (2017).

[13] B. Zhang, Y. Guo, H. Zirath, and Y. P. Zhang, "Investigation on 3-d-printing technologies for millimeter- wave and terahertz applications," *Proc. IEEE* **105**, 723 (2017).

[14] S. Park, Z. Z. Clark, Y. Li, M. McLamb, and T. Hofmann, "A stereolithographically fabricated polymethacrylate broadband thz absorber," *2019 IEEE 16th International Conference on Smart Cities: Improving Quality of Life Using ICT & IoT and AI (HONET-ICT)*, 217 (2019).

[15] J. Li, C. M. Shah, W. Withayachumnankul, B. S.-Y. Ung, A. Mitchell, S. Sriram, M. Bhaskaran, S. Chang, and D. Abbott, "Mechanically tunable terahertz metamaterials," *Appl. Phys. Lett.* **102**, 121101 (2013).

[16] X. Zhao, J. Schalch, J. Zhang, H. R. Seren, G. Duan, R. D. Averitt, and X. Zhang,

"Electromechanically tunable metasurface transmission waveplate at terahertz frequencies," *Optica* **5**, 303 (2018).

[17] T. Hofmann, C. Herzinger, A. Boosalis, T. Tiwald, J. A. Woollam, and M. Schubert, "Variable-wavelength frequency-domain terahertz ellipsometry," *Rev. Sci. Instrum.* **81**, 023101 (2010).

[18] T. Hofmann, A. Boosalis, P. Kühne, C. Herzinger, J. Woollam, D. Gaskill, J. Tedesco, and M. Schubert, "Hole-channel conductivity in epitaxial graphene determined by terahertz optical-hall effect and midinfrared ellipsometry," *Appl. Phys. Lett.* **98**, 041906 (2011).

[19] P. Kühne, C. Herzinger, M. Schubert, J. Woollam, and T. Hofmann, "Invited article: An integrated mid-infrared, far-infrared, and terahertz optical hall effect instrument," *Rev. Sci. Instrum.* **85**, 071301 (2014).

[20] T. Hofmann, S. Knight, D. Sekora, D. Schmidt, C. Herzinger, J. Woollam, E. Schubert, and M. Schubert, "Screening effects in metal sculptured thin films studied with terahertz mueller matrix ellipsometry," *Appl. Surf. Sci.* **421**, 513 (2017).

[21] Formlabs, Installation and Usage Instructions Form 2 Desktop Stereolithrgraphy 3D Printer (2018).

[22] S. Park, Y. Li, D. B. Fullager, S. Schöche, C. M. Herzinger, G. D. Boreman, and T. Hofmann, "Terahertz to mid-infrared dielectric properties of polymethacrylates for stereolithographic single layer assembly," *J. Infrared Millim. Terahertz Waves* **40**, 971 (2019).

[23] D. B. Fullager, S. Park, C. Hovis, Y. Li, J. Reese, E. Sharma, S. Lee, C. Evans, G. D. Boreman, and T. Hofmann, "Metalized poly-methacrylate off-

axis parabolic mirrors for terahertz imaging fabricated by additive manufacturing," *J. Infrared Millim. Terahertz Waves* **40**, 269 (2019).

[24] H. Fujiwara, Spectroscopic Ellipsometry: Principles and Applications, (John Wiley & Sons, 2007).

[25] P. Hauge, "Recent developments in instrumentation in ellipsometry," *Surf. Sci.* **96**, 108 (1980).

[26] D. W. Berreman, "Optics in stratified and anisotropic media: 4× 4-matrix formulation," *J. Opt. Soc. Am.* **62**, 502 (1972).

[27] M. Schubert, "Polarization-dependent optical parameters of arbitrarily anisotropic homogeneous layered systems," *Phys. Rev. B* **53**, 4265 (1996).

[28] S. Park, Y. Li, D. B. Fullager, M. Lata, P. Kühne, V. Darakchieva, and T. Hofmann, "Terahertz optical properties of polymethacrylates after thermal annealing," *J. Vac. Sci. Technol. B* **37**, 062924 (2019).

[29] I. J. Hodgkinson and Q. Wu, Birefringent thin films and polarizing elements, (World Scientific, 1998).

[30] D. Schmidt, B. Booso, T. Hofmann, E. Schubert, A. Sarangan, and M. Schubert, "Generalized ellipsometry for monoclinic absorbing materials: determination of optical constants of cr columnar thin films," *Opt. Lett.* **34**, 992 (2009).

[31] G. E. Jellison, "Spectroscopic ellipsometry data analysis: measured versus calculatedquantities," *Thin Solid Films* **313-314**, 33 (1998).

[32] M. Naftaly and R. E. Miles, "Terahertz time-domain spectroscopy for material characterization," *Proc. IEEE* **95**, 1658 (2007).

[33] K. Oka and T. Kaneko, "Compact complete imaging polarimeter using birefringent wedge prisms," *Opt. Express* **11**, 1510 (2003).

[34] J. F. de Boer, C. K. Hitzenberger, and Y. Yasuno, "Polarization sensitive optical coherence tomography–a review," *Biomed. Opt. Express* **8**, 1838 (2017).

[35] Z. Jacob, L. V. Alekseyev, and E. Narimanov, "Optical hyperlens: far-field imaging beyond the diffraction limit," *Opt. Express* **14**, 8247 (2006).

[36] B.-I. Popa and S. A. Cummer, "Cloaking with optimized homogeneous anisotropic layers," *Phys. Rev. A* **79**, 023806 (2009).

[37] G. Ghosh, "Dispersion-equation coefficients for the refractive index and birefringence of calcite and quartz crystals," *Opt. Commun.* **163**, 95 (1999).

[38] W. Zhu, A. Liu, T. Bourouina, D. P. Tsai, J. Teng, X. Zhang, G. Lo, D. Kwong, and N. Zheludev, "Microelectromechanical maltese-cross metamaterial with tunable terahertz anisotropy," *Nat. Commun.* **3** (2012).

[39] S. Liu, T. J. Cui, Q. Xu, D. Bao, L. Du, X. Wan, W. X. Tang, C. Ouyang, X. Y. Zhou, H. Yuan, *et al.*, "Anisotropic coding metamaterials and their powerful manipulation of differently polarized terahertz waves," *Light Sci. Appl.* **5**, e16076 (2016).

[40] V. M. Shalaev, W. Cai, U. K. Chettiar, H.-K. Yuan, A. K. Sarychev, V. P. Drachev, and A. V. Kildishev, "Negative index of refraction in optical metamaterials," *Opt. Lett.* **30**, 3356 (2005).

[41] A. Salandrino and N. Engheta, "Far-field subdiffraction optical microscopy using metamaterial crystals: Theory and simulations," *Phys. Rev. B* **74**, 075103 (2006).

[42] L. H. Nicholls, F. J. Rodríguez-Fortuño, M. E. Nasir, R. M. Córdova-Castro, N. Olivier, G. A. Wurtz, and A. V. Zayats, "Ultrafast synthesis and switching

of light polarization in nonlinear anisotropic metamaterials," *Nat. Photonics* **11**, 628 (2017).

[43] Z. Wang, F. Cheng, T. Winsor, and Y. Liu, "Optical chiral metamaterials: a review of the fundamentals, fabrication methods and applications," *Nanotechnology* **27**, 412001 (2016).

[44] M. Askari, D. A. Hutchins, P. J. Thomas, L. Astolfi, R. L. Watson, M. Abdi, M. Ricci, S. Laureti, L. Nie, S. Freear, *et al.*, "Additive manufacturing of metamaterials: A review," *Addit. Manuf.* **36**, 101562 (2020).

[45] C. M. Soukoulis and M. Wegener, "Past achievements and future challenges in the development of three-dimensional photonic metamaterials," *Nat. Photonics* **5**, 523 (2011).

[46] Q. Wang, B. Gao, M. Raglione, H. Wang, B. Li, F. Toor, M. A. Arnold, and H. Ding, "Design, fabrication, and modulation of thz bandpass metamaterials," *Laser & Photonics Rev.* **13**, 1900071 (2019).

[47] S. Park, Y. Li, B. Norton, M. McLamb, G. D. Boreman, and T. Hofmann, "One-dimensional photonic crystals fabricated using stereolithographic single layer assembly for the terahertz spectral range," *J. Infrared Millim. Terahertz Waves* **41**, 542 (2020).

[48] S. Park, B. Norton, G. D. Boreman, and T. Hofmann, "Mechanical tuning of the terahertz photonic bandgap of 3d-printed one-dimensional photonic crystals," *J. Infrared Millim. Terahertz Waves* **42**, 1 (2020).

[49] S. Park, Y. Li, M. McLamb, B. Norton, G. D. Boreman, and T. Hofmann, "Highly localized defect mode in polymer-based thz photonic crystals fabricated using stereolithography," *J. Infrared Millim. Terahertz Waves* **41**, 825 (2020).

[50] E. Yablonovitch, “Inhibited spontaneous emission in solid-state physics and electronics,” *Phys. Rev. Lett.* **58**, 2059 (1987).

[51] J. D. Joannopoulos, P. R. Villeneuve, and S. Fan, “Photonic crystals,” *Solid State Commun.* **102**, 165 (1997).

[52] Z.-Y. Li, J. Wang, and B.-Y. Gu, “Creation of partial band gaps in anisotropic photonic-band-gap structures,” *Phys. Rev. B* **58**, 3721 (1998).

[53] G. Alagappan, X. Sun, P. Shum, M. Yu, and M. Doan, “One-dimensional anisotropic photonic crystal with a tunable bandgap,” *J. Opt. Soc. Am. B* **23**, 159 (2006).

[54] I. Abdulhalim, “Reflective phase-only modulation using one-dimensional photonic crystals,” *J. Opt. A - Pure Appl. Op.* **2**, L9 (2000).

[55] M. Honda, T. Seki, and Y. Takeoka, “Dual tuning of the photonic band-gap structure in soft photonic crystals,” *Adv. Mater.* **21**, 1801 (2009).

[56] I. V. Timofeev, D. N. Maksimov, and A. F. Sadreev, “Optical defect mode with tunable q factor in a one-dimensional anisotropic photonic crystal,” *Phys. Rev. B* **97**, 024306 (2018).

[57] Z. Wu, Z. Shi, H. Xia, X. Zhou, Q. Deng, J. Huang, X. Jiang, and W. Wu, “Design of highly birefringent and low-loss oligoporous-core thz photonic crystal fiber with single circular air-hole unit,” *IEEE Photonics J.* **8**, 1 (2016).

[58] L. Qi and C. Liu, “Complex band structures of 1d anisotropic graphene photonic crystal,” *Photonics Res.* **5**, 543 (2017).

[59] A. Ortigosa-Blanch, J. C. Knight, W. J. Wadsworth, J. Arriaga, B. J. Mangan, T. A. Birks, and P. S. J. Russell, “Highly birefringent photonic crystal fibers,” *Opt. Lett.* **25**, 1325 (2000).

[60] S. Park, Y. Li, D. Fullager, S. Schöche, C. Herzinger, S. Lee, and T. Hofmann, "Terahertz-frequency dielectric anisotropy in three-dimensional methacrylates fabricated by stereolithography," *Opt. Lett.* **45**, 1982 (2020).

[61] D. Schmidt and M. Schubert, "Anisotropic bruggeman effective medium approaches for slanted columnar thin films," *J. Appl. Phys.* **114**, 083510 (2013).

CHAPTER 6: STEREOLITHOGRAPHICALLY FABRICATED OFF-AXIS PARABOLIC REFLECTORS FOR THZ IMAGING

6.1 Metalized Poly-methacrylate Off-Axis Parabolic Mirrors for Terahertz Imaging Fabricated by Additive Manufacturing

Terahertz radiation sources are currently one of the most widely used non-ionizing illumination mechanisms for security applications and also find increasing utilization in quality control of commercial products.[1] Presently, a majority of these applications rely on scanning rather than direct imaging, and implicitly suffer from temporal latency due to post processing. The monetary and temporal cost associated with procuring commercially manufactured optics which are suitable for imaging leads to fundamental limitations in the ability to rapidly develop application specific imaging modalities using terahertz sources. Herein, we show a novel method for the rapid prototyping of metallic coated poly-methacrylate parabolic reflectors fabricated by stereolithographic 3D printing. Images comparing the performance a commercially available off-axis parabolic reflector to our metalized poly-methacrylate prototype which was designed to be identical to the commercially available mirror are subsequently presented. The images show that at 530 GHz it is possible to produce a metalized poly-methacrylate off-axis paraboloid whose spatial beam profile is nearly identical to that of a commercially available equivalent.

---

[1] Reprinted by permission from Springer Nature Customer Service Centre GmbH: Springer D. B. Fullager, S. Park, C. Hovis, Y. Li, J. Reese, E. Sharma, S. Lee, C. Evans, G. D. Boreman, and T. Hofmann, "Metalized Poly-methacrylate Off-Axis Parabolic Mirrors for Terahertz Imaging Fabricated by Additive Manufacturing," *J. Infrared, Millimeter, Terahertz Waves* **40**, 269 - 275 (2019). © 2019

6.1.1 Introduction

In order to develop novel THz imaging modalities usable from 290 GHz to 4.5 THz, it is often necessary to create a spatially uniform intensity distribution that is well-collimated to avoid diffracted orders in the image plane that detract from image quality [1, 2]. Often, the expansion of a collimated source is achieved by using a reversed telescope. However the cost of transmissive THz optics, which offer the necessary magnification factor, is prohibitive relative to reflective optics. This has led to a significant number of contributions to the literature contributions focused on additive manufacturing of transmissive optics from materials with relatively low loss [3, 4, 5, 6, 7, 8, 9]. In order to maximize the throughput of a THz and far-infrared optical system, however, reflective optics are more advantageous. An alternative method to the use of a reversed telescope, which expands the output of a point source in conjunction with a collimating lens, is to bring an off-axis parabolic reflector's focal point to the output aperture of the illumination source. This ideally produces a collimated output, which can then be expanded by successive off-axis parabolic reflectors of varying focal lengths [10]. The fundamental limitation of this strategy is that the degree of angular magnification is limited by the available focal lengths of off-the-shelf components or by the time and cost of obtaining custom optics.

There have previously been demonstrations of reflective focusing optics produced by additive manufacturing in the literature [11, 12, 13, 14], yet the development of a reflective collimating optic produced by additive manufacturing is lacking. Specifically, there are no demonstrations of metalized, stereolithographically 3D printed reflective collimating optics. Such printed optics potentially could be of significantly lighter weight than the conventional solid metal optics, in addition to having much lower thermal expansion properties, which will maintain optical alignment over a greater operating temperature range. All of these properties are of great importance, especially in space-based applications. In this particular case, our goal is to demonstrate that components for THz imaging using reflective optics can be fabricated by additive manufacturing and subsequent metalization by magnetron sputtering or other physical vapor deposition methods.

6.1.2 Rapid Prototyping of Terahertz Optical Components

To demonstrate the capabilities of reflective optical components produced by additive manufacturing techniques, the profile of a commercially available off-axis parabolic reflector (76.2 mm diameter, 228.6 mm reflected focal length, and 114.3 mm parent focal length) was fabricated by stereolithographic single layer assembly using a castable resin and desktop 3D printer (Castable Resin and Form 2 Desktop 3D Printer, Formlabs Inc.). A castable resin was chosen for this application as any material designed for casting and subsequent removal by heating implicitly possesses a lower vapor pressure than a standard methacrylate polymer [15]. Poly-methacrylates with higher vapor pressures are undesirable for metalization in vacuum systems as they prevent the deposition system from achieving a pressure which minimizes the presence of oxygen and other contaminants prior to sputtering due to out-gassing.

The stereolithography file used for fabrication was designed using Solidworks 2017 (Dassault Systems Inc.). The form factor of the commercially available parabolic mirror was determined using the well-known geometric properties of parabolas. Using a coordinate system where the focus of the parabola is located at a position in cartesian coordinates of (0,f), where f is the parent focal length of the off-axis paraboloid, the equation of the parabola is then given by

$$y = \frac{1}{4f}x^2. \tag{6.1}$$

The necessary coordinate range along the x-axis to provide the appropriate height is determined by the specified diameter and thickness of the optic. These parameters are then used to determine the appropriate curve, which is rotated about the z-axis to form a parabolic sheet. Subsequently, a circular base of the appropriate diameter is extruded to the surface of the parabolic sheet, leaving the desired form factor of the off-axis paraboloid.

The STL file is then loaded into the aforementioned desktop 3D printer and set to write at the finest resolution of the layer thickness which is 25 µm. The intent of utilizing the finest resolution of the single-layer assembly process is to achieve as close to a true-to-form shape as possible relative to the commercially available optic. The 76.2 mm diameter off-axis paraboloid takes approximately 13 hours to print. After fabrication the optic is rinsed in isopropyl alcohol for approximately 1 hour and then dried with compressed air. Subsequently, the support material required for fabrication by single-layer assembly is trimmed away leaving a self-supporting poly-methacrylate paraboloid. The castable resin requires a post bake and was cured for 4 hours at 72 °C. The poly-methacrylate paraboloid was then loaded into a sputtering system (ATC 1800-F, AJA Inc.) equipped with a DC magnetron loaded with a gold target as well as an RF magnetron loaded with a nickel-chrome (NiCr) target.

After being loaded into the chamber and pumped down to approximately 866 µPa

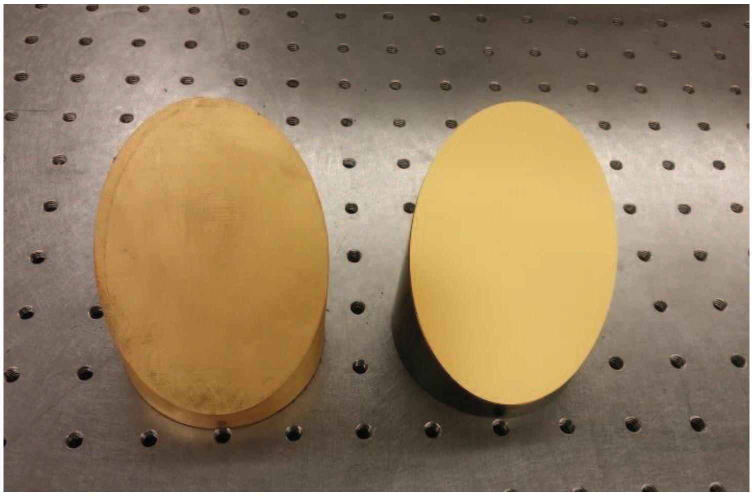

Figure 6.1: Photograph of a metalized 3D printed poly-methacrylate parabolic reflector (left) next to its commercially available equivalent (right).

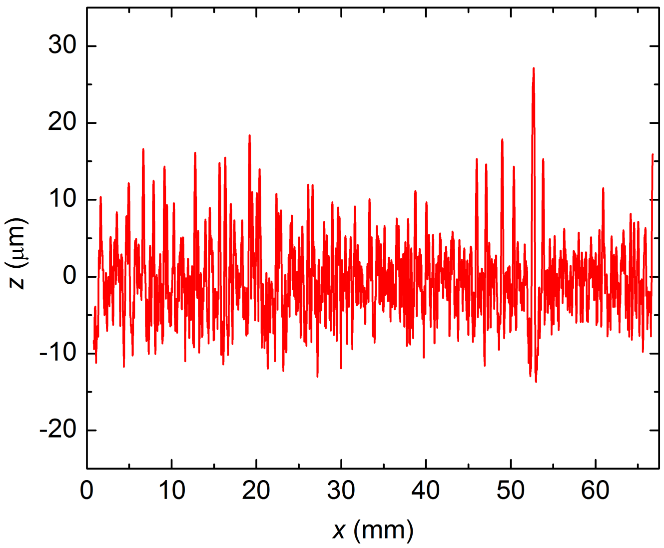

Figure 6.2: Surface profile of the poly-methacrylate OAP prototype obtained after sputtering using a tactile profilometer (LD 260, Mahr Inc.). The arithmetic mean deviation R_a and root mean squared deviation R_q is found to be 4 µm and 5 µm, respectively.

($6.5 \cdot 10^{-6}$ Torr), the paraboloid was then coated on a rotating table for 30 minutes at 150 W with NiCr and subsequently for 30 minutes at 50 W with gold at ambient temperature. The result of this process is shown in Fig. 6.1 which shows a visual side-by-side comparison of the metalized poly-methacrylate reflector Fig. 6.1, left next to its commercially available equivalent Fig. 6.1, right.

After metalization, the surface quality of the part was investigated by a tactile profilometer (LD 260, Mahr Inc.) equipped coordinate measurement machine as shown in Fig. 6.2. The arithmetic mean deviation R_a is 4 µm, and the root mean squared deviation R_q is 5 µm. As such, the surface is of a sufficient quality for imaging at a 566 µm wavelength, though coarser than the commercially available equivalent.

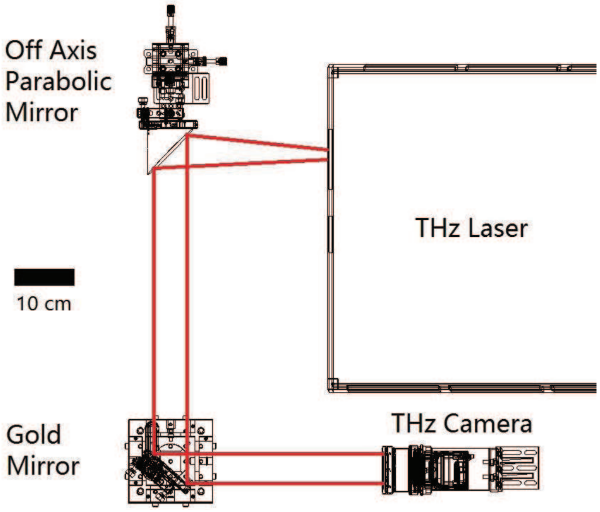

Figure 6.3: Schematic of the collimating and imaging setup used for the images depicted herein. The scale bar represents 10 cm.

6.1.3 Image Acquisition

To demonstrate the functionality of the metalized poly-methacrylate parabolic reflector, either of the two off-axis parabolic mirrors compared herein are mounted on a 3-way adjustable translation stage (x,y,z) on which a 76.2 mm kinematic mount with tip and tilt adjustment is affixed. The collimated output from the off-axis paraboloid is then reflected off of a 76.2 mm planar gold mirror which is used to increase the throw of the optical system so as to satisfy the minimum object distance of 70 cm of the THz camera's objective lens. For this experiment, a real time (50 Hz frame rate) THz camera (MICROXCAM-340I, Institut National d'Optique) equipped with a variable focus objective lens (f/# = 0.7) is used. The dimension of detector array is 384 × 288 pixels with 35 µm pixel pitch.

Fig. 6.3 shows a schematic of the optical system used to acquire the images shown in Fig. 6.4. The spatial beam profile of both parabolic reflectors is shown in Fig. 6.4. Both off-axis parabolic reflectors are placed with their focal points at the output aperture of a line tunable far-infrared laser source (SI-FIR, Coherent Inc.) emitting 530 GHz, which was chosen for this initial demonstration because it is close to the middle

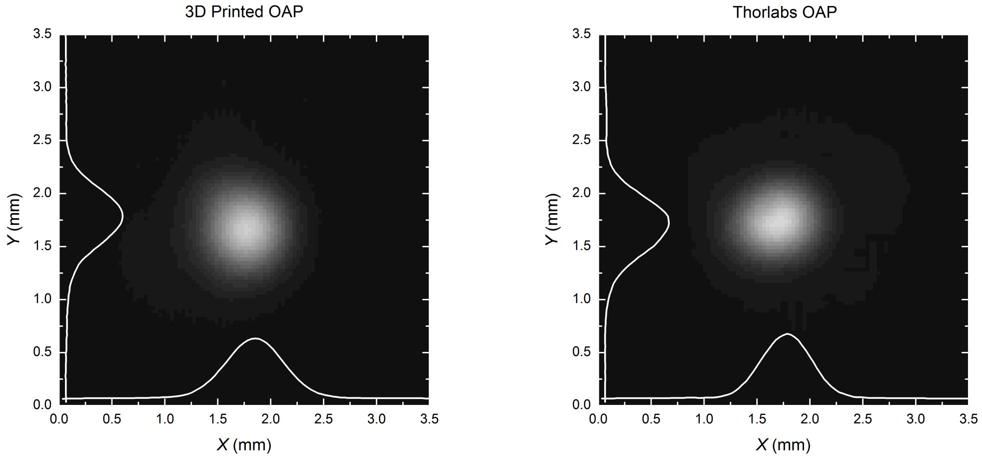

Figure 6.4: Greyscale spatial beam profiles of the metalized poly-methacrylate off-axis paraboloid (left), and the commercially available equivalent (right). Cross sectional intensity plots taken from the x and y axes are superimposed.

of the spectral range over which THz optics are typically used. After alignment, a Gaussian spot appears clearly for both the commercially available parabolic reflector as well as the metalized poly-methacrylate prototype. Both images were taken with nominally identical laser output power levels of approximately 140 µW ± 7 µW. The intensity data are measured by an Ophir thermopile detector with Juno ADC (Ophir-Spiricon Inc.) optimized for detection in the THz range. Intensity measurements were taken before and after each image was captured. No changes are made to the camera settings between image acquisitions to ensure consistency. Note, that the camera settings are optimized to capture the Gaussian beam profile, therefore higher order diffraction lobes are not visible in Fig. 6.4 due to the limitation in the dynamic range of the detector (30 nW at 2.52 THz), although they are detectable.

6.1.4 Discussion and Conclusions

The metalized poly-methacrylate off-axis paraboloid reflector investigated here shows very similar performance to a commercially available off-axis paraboloid with an identical focal length and diameter in the THz spectral range. We find that the spatial beam profile of the off-axis paraboloid fabricated using stereolithography is almost identical to the spatial beam profile of the commercially available off-axis paraboloid. For the purpose of collimating a coherent far-infrared source, the methods described herein offer a low-cost alternative to commercially available optics. We propose the metalization of reflective optics fabricated by stereolithographic 3D printing techniques as a novel alternative for rapid prototyping of custom optical components.

6.2 One-dimensional photonic crystal-based Terahertz Off-axis Parabolic Reflector fabricated with single step stereolithography

A polymer-based, off-axis parabolic reflector fabricated through stereolithographic 3D printing is demonstrated in the THz spectral range. The reflector was realized by alternating layers of compact and low-density layers, forming one-dimensional photonic crystal with reflective photonic bandgap therefore not requiring any extra step such as metalization in order to operate as reflector in the desired frequency range. Images comparing the performance of a commercially available off-axis parabolic reflector to the fabricated reflector with the same dimensions, are presented at frequency of 115.3 GHz. The images demonstrate the feasibility to stereolithographically fabricate off-axis parabolic reflector whose spatial beam profile and reflectivity are comparable to that of a commercially available equivalent, without any extra fabrication step.

6.2.1 Introduction

Advancement in terahertz (THz) optical systems requires optical components that can manipulate the THz wave propagation. Recently, additive manufacturing techniques have been recognized as rapid and cost-efficient solutions for rapid prototyping of THz optical elements such as gratings [5], waveguides [16, 17], broad-band absorbers [18, 19], and anisotropic metamaterials [20]. Among the additive manufacturing techniques used for the fabrication of THz optical components, stereolithography has emerged as a techcnique with a superior spatial resolution on the order of 10 µm and a substantially smaller surface roughness compared to other techniques [21, 22].

Reflective THz optical components have been demonstrated by the metalization of stereolithographically fabricated, polymer-based reflectors [23, 24]. These reflective components exhibit a surface roughness of approximately 5 µm and can achieve THz optical responses comparable to commercially available optics [24]. However demonstrations up to date rely on the metalization of polymer base geometry in order to obtain reflective properties for the final components. While the additive manufacturing approaches allow fabrication of arbitrary geometry, the extra metalization step adds cost and complexity to rapid prototyping of custom THz reflective optics.

THz frequency bands with very high reflectivity can also be realized by periodic structures consisting of dielectric materials [25]. Such spatially periodic arrangements of sub-wavelength scale constituents, commonly known as photonic crystals, influence the propagation of electromagnetic waves and form photonic bandgaps [26]. Band-stop and band-pass filters that allow broad-band reflection or selective transmission at desired frequencies are some of the essential components for developing an optical system. Recently, we have demonstrated polymer-based THz 1D photonic crystals fabricated by stereolithography with high reflection features in the W-band [27].

Stereolithography enables fabrication of virtually any complex geometry with sub-wavelength sized constituents for THz spectral range. Such successful demonstration of 1D photonic crystals in THz frequency range therefore suggests that powered reflectors can be realized based on these 1D photonic crystal designs. In this paper, we report for the first time on design and fabrication of all-dielectric, off-axis parabolic reflector designed based on the 1D photonic crystals for the THz spectral range.

6.2.2 Experiment

6.2.2.1 Design and fabrication

A commercially available gold off-axis parabolic reflector (76.2 mm diameter, 228.6 mm reflected focal length, and 114.3 mm parent focal length) was used as a reference for this demonstration. A reflector with the same outer profile, diameter and focal lengths as the commercially available reference was designed for stereolithographic fabrication. The design employed a number of identical pairs of alternating layers of compact and void layers, forming a 1D photonic crystal along the curved surface of the reflector as shown in the cross sectional view of the architecture in figure 6.5. The compact layers had parabolic interfaces parallel to each other, to maintain the parabolic surface profile throughout the 1D photonic crystal.

The compact layers are composed entirely of polymethacrylate without any intentional internal structure. The dielectric function of these compact layers is thus that of the polymethacrylate (black v4, Formlabs Inc.) employed here for fabrication and was accurately determined using infrared and THz spectroscopic ellipsometry [28]. The effective dielectric function of the void layers was assumed to be identical to that of air. In order to minimize possible deformation of the thin compact layers during the fabrication process, columnar support structures were dispersed throughout the void layer for added structural integrity. The volumetric fraction of the columnar inclusions were kept to be under 1 % in order to maintain the assumption that the layer is approximately void.

It was important to consider that the 1D photonic crystal formed along the parabolic surface of the reflector will experience a range of different incidence angle, which affects the spectral characteristics of the photonic bandgap. Thus in order to maintain high reflectivity even at higher angles of incidence, the thicknesses of the layers were optimized to create photonic bandgaps with the maximum spectral width. Stratified optical layer model calculation was carried out using a commercial software

(WVASE32$^{\text{TM}}$, J.A. Woollam Company) to perform optimization of layer thicknesses. The optical layer model comprises 13 layers of alternating compact and void layers all embedded in an air ambient. The design was optimized to place the photonic bandgap centered around 100 GHz at normal incidence. Optical layer model calculation predicted that the photonic bandgap will maintain reflectivity over 90 % at 110 GHz for incidence angle ranging 10° to 80°. As a result of these model calculations, the nominal geometry of the photonic crystal was finalized. The thickness of the compact layers and the void layers were selected to be 500 µm and 675 µm, respectively.

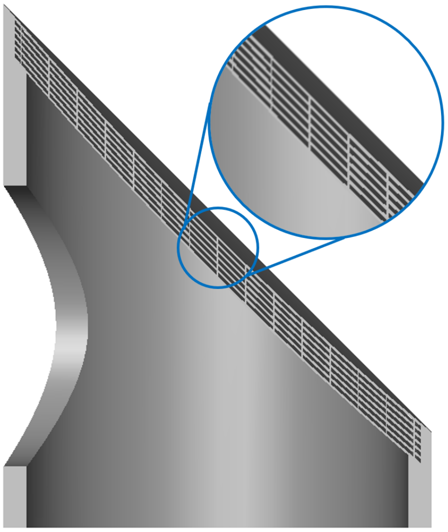

Figure 6.5: Cross-sectional side view of the CAD model of the off-axis parabolic reflector. Close-up view of the alternating compact and void layers are shown in the inset.

A 3D CAD (Computer Aided Design) model of the optimized reflector was acquired using a commercial software (SolidWorks, Dassault Systèmes). To minimize possible deformation of the thin compact layers during the fabrication process, columnar support structures were dispersed throughout the void layer for added structural integrity. The designed reflector was stereolithographically fabricated using a commercially available stereolithography system (Form2, Formlabs. Inc.) and resin (black v4, Formlabs. Inc.). The fabricated sample was cleaned with isopropyl alcohol to remove excess unpolymerized resin from the surface. The sample was subsequently dried using compressed air in order to remove any isopropyl alcohol from the surfaces.

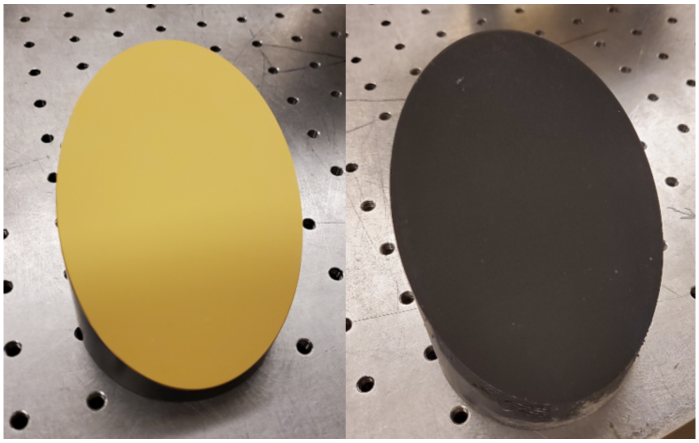

Figure 6.6: Commercially available (left) and the stereolithographically fabricated (right) off-axis parabolic reflector.

6.2.2.2 Data Acquisition and Analysis

In order to compare the performance of the stereolithographically fabricated reflector with its commercial counterpart, both reflectors were used to collimate output from a THz source. An electronic synthesizer (Synthesizer, Virginia Diodes Inc.) and an extension module (WR9.0SGX, Virginia Diodes Inc.) were used in tandem as the THz source for this experiment. Both off-axis parabolic reflectors are placed with their focal points at the output aperture of the source emitting 115.3 GHz. The collimated output from the off-axis parabolic reflectors was then imaged using a real time (50 Hz frame rate) THz camera (MICROXCAM-340I, Institut National d'Optique) equipped with a variable focus objective lens ($f/\# = 0.7$). The dimension of the detector array is 384 × 288 pixels with 35 µm pixel pitch. Note that the contrast setting was adjusted to more conveniently compare the Gaussian beam profiles emerging from the two reflectors. Collimated output power from the both reflectors were measured with a broadband power meter (PM5, Virginia Diodes Inc.) to verify the relative reflectivity of the stereolithographically fabricated reflector compared to the commercial reflector.

6.2.3 Results and discussion

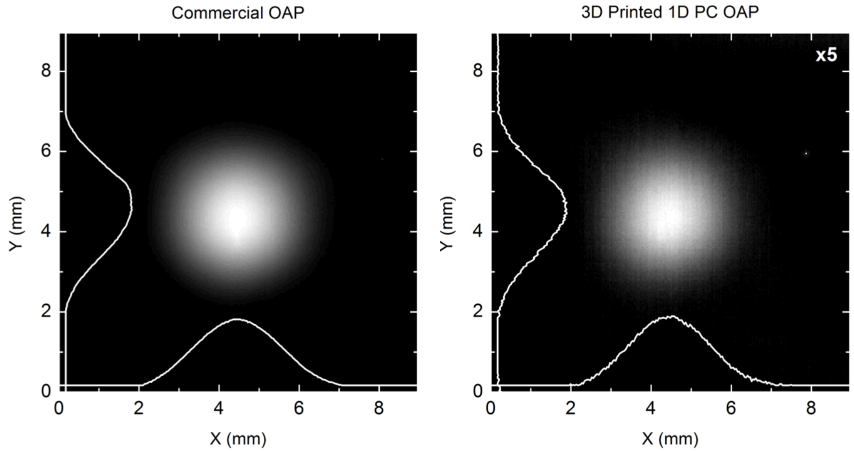

Figure 6.7: Collimated beam profiles obtained using a commercially available (left) and the stereolithographically fabricated (right) off-axis parabolic reflector.

Figure 6.7 illustrates the spatial beam profiles obtained using a commercial (left) and the stereolithographically fabricated (right) off-axis parabolic reflector. The two Gaussian beam profiles appear virtually identical.

The stereolithographically fabricated reflector had reflectivity approximately 23% of that of its commercial counterpart. This is significantly lower than the calculated nominal reflectivity at the chosen frequency (>90%). This is primarily attributed to the fact that the compact layers the reflector are composed of is thinner than the recommended minimum wall thickness of the stereolithography system that is employed here. Significant amount of deformation was observed in the thin layers, especially after the cleaning process with isopropyl alcohol. The thin layers underwent substantial amount of warping as isopropyl alcohol dried. In order to prevent such deformation, only the outer surface of the fabricated reflector was cleaned with isopropyl alcohol and the overall cleaning time was reduced to less than a minute. However the layers seemed to be affected noticeably even with the minimal cleaning involved. This geometric deformation appears to result in a substantial reduction in total reflectivity achieved by the fabricated part, while not affecting the resultant beam profile significantly.

The design of the off-axis parabolic reflector can be optimized further in order to improve the performance. The current design employs 7 layers of compact layers with identical curvature and does not compensate for varying angle of incidence along the surface. Geometrical parameters such as thickness and curvature can be calculated for each compact layer to highly reflect part of the incoming beam deviating from normal incidence.

6.2.4 Summary and conclusion

A polymer-based, off-axis parabolic reflector fabricated through stereolithographic 3D printing has been demonstrated in the THz spectral range. The reflector was realized by alternating layers of compact and low-density layers, forming one-dimensional photonic crystal with reflective photonic bandgap therefore not requiring any extra step such as metalization in order to operate as reflector in the desired frequency range. Images comparing the performance of a commercially available off-axis parabolic reflector to the fabricated reflector with the same dimensions, are presented at frequency of 115.3 GHz. The collimated beam profile achieved with the stereolithographically fabricated reflector is virtually identical to that obtained using a commercially available reflector. Intensity measurements were performed before and after collimation using a broadband power meter, revealing that the stereolithographically prototyped reflector has reflectivity of approximately 23% compared to its commercial counterpart. This discrepancy is attributed to the deformation caused by the limitation associated with fabrication process. Overall, stereolithography is suggested as a feasible method to fabricate off-axis parabolic reflectors whose spatial beam profile is comparable to that of a commercially available equivalent, without any extra fabrication step. Further optimization steps can be implemented in design and fabrication processes to improve the performance of the reflector.

REFERENCES

[1] B. Redding, M. A. Choma, and H. Cao, "Speckle-free laser imaging using random laser illumination," *Nat. Phot.* **6**, 355 (2012).

[2] J. C. Dainty, Laser speckle and related phenomena, (Springer Science & Business Media, 2013).

[3] S. F. Busch, M. Weidenbach, M. Fey, F. Schäfer, T. Probst, and M. Koch, "Optical properties of 3d printable plastics in the thz regime and their application for 3d printed thz optics," *J. Infrared Millim. Terahertz Waves* **35**, 993 (2014).

[4] S. F. Busch, M. Weidenbach, J. C. Balzer, and M. Koch, "Thz optics 3d printed with topas," *J. Infrared Millim. Terahertz Waves* **37**, 303 (2016).

[5] A. D. Squires, E. Constable, and R. A. Lewis, "3d printed terahertz diffraction gratings and lenses," *J. Infrared Millim. Terahertz Waves* **36**, 72 (2015).

[6] W. D. Furlan, V. Ferrando, J. A. Monsoriu, P. Zagrajek, E. Czerwińska, and M. Szustakowski, "3d printed diffractive terahertz lenses," *Opt. Lett.* **41**, 1748 (2016).

[7] H. Yi, S.-W. Qu, K.-B. Ng, C. H. Chan, and X. Bai, "3-d printed millimeter-wave and terahertz lenses with fixed and frequency scanned beam," *IEEE Trans. Antennas Propag.* **64**, 442 (2016).

[8] A. I. Hernandez-Serrano, M. Weidenbach, S. F. Busch, M. Koch, and E. Castro-Camus, "Fabrication of gradient-refractive-index lenses for terahertz applications by three-dimensional printing," *J. Opt. Soc. Am. B* **33**, 928 (2016).

[9] J. Liu, R. Mendis, and D. M. Mittleman, “A maxwell’s fish eye lens for the terahertz region,” *Appl. Phys. Lett.* **103**, 031104 (2013).

[10] A. Bergeron, M. Terroux, L. Marchese, O. Pancrati, M. Bolduc, and H. Jerominek, “Components, concepts, and technologies for useful video rate thz imaging,” *Millimetre Wave and Terahertz Sensors and Technology V* **8544**, 85440C (2012).

[11] D. Headland, W. Withayachumnankul, M. Webb, H. Ebendorff-Heidepriem, A. Luiten, and D. Abbott, “Analysis of 3d-printed metal for rapid-prototyped reflective terahertz optics,” *Opt. Express* **24**, 17384 (2016).

[12] P. Nayeri, M. Liang, R. Sabory-Garcia, M. Tuo, F. Yang, M. Gehm, H. Xin, and A. Elsherbeni, “High gain dielectric reflectarray antennas for thz applications,” *Antennas and Propagation Society International Symposium*, 1124 (2013).

[13] T. Niu, W. Withayachumnankul, B. S.-Y. Ung, H. Menekse, M. Bhaskaran, S. Sriram, and C. Fumeaux, “Experimental demonstration of reflectarray antennas at terahertz frequencies,” *Opt. Express* **21**, 2875 (2013).

[14] T. Niu, W. Withayachumnankul, A. Upadhyay, P. Gutruf, D. Abbott, M. Bhaskaran, S. Sriram, and C. Fumeaux, “Terahertz reflectarray as a polarizing beam splitter,” *Opt. Express* **22**, 16148 (2014).

[15] E. Johansson, O. Lidström, J. Johansson, O. Lyckfeldt, and E. Adolfsson, “Influence of resin composition on the defect formation in alumina manufactured by stereolithography,” *Materials* **10**, 138 (2017).

[16] M. Weidenbach, D. Jahn, A. Rehn, S. F. Busch, F. Beltrán-Mejía, J. C. Balzer, and M. Koch, “3d printed dielectric rectangular waveguides, splitters and couplers for 120 ghz,” *Opt. Express* **24**, 28968 (2016).

[17] J. Yang, J. Zhao, C. Gong, H. Tian, L. Sun, P. Chen, L. Lin, and W. Liu, "3d printed low-loss thz waveguide based on kagome photonic crystal structure," *Opt. Express* **24**, 22454 (2016).

[18] M. Petroff, J. Appel, K. Rostem, C. L. Bennett, J. Eimer, T. Marriage, J. Ramirez, and E. J. Wollack, "A 3d-printed broadband millimeter wave absorber," *Rev. Sci. Instrum.* **90**, 024701 (2019).

[19] S. Park, Z. Z. Clark, Y. Li, M. McLamb, and T. Hofmann, "A stereolithographically fabricated polymethacrylate broadband thz absorber," *2019 IEEE 16th International Conference on Smart Cities: Improving Quality of Life Using ICT & IoT and AI (HONET-ICT)*, 217 (2019).

[20] S. Park, Y. Li, D. Fullager, S. Schöche, C. Herzinger, S. Lee, and T. Hofmann, "Terahertz-frequency dielectric anisotropy in three-dimensional methacrylates fabricated by stereolithography," *Opt. Lett.* **45**, 1982 (2020).

[21] T. D. Ngo, A. Kashani, G. Imbalzano, K. T. Q. Nguyen, and D. Hui, "Additive manufacturing (3d printing): A review of materials, methods, applications and challenges," *Compos. B. Eng* **143**, 172 (2018).

[22] A. I. Shallan, P. Smejkal, M. Corban, R. M. Guijt, and M. C. Breadmore, "Cost-effective three-dimensional printing of visibly transparent microchips within minutes," *Anal. Chem.* **18**, 3124 (2014).

[23] J. A. Colla, R. E. M. Vickers, M. Nancarrow, and R. A. Lewis, "3d printing metallised plastics as terahertz reflectors," *J. Infrared Millim. Terahertz Waves* **40**, 752 (2019).

[24] D. B. Fullager, S. Park, C. Hovis, Y. Li, J. Reese, E. Sharma, S. Lee, C. Evans, G. D. Boreman, and T. Hofmann, "Metalized poly-methacrylate off-

axis parabolic mirrors for terahertz imaging fabricated by additive manufacturing," *J. Infrared Millim. Terahertz Waves* **40**, 269 (2019).

[25] N. Krumbholz, K. Gerlach, F. Rutz, M. Koch, R. Piesiewicz, T. Kürner, and D. Mittleman, "Omnidirectional terahertz mirrors: A key element for future terahertz communication systems," *Appl. Phys. Lett.* **88**, 202905 (2006).

[26] E. Yablonovitch, "Inhibited spontaneous emission in solid-state physics and electronics," *Phys. Rev. Lett.* **58**, 2059 (1987).

[27] S. Park, Y. Li, B. Norton, M. McLamb, G. D. Boreman, and T. Hofmann, "One-dimensional photonic crystals fabricated using stereolithographic single layer assembly for the terahertz spectral range," *J. Infrared Millim. Terahertz Waves* **41**, 542 (2020).

[28] S. Park, Y. Li, D. B. Fullager, S. Schöche, C. M. Herzinger, G. D. Boreman, and T. Hofmann, "Terahertz to mid-infrared dielectric properties of polymethacrylates for stereolithographic single layer assembly," *J. Infrared Millim. Terahertz Waves* **40**, 971 (2019).

CHAPTER 7: SUMMARY AND OUTLOOK

Stereolithography has been introduced as a promising fabrication approach for custom THz optical components and novel metamaterials with designed electromagnetic properties. The infrared and THz complex dielectric function of several different types of polymethacrylates commercially available for stereolithography systems have been accurately determined using spectroscopic ellipsometry. The dielectric functions were then used to predict optical response of various optical components in the THz spectral range during the design process. All-dielectric THz 1D photonic crystals composed of layers of low and high density fabricated from a single polymer and THz anisotropic metamaterials consisting of slanted columnar structures were fabricated in a single-step stereolithography and characterized in the THz frequency range. The 1D photonic crystal structures were explored further and defect modes and mechanical tuning of the THz photonic bandgaps in these crystals were demonstrated. The THz anisotropic metamaterial design has been implemented into such 1D photonic crystals for the first time and polarization direction dependent photonic bandgaps have been demonstrated. Furthermore, 1D photonic crystal design was successfully implemented to create powered THz reflective optics, which typically requires metalization of the surface after the polymer-based additive manufacturing process. In summary, following results have been obtained during the course of this work:

- **Complex dielectric functions of polymethacrylates**

  Optical properties of several different types of polymethacrylates commonly used for stereolithographic fabrication have been characterized. Spectroscopic ellipsometry data were obtained in the mid-infrared and THz spectral ranges and the data sets were analyzed using a stratified optical layer model approach.

While a number of strong absorption features with Gaussian broadening profile dominated the infrared spectral range, the polymethacrylates were found to exhibit only weak absorption in the THz range. The polymethacrylates were found to be suitable for fabrication of thin transmissive THz optics. These results have been published in Journal of Infrared, Millimeter and Terahertz waves.

- **THz one-dimensional photonic crystals**

  Polymer-based one-dimensional photonic crystals with photonic bandgaps in THz frequency range were designed and fabricated through stereolithography and were characterized using THz transmission spectroscopy in the spectral range from 82 to 125 GHz. Distinct photonic bandgaps centered within the investigated frequency range were observed in the experimental transmission spectra. The photonic crystals consist of alternating solid, compact layers of polymethacrylate and low-density layers composed of sub-wavelength scale columnar structures dispersed throughout the layer. The Bruggeman effective medium approximation was found to describe the dielectric function of such low-density layers accurately. THz defect modes, which are highly localized transmission within the THz photonic bandgaps of these 1D photonic crystals, have also been realized. Both the photonic bandgap and the defect mode were explored for their mechanical tunability, where a spectral shift of the resonances was achieved by manipulation of the photonic crystal geometry. These results have been published in Journal of Infrared, Millimeter and Terahertz waves.

- **THz anisotropic metamaterials**

  THz anisotropic metamaterials composed of slanted columnar layers were realized using polymethacrylate based stereolithography for the first time. The structures were characterized in THz spectral range using generalized spectroscopic ellipsometry and strong anisotropic responses were observed. Using a similar geometry, 1D photonic crystals were fabricated. A 2 GHz shift in the center frequency of the photonic bandgap as a function of in-plane orientation was revealed in the linearly polarized THz transmission spectra. These results have been published in Optics Letters.

- **Additively manufacturing approaches for powered THz reflective optics**

  Two different approaches for manufacturing powered reflective optics in the THz spectral range were investigated. An off-axis parabolic reflector was fabricated by metalizing a polymer base. The printed polymer structure with desired geometric parameters was coated with gold by sputter deposition. The comparison between the manufactured reflector and its commercial counterpart revealed that the performances are comparable. Another method of creating such powered optics by stereolithography was explored. For this design a 1D photonic crystal design was employed. By adding desired curvature to the layers that comprise the photonic crystal, all-dielectric THz off-axis parabolic reflectors can be manufactured in a single-step stereolithography. These results are in preparation for publication in Optics Letters.

The potential of stereolithography for effective rapid prototyping and manufacturing of custom THz optics and metamaterials have been studied, with several exemplary demonstrations. Our results demonstrate that stereolithography can serve as an effective way of fabricating THz optics with virtually arbitrary architecture as well as metamaterials with tailored optical properties including anisotropy. Stereolithography is envisioned as a versatile technique for creating THz optical components with designed optical properties, for various applications including surveillance, THz sensing, and polarimetric detection.

LIST OF OWN PUBLICATIONS

The following peer-reviewed technical articles have been published as part of this dissertation and are partially included in the following chapters.

1. Y. Li, D. Fullager, **S. Park**, D. Childers, R. Fesperman, G. Boreman, and T. Hofmann, "High-contrast infrared polymer photonic crystals fabricated by direct laser writing," *Opt. Lett.* **43**, 4711 (2018).
2. Y. Li, **S. Park**, M. McLamb, M. Lata, S. Schöche, D. Childers, I. Aggarwal, M. Poutous, G. Boreman, and T. Hofmann, "UV to NIR optical properties of IP-Dip, IP-L, and IP-S after two-photon polymerization determined by spectroscopic ellipsometry," *Opt. Mater. Express* **9**, 4318 (2019).
3. Y. Li, **S. Park**, D. B. Fullager, D. Childers, M. K. Poutous, I. D. Aggarwal, G. Boreman, and T. Hofmann, "Near-infrared transmittance enhancement using fully conformal antireflective structured surfaces on microlenses fabricated by direct laser writing," *Opt. Eng.* **58**, 010501 (2019).
4. Y. Li, M. Kocherga, **S. Park**, M. Lata, M. McLamb, G. Boreman, T. A. Schmedake, and T. Hofmann, "Optical dielectric function of Si(2,6-bis(benzimidazol-2´-yl)pyridine)$_2$ determined by spectroscopic ellipsometry," *Opt. Mater. Express* **9**, 3469 (2019).
5. Y. Li, **S. Park**, M. McLamb, M. Lata, D. Childers, and T. Hofmann, "Fabrication of optical components with nm-to mm-scale critical features using three-dimensional direct laser writing," *IEEE HONET-ICT*, 213 (2019).
6. **S. Park**, Y. Li, D. B. Fullager, S. Schöche, C. M. Herzinger, G. D. Boreman, and T. Hofmann, "Terahertz to mid-infrared dielectric properties of polymethacrylates for stereolithographic single layer assembly," *J. Infrared, Millimeter, Terahertz Waves* **40**, 971 (2019).

7. **S. Park**, Y. Li, D. B. Fullager, M. Lata, P. Kühne, V. Darakchieva, and T. Hofmann, "Terahertz optical properties of polymethacrylates after thermal annealing," *J. Vac. Sci Technol. B* **37**, 062924 (2019).

8. M. Lata, Y. Li, **S. Park**, M. J. McLamb, and T. Hofmann, "Direct laser writing of birefringent photonic crystals for the infrared spectral range," *J. Vac. Sci Technol. B* **37**, 062905 (2019).

9. M. McLamb, Y. Li, **S. Park**, M. Lata, and T. Hofmann, "Diffraction gratings for uniform light extraction from light guides," *IEEE HONET-ICT*, 220 (2019).

10. **S. Park**, Z. Z. Clark, Y. Li, M. McLamb, and T. Hofmann, "A stereolithographically fabricated polymethacrylate broadband THz absorber," *IEEE HONET-ICT*, 217 (2019).

11. D. B. Fullager, **S. Park**, C. Hovis, Y. Li, J. Reese, E. Sharma, S. Lee, C. Evans, G. D. Boreman, and T. Hofmann, "Metalized poly-methacrylate off-axis parabolic mirrors for terahertz imaging fabricated by additive manufacturing," *J. Infrared, Millimeter, Terahertz Waves* **40**, 269 (2019).

12. **S. Park**, Y. Li, B. Norton, M. McLamb, G. D. Boreman, and T. Hofmann, "One-dimensional Photonic Crystals Fabricated Using Stereolithographic Single Layer Assembly for the Terahertz Spectral Range," *J. Infrared, Millimeter, Terahertz Waves* **41**, 542 (2020).

13. **S. Park**, Y. Li, M. McLamb, B. Norton, G. D. Boreman, and T. Hofmann, "Highly Localized Defect Mode in Polymer-Based THz Photonic Crystals Fabricated Using Stereolithography," *J. Infrared, Millimeter, Terahertz Waves* **41**, 825 (2020).

14. **S. Park**, Y. Li, D. B. Fullager, S. Schöche, C. M. Herzinger, S. Lee, and

T. Hofmann, “Terahertz-frequency dielectric anisotropy in three-dimensional polymethacrylates fabricated by stereolithography,” *Opt. Lett.* **45**, 1982 (2020).

15. **S. Park**, B. Norton, G. D. Boreman, and T. Hofmann, “Mechanical Tuning of the Terahertz Photonic Bandgap of 3D-Printed One-Dimensional Photonic Crystals,” *J. Infrared, Millimeter, Terahertz Waves* **42**, 220 (2021).

16. **S. Park**, V. P. Stinson, G. D. Boreman, and T. Hofmann, “Terahertz anisotropic response of additively manufactured one-dimensional photonic crystals,” *Opt. Lett.* **46**, 3396 (2021).

17. Y. Li, M. McLamb, **S. Park**, D. Childers, G. D. Boreman, and T. Hofmann, “Theoretical Study of Enhanced Plasmonic - Photonic Hybrid Cavity Modes in Reciprocal Plasmonic Metasurfaces,” *Plasmonics* (2021).

18. **S. Park**, V. P. Stinson, M. McLamb, G. D. Boreman, and T. Hofmann, “Mechanical tuning of defect modes in polymer-based terahertz one-dimensional photonic crystals fabricated by stereolithography,” *accepted in Opt. Eng.* (2021).